Master's Thesis

Morphodynamic evolution of double-inlet systems: a numerical model study

T.V. de Ruijsscher

Supervisor:
Prof. Dr. H.E. de Swart
Daily supervisor:
W. Ridderinkhof, MSc

Second examiner:
Prof. dr. W.M.P. de Ruijter

Utrecht University

Institute for Marine and Atmospheric research Utrecht (IMAU),

Coastal and Shelf Sea Dynamics

April 2014 — January 2015

Abstract

A vast amount of tidal inlet systems worldwide are multiple inlet tidal systems. Numerical modelling studies have been, however, mainly focussed on single inlet tidal systems. Furthermore, some semi-analytical models suggest that multiple inlet tidal systems are not stable on geological timescales. In this thesis a numerical morphodynamic model is used to investigate whether double inlet tidal systems can subsist on longer timescales in an environment without waves, and what effect a different inlet spacing and artificial lowering of the bed have on sediment transport patterns and on the bed level profiles.

It is found that when developing from an initially flat bottom, a channel-shoal network develops that has a similar structure as that observed in the Wadden Sea. The main channels in terms of net sediment transport are tilted downdrift in the basin, making the system more asymmetrical. After 185 yr of morphological evolution, the total eroded sediment and sediment transports in the basin reach a quasi-steady value, indicating the development of a steady double inlet system. However, a continuous import of sediment occurs, which is due to tidal asymmetry, but in the updrift inlet mainly due to the residual flow. In the basin a tidal watershed develops — separating the basin parts drained by each inlet — which is shifted downdrift as a result of the phase difference between the inlets.

When the inlet spacing is increased, the main channels in terms of net sediment transport shift from a dominant direction away from the watershed to a dominant direction towards the watershed. The system imports sediment for all studied distances between the inlets, but for increasing inlet spacing, the import due to the residual flow increases, whereas the import due to tidal asymmetry decreases. Furthermore, the sediment transports of downdrift and updrift sub-system become more equal with increased inlet spacing, consequently the updrift sub-system becomes less dominant. Regarding the tidal watershed, its location shifts downdrift with increasing inlet spacing (due to the phase difference between the inlets), whereas it forms a less effective separation of the two sub-systems for a larger distance between the inlets.

Finally, when the bed level is lowered artificially, almost no morphological changes occur in the proximity of the peak lowering, mainly caused by a decreased velocity due to mass continuity. The tidal prism in the updrift sub-basin increases, resulting in increased erosion of the updrift inlet. Counterintuitively, a lowering of the bed level causes a decreased sediment import.

Contents

1. Introduction

Coasts have a variety of appearances all over the world. One of these are barrier coasts, which consist of barrier islands, sheltering a back-barrier basin from the sea [Beets & Van der Spek, 2000; Davis & Fitzgerald, 2004]. These barrier coasts ($\sim$ 15% of today's coastlines) resulted from the flooding of the continental shelves since the last glaciation ($\sim 12,000$ yr BP) during the Holocene. This flooding introduced a complex dynamics of filling the topographic lows with sediment and eroding the topographic highs, which eventually formed the present barrier coastal configurations.

Barrier coasts consist of tidal inlet systems, of which a schematic example is shown in fig. 1.1. These tidal inlet systems consist of an inlet, providing a connection between the back-barrier basin and the sea. At the seaward side of the inlet, an ebb-tidal delta is present: a region of accumulated sediment and thus a higher bed level. Additionally, a flood delta is present in the back-barrier basin. Such a flood delta in general consists of tidal flats or shoals, which are areas in the back-barrier basin that are submerged only during a part of the tidal cycle. Besides these shoals, a complex tidal network of channels exists in the back-barrier basin, described by e.g. Van Veen [1950] as showing tree-type shapes reminiscent of apple trees. The basin is enclosed by the main coast, barrier islands, one or more inlets and possibly by tidal watersheds. These tidal watersheds are lines that divide the drainage areas of the various inlets, see fig. 1.1 [De Swart & Zimmerman, 2009]. Tidal currents are present near the coast, which can be both parallel to the coast (e.g. in the Wadden Sea, see Oost & De Boer [1994]) and cross-shore (e.g. in North Carolina, eastern coast of the USA, see Van der Vegt et al. [2006]) in the near-shore sea and cross-shore in the inlet. Moreover, waves act on the coast, resulting in longshore sediment transport known as littoral drift [CERC, 1984]. It is important to note that back-barrier basins can be drained by multiple inlets, as a result of which a division has to be made between single inlet and multiple inlet tidal systems.

Examples of tidal inlet systems are the Ria Formosa in southern Portugal (studied by e.g. Salles et al. [2005]), the Wadden Sea along the Dutch, German and Danish coast (described extensively by Oost & De Boer [1994]), the Venice Lagoon (studied by e.g. Amos et al. [2004]) and barrier islands along the eastern coast of the USA, e.g. in North Carolina (studied by e.g. Van der Vegt et al. [2006]). Many of these systems are multiple inlet systems [Salles, 2001], where a throughflow of water from one inlet to another (via the back-barrier basin) can be present, which is investigated e.g. by Ridderinkhof [1988] and Buijsman & Ridderinkhof [2007].

Many multiple inlet systems are stable in the sense that their inlets stay open. In the past, also unstable configurations have been observed (i.e., one ore more inlets close during the morphological evolution of the system). An example is the closure of the tidal inlets at the

western coast of the Netherlands [Beets & Van der Spek, 2000]. Although an inlet stays open, it can still behave quite dynamic in its location, as for instance the trend of the (now artificially closed) Ancão inlet in the Ria Formosa system to shift eastward in time [Williams et al., 2003].

On a timescale of several years, the morphological patterns (e.g. channel-shoal patterns and ebb-tidal deltas) of tidal inlet systems not only affect sediment transport (both in magnitude and direction), but also the ecology of the system. Shoals are for instance important for birds. Furthermore, about 60% of the human population lives within 100 km from the coast [Vitousek et al., 1997]. For these reasons, it is of still increasing importance to know about the morphodynamic response of barrier coast systems to external changes, e.g. sea level rise, storms, ecological interactions and human interventions.

During the last decades, insight in the morphologic behaviour of tidal inlet systems has been gained. One of the first studies on tidal inlet systems was done by Escoffier [1940] (building on earlier work of Brown [1928]), who described the evolution of the cross-sectional area of a tidal inlet as competition between littoral drift (attempting to close the inlet) and the ebb-tidal current (attempting to erode the inlet). This approach was extended to multiple inlets draining a back-barrier basin, where Van de Kreeke [1990] pointed out that without the presence of a topographic high, which separates sub-basins drained by separate inlets, no stable morphodynamic equilibrium can be found. This was based on the equilibrium relation between inlet cross-sectional area and tidal prism (e.g. O'Brien [1966]). Van de Kreeke et al. [2008] concluded that a double inlet tidal system can be morphodynamically stable (i.e., both inlets remain open), provided that a topographic high separates the back-barrier basin in two sub-basins that hardly interact. De Swart & Volp [2012] extended the semi-analytical model of Van de Kreeke et al. [2008] by adding hypsometric effects (varying cross-sectional area of the inlet and wetted surface of the lagoon during the tidal cycle). They also found multiple stable morphodynamic equilibria and concluded that these equilibria are sensitive to changes in parameters that break the symmetry of the system, e.g., the ratio of the surface areas of the back-barrier basins and the phase difference of the tidal wave. Furthermore, Brouwer et al. [2012] showed (building on the analytical model of Van de Kreeke et al. [2008]), that when exit and entrance losses in the inlet are taken into account, a tidal watershed is not necessary for a double inlet system to be morphodynamically stable. Recently, Roos et al. [2013] explored the observed existence of stable barrier coasts with a morphodynamic model using an arbitrary number of inlets that connect back-barrier basin and ocean, explicitly including spatial variations in tide levels in the back-barrier basin and the ocean. They concluded that such systems have morphodynamic equilibrium states with multiple open inlets, where the number of open inlets depends on the tidal range and basin width.

Besides semi-analytical models, also numerical models have been used to study tidal inlet systems. As one of the early attempts in numerical models of tidal inlet systems, Wang et al. [1995] developed a process-based dynamic model for morphological development in the 'Friesche Zeegat' tidal inlet in the Dutch Wadden Sea. Van Leeuwen et al. [2003] presented and discussed results of long-term simulations of the 'Friesche Zeegat' case with an extended version of this model. They reproduced ebb-tidal deltas which compare fairly well with observations. Tidal network development in a short tidal basin was studied numerically by Marciano et al. [2005], showing triple branching behaviour of channels, similar to the three to four times branching behaviour observed in the Wadden Sea. It should however be noted that the developed tidal networks in numerical models are still extremely sensitive to parameterisations, as discussed by Dissanayake et al. [2009]. In order to improve existing numerical models and allow for long-

term simulations, several methods for morphological updating of the bed level are developed, of which most are based on multiplying bed level changes by a so-called 'morphological factor' [Roelvink, 2006; Van Maanen et al., 2011; Fortunato & Oliveira, 2004]. Such an improved model was among others used by Dissanayake et al. [2012] in order to assess the influence of a human intervention in an existing barrier coast system, in this case the Ley Bay area in the East Frisian Wadden Sea. Also they investigated the influence of single and multiple sediment fractions on e.g. erosion and sedimentation volumes in the inlets. Recently, Ridderinkhof et al. [2014a] used a morphodynamic model to explore influence of the length of back-barrier basins on the hydrodynamics. They also showed that no unique relationship exists between tidal prism and ebb-tidal delta volume, because the ebb-tidal delta volume is affected by the net sediment transport due to tidal asymmetry.

Most of the above mentioned numerical studies focus on single inlet tidal systems. Although multiple inlet systems have been investigated with semi-analytical models, no specific effort has been put in investigating these systems with process-based numerical models, except for a small amount of studies (e.g., investigation of the Ria Formosa by Salles et al. [2005]). This motivates the overall objective of the present study, i.e., revealing and understanding the morphodynamic pattern formation in double inlet tidal systems due to an external tidal forcing, and investigating the possibility of a stable configuration (i.e., two inlets remain open) without the effect of waves. This is an addition to e.g. Van de Kreeke et al. [2008] and Roos et al. [2013], who showed that a multiple inlet tidal system can reach a stable morphodynamic equilibrium if waves are taken into account and if a watershed is present (prescribed or dynamically implemented). To achieve this, rather than prescribing a watershed by a topographic high (cf. Van de Kreeke et al. [2008] and De Swart & Volp [2012]), initially a flat bathymetry is introduced, and a watershed is expected to develop dynamically. In order to get insight in the development of double inlet tidal systems, following research questions are formulated:

1. What are the main characteristics of the hydrodynamics and of morphologic patterns that form in a double inlet tidal system, why do they arise and how do they develop in time?
   (a) What are the morphologic characteristics of the channel-shoal patterns in the basin and of the ebb-tidal deltas in terms of location, shape and bottom elevation?
   (b) What are the hydrodynamic characteristics of the system in terms of tidal flow, residual flow, net sediment transport and tidal asymmetry?
   (c) Does the system evolve towards a morphodynamic equilibrium state, considering the weighted centre of channel volume, total eroded sediment volume and sediment exchange between basin, inlets and sea? And if so, do both inlets remain open?
   (d) Will a tidal watershed develop?
2. What is the effect of the distance between the two inlets on the morphological evolution of a double inlet tidal system, considering location of a tidal watershed, sediment exchange between sea, inlets and basin, and formation of ebb-tidal deltas?
   (a) What is the effect of the distance between the two inlets on the morphologic characteristics of the channel-shoal patterns in the basin and of the ebb-tidal deltas, considering location, shape and bed level elevation?
   (b) What is the effect of the distance between the two inlets on the net sediment transport patterns and tidal asymmetry?

(c) Does a different inlet spacing change sediment exchange between sea, inlets and basin?

(d) Does the distance between the inlets influence the location of a tidal watershed and the degree to which it effectively separates the two sub-basins?

For several years, gas has been extracted from below the Dutch Wadden Sea already [Beerlage & Ten Holder, 2009]. Recently the Dutch government also gave permission for salt mining in the Wadden Sea [MER, 2014]. Both processes could lead to subsidence of the Wadden Sea bottom [Buijsman, 1997; MER, 2014], which could have large effects on the ecological functioning of the part of the Wadden Sea where it takes place, or even on a larger scale, if the whole system adapts morphodynamically to the local bed level change. Therefore, it is important to know how a well-developed back-barrier system adapts after a given lowering of the bottom. To get a first indication of the morphodynamic adaptation of the tidal inlet system, an additional research question is introduced:

3. What effect does lowering of the bed level have on the morphologic channel-shoal patterns in the back-barrier basin and on the ebb-tidal delta location and extension, and does the tidal inlet system compensate the lowering by an import of sediment?

   (a) What effect do both location and intensity of the lowering have on changes in the observed channel-shoal patterns in the back-barrier basin, and in the appearance (location, extension, intensity) of the ebb-tidal deltas?

   (b) Do the inlets import sediment to compensate for a sudden lowering of the bed level?

The structure of the rest of this thesis is the following. In chapter 2, the used numerical morphodynamic model will be introduced, together with the model domain and parameter value choices. Furhermore, the theoretical tools used in this thesis to analyse the model results are introduced. In chapter 3, the results are described, in the order of the research questions as indicated above. Thereafter, the results as well as the numerical model assumptions are discussed in chapter 4. In chapter 5, brief contemplative conclusions on the present research are given. Finally, an outlook for further research is presented in chapter 6.

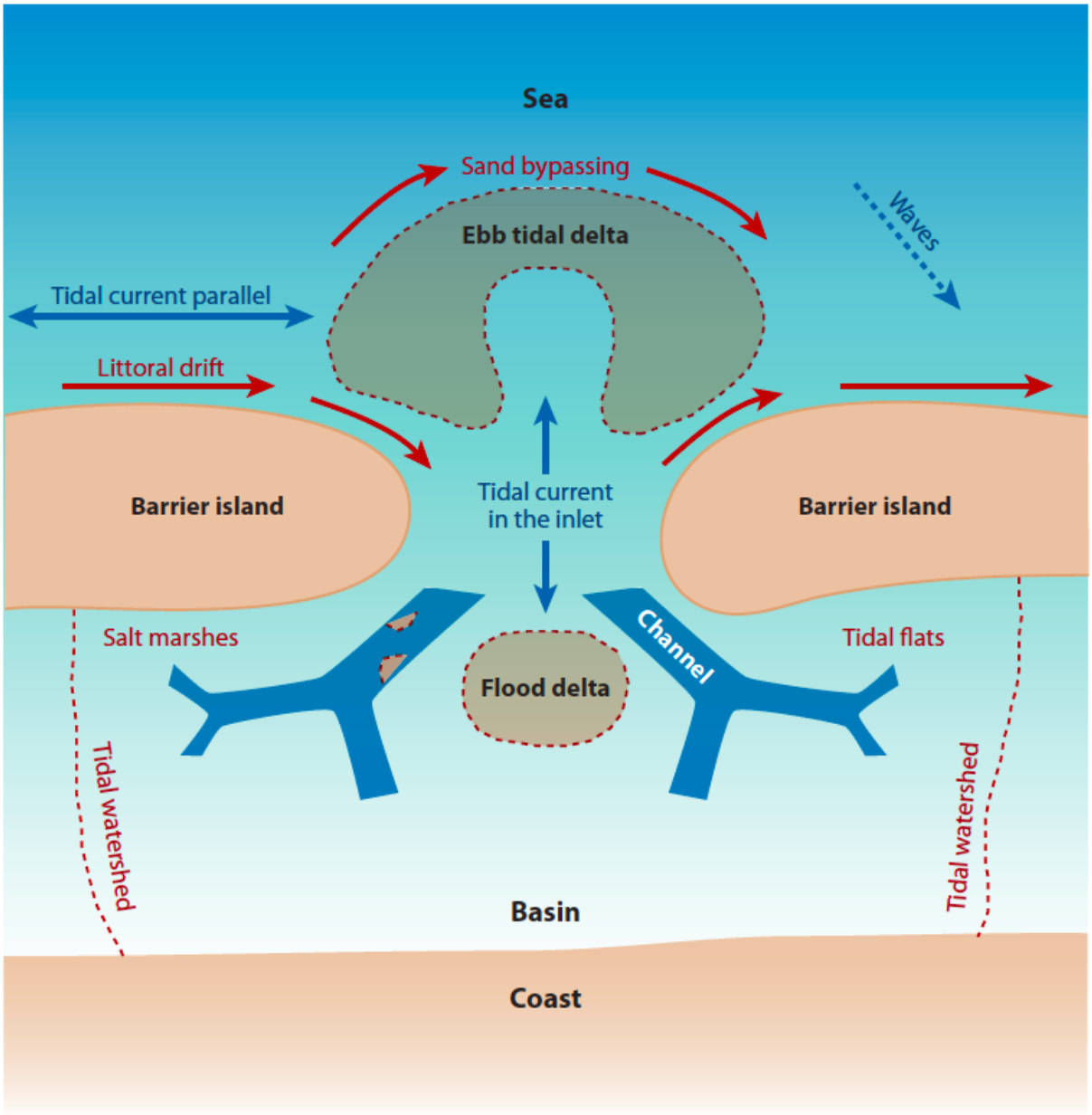

Figure 1.1: Sketch of an idealised tidal inlet system, showing the different geomorphologic elements and the dominant physical processes and phenomena [De Swart & Zimmerman, 2009].

2. Materials and methods

2.1 Materials

2.1.1 Domain specifications

For this research, a domain is composed consisting of a rectangular basin (length L and width B), connected to a sea by two inlets, each of initial width B_{inl} and length L_{inl} (see fig. 2.1). The dimensions of this basin are representative for the relatively small tidal inlet system of the German Wadden island of Baltrum in the East Frisian Wadden Sea. The coordinates in this model domain are described by a two-dimensional coordinate system, with the x-direction parallel to the coast and the y-coordinate perpendicular to the coast (see fig. 2.1). Only the domain visualised in fig. 2.1 will be dealt with, but to avoid effects of the domain boundaries on the results in the region of interest, the total sea consists of the larger intervals $0\,\text{km} \leq x \leq L_{\text{sea}}$ and $0\,\text{km} \leq y \leq B_{\text{sea}}$, with L_{sea} and B_{sea} the length and width of the part of the domain representing the sea. Initially, the bottom elevation in the basin and both inlets is uniformly set at $-H_{\text{b}}$ (with 0 representing mean sea level) and decreases from $y = 12\,\text{km}$ to $y = 7\,\text{km}$ linearly towards $-H_{\text{s}}$. For $y < 7\,\text{km}$ the bed level is uniformly set at $-H_{\text{s}}$.

A tidal wave enters the domain at the right side in fig. 2.1 and moves in time from right to left. Based on this movement, a 'downdrift' and an 'updrift' direction are defined, indicating movement along the tidal wave or against the tidal wave. Both the direction of the tidal wave and the directions are indicated in fig. 2.1. Following the definitions of downdrift and updrift direction, the basin is divided in a downdrift and an updrift sub-basin (see fig. 2.1).

2.1.2 Physical and numerical aspects of the model

In this study, the Delft3D numerical model is used, which is (in three-dimensional form) extensively described by Lesser et al. [2004]. Therefore, in this section, only the governing equations (following Lesser et al. [2004] and Deltares [2013]) and the choice of parameter values will be discussed. In this study, atmospheric effects such as storm surges are excluded, as are wave-effects (e.g., littoral drift). Moreover, the sediment implemented in the model consists of sand of only a single grain size (diameter D_{50}), which excludes e.g. sorting effects.

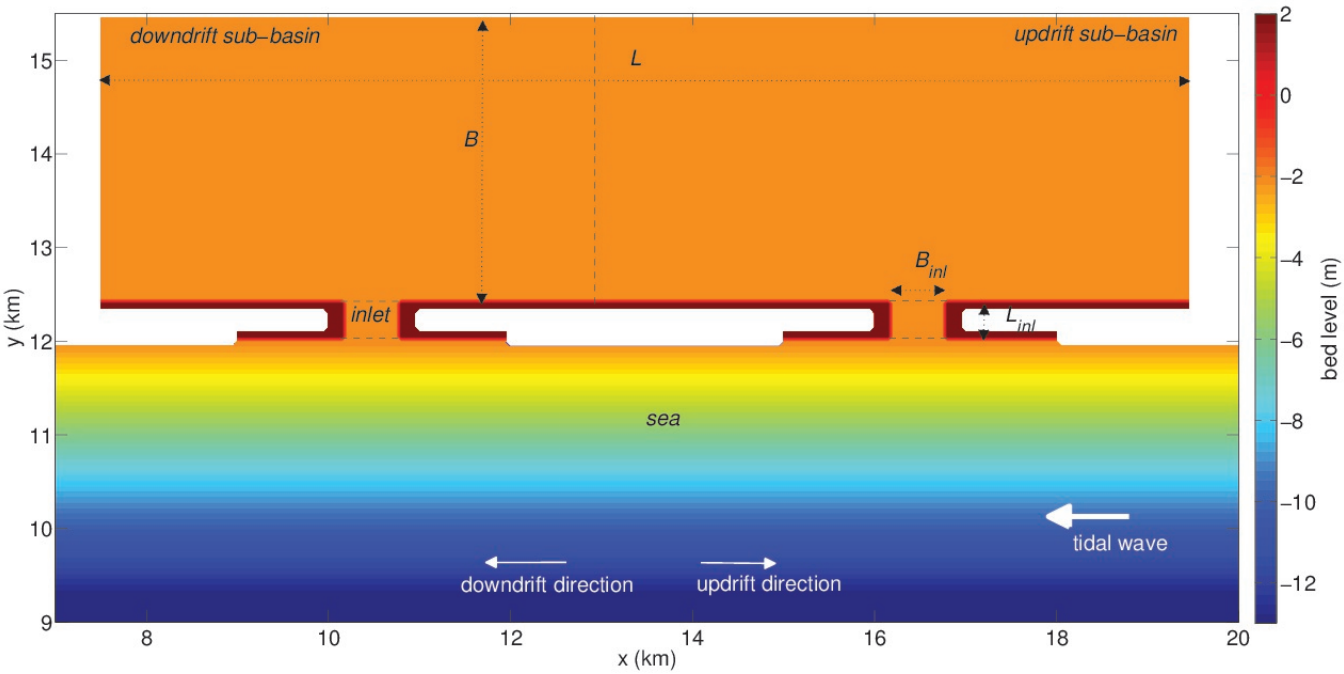

Figure 2.1: Colour plot of the initial bathymetry of the system, with 0 m indicating mean sea level. The length L and width B of the back-barrier basin are indicated by the dotted arrows, along with the initial length L_{inl} and width B_{inl} of the inlets. The different parts of the domain (sea, inlets and sub-basins) are separated by dashed lines. The thin white arrows indicate the definition of downdrift and updrift direction, and the thick white arrow denotes the direction of the longshore tidal wave.

Hydrodynamics

The hydrodynamics is described by the depth-averaged shallow water equations,

$$
\begin{aligned}
\frac{\partial \eta}{\partial t} + \frac{\partial hu}{\partial x} + \frac{\partial hv}{\partial y} &= 0\,, \\
\frac{\partial u}{\partial t} + u\frac{\partial u}{\partial x} + v\frac{\partial u}{\partial y} - fv &= -g\frac{\partial \eta}{\partial x} - C_{\mathrm{D}}\frac{u\sqrt{u^2+v^2}}{h} \\
&\quad + \frac{1}{h}\left[\frac{\partial}{\partial x}\left(\nu_{\mathrm{e}} h\frac{\partial u}{\partial x}\right) + \frac{\partial}{\partial y}\left(\nu_{\mathrm{e}} h\frac{\partial u}{\partial y}\right)\right]\,, \\
\frac{\partial v}{\partial t} + u\frac{\partial v}{\partial x} + v\frac{\partial v}{\partial y} + fu &= -g\frac{\partial \eta}{\partial y} - C_{\mathrm{D}}\frac{v\sqrt{u^2+v^2}}{h} \\
&\quad + \frac{1}{h}\left[\frac{\partial}{\partial x}\left(\nu_{\mathrm{e}} h\frac{\partial v}{\partial x}\right) + \frac{\partial}{\partial y}\left(\nu_{\mathrm{e}} h\frac{\partial v}{\partial y}\right)\right]\,.
\end{aligned}
\tag{2.1}
$$

Here, η is the sea surface elevation (compared to the undisturbed water depth H), h is the local water depth ($h = H + \eta$), u and v are the depth-averaged velocity components in x- and y-direction respectively of depth-averaged velocity vector $\mathbf{u}$, f is the Coriolis parameter, g is the gravity acceleration and ν_{e} is the eddy viscosity (which is assumed to be spatially uniform). Finally, C_{D} is a drag coefficient which is chosen to be $C_{\mathrm{D}} = g/C^2$, with C the (spatially uniform) Chézy coefficient. This results in a quadratic bed shear stress $\boldsymbol{\tau}_{\mathrm{b}}$, following Soulsby

[1997] described by

$$\boldsymbol{\tau}_{\mathrm{b}} = \rho C_{\mathrm{D}} \mathbf{u}|\mathbf{u}| \,, \tag{2.2}$$

where ρ is the density of water.

The model is forced by tidal wave consisting only of the principal lunar semi-diurnal (M2) tidal constituent, with frequency ω_2, amplitude A_2 and phase ϕ_2, travelling in the negative x-direction in the sea. To achieve this, the longshore domain boundary (at $y = 0\,\mathrm{km}$) is forced with a harmonic sea surface variation of constant amplitude A_2, and the cross-shore domain boundaries (at $x = 0\,\mathrm{km}$ and $x = 32.5\,\mathrm{km}$) are forced by the water level gradient $\partial\eta/\partial x$ (Neumann boundary condition), with frequency ω [Roelvink & Walstra, 2004]. Here the amplitude of the water level gradient ($A_{2,\mathrm{grad}}$) is determined by

$$A_{2,\mathrm{grad}} = \frac{2\pi}{\lambda_2} A_2 \,, \tag{2.3}$$

where the M2 tidal wavelength λ_2 is approximated by using

$$\lambda_2 = \frac{2\pi}{\omega_2} \sqrt{g H_{\mathrm{s}}} \,, \tag{2.4}$$

with H_{s} the (constant) initial offshore tidally-averaged water depth. The phase difference $\Delta\phi_2$ of the imposed water levels at the cross-shore boundaries is determined by

$$\Delta\phi_2 = \frac{L_{\mathrm{sea}}}{\lambda_2} \times 360^\circ \,. \tag{2.5}$$

For a travelling wave in the negative x-direction (downdrift), the phase of the water level gradient is $\phi_{2,\mathrm{grad}} = \phi_2 - 90^\circ$.

Sediment transport

For the sediment transport, the equations of Van Rijn [1993] are used, which distinguish both bedload transport ($\mathbf{q}_{\mathrm{b}}$) and suspended load transport ($\mathbf{q}_{\mathrm{s}}$). The latter is calculated as

$$q_{\mathrm{s},x} = uhc - hD_{\mathrm{H}} \frac{\partial c}{\partial x} \,, \qquad q_{\mathrm{s},y} = vhc - hD_{\mathrm{H}} \frac{\partial c}{\partial y} \,, \tag{2.6}$$

with D_{H} the horizontal eddy diffusion coefficient. The depth-averaged sediment concentration c is determined using a depth-averaged advection-diffusion equation,

$$\frac{\partial hc}{\partial t} + \frac{\partial huc}{\partial x} + \frac{\partial hvc}{\partial y} - \frac{\partial}{\partial x}\left(hD_{\mathrm{H}} \frac{\partial c}{\partial x}\right) - \frac{\partial}{\partial y}\left(hD_{\mathrm{H}} \frac{\partial c}{\partial y}\right) = \frac{w_{\mathrm{s}}(c_{\mathrm{eq}} - c)}{T_{\mathrm{sd}}} \,. \tag{2.7}$$

Here w_{s} is the sediment settling velocity, defined as

$$w_{\mathrm{s}} = \frac{10\nu}{D_{50}} \left[\sqrt{1 + \frac{0.01(\rho_{\mathrm{s}} - \rho) g D_{50}}{\rho \nu^2}} - 1 \right] \,. \tag{2.8}$$

In the above equations, T_{sd} is a parameter that depends on the bed shear stress and on the settling velocity, ν is the molecular viscosity of water, ρ_{s} is the density of the sediment particles (in $\mathrm{kg/m^3}$), D_{50} is the median sediment diameter (in m), and c_{eq} is the equilibrium concentration.

This last term is defined such that it leads to the same advective sediment transport as that due to a depth-dependent concentration ($\hat{c}(z)$) and velocity ($\hat{u}(z)$), described by Ridderinkhof et al. [2014a] as

$$\mathbf{u}c_{\mathrm{eq}} \equiv \int_0^h \hat{\mathbf{u}}(z)\hat{c}(z)\,\mathrm{d}z\,. \tag{2.9}$$

The velocity $\hat{u}$ is assumed to be logarithmic in the vertical, and following Van Rijn et al. [2001], $\hat{c}(z)$ is determined by the concentration at reference height a_{ref},

$$\begin{aligned} \hat{c}(a_{\mathrm{ref}}) &= 0.015\frac{D_{50}T_{\mathrm{r}}^{1.5}}{a_{\mathrm{ref}}D_*^{0.3}}\,, \\ a_{\mathrm{ref}} &= \min\left[\max\left(k, 0.01h\right), 0.2h\right]\,. \end{aligned} \tag{2.10}$$

and assuming that in equilibrium the sediment obeys a Rouse profile above the reference height (as mentioned in e.g. Ridderinkhof et al. [2014a]). Here, k is a roughness height (in m) depending on the local current speed and the sediment characteristics, and D_* is a dimensionless sediment diameter, defined as

$$D_* = D_{50}\left[\frac{(\rho_{\mathrm{s}}-\rho)g}{\rho\nu^2}\right]^{1/3}\,. \tag{2.11}$$

The dimensionless bed shear stress T_{r} is given by

$$T_{\mathrm{r}} = \max\left(\frac{|\boldsymbol{\tau}_{\mathrm{b}}|}{\tau_{\mathrm{cr}}} - 1, 0\right)\,, \tag{2.12}$$

where τ_{cr} the critical shear stress: the minimum magnitude of the bed shear stress $\boldsymbol{\tau}_{\mathrm{b}}$ needed for the initiation of sediment particle motion. This critical shear stress is calculated in the model by

$$\tau_{\mathrm{cr}} = (\rho_{\mathrm{s}}-\rho)gD_{50}\theta_{\mathrm{cr}}\,, \tag{2.13}$$

where τ_{cr} is the critical Shields parameter, which is for the chosen sediment diameter in this research parameterised by $\theta_{\mathrm{cr}} = 0.14D_*^{-0.64}$.

The bedload transport $\mathbf{q}_{\mathrm{b}}$ is calculated from the depth-averaged velocity $\mathbf{u}$, the bed shear stress τ_{b} and the local bed slope,

$$\begin{aligned} q_{\mathrm{b},x} &= \frac{D_{50}D_*^{-0.3}T_{\mathrm{r}}\alpha_{\mathrm{s}}}{2\sqrt{|\boldsymbol{\tau}_{\mathbf{b}}|\rho}}\left(\tau_{\mathrm{b},x} - \alpha_{\mathrm{BN}}\sqrt{\frac{\tau_{\mathrm{cr}}}{|\boldsymbol{\tau}_{\mathbf{b}}|}}\frac{\partial z_{\mathrm{bed}}}{\partial n}\tau_{\mathrm{b},y}\right)\,, \\ q_{\mathrm{b},y} &= \frac{D_{50}D_*^{-0.3}T_{\mathrm{r}}\alpha_{\mathrm{s}}}{2\sqrt{|\boldsymbol{\tau}_{\mathbf{b}}|\rho}}\left(\tau_{\mathrm{b},y} - \alpha_{\mathrm{BN}}\sqrt{\frac{\tau_{\mathrm{cr}}}{|\boldsymbol{\tau}_{\mathbf{b}}|}}\frac{\partial z_{\mathrm{bed}}}{\partial n}\tau_{\mathrm{b},x}\right)\,. \end{aligned} \tag{2.14}$$

Here, $\partial z_{\mathrm{bed}}/\partial n$ is the bed slope perpendicular to the local flow and α_{BN} is a coefficient which is discussed in Dissanayake et al. [2009]. Furthermore, α_{s} is a function of the slope in the along current direction defined as

$$\alpha_{\mathrm{s}} = 1 + \alpha_{\mathrm{BS}}\left[\frac{\tan(\varphi_{\mathrm{fric}})}{\cos\left(\tan^{-1}(\frac{\partial z_{\mathrm{bed}}}{\partial s})\right)\left(\tan(\varphi_{\mathrm{fric}}) - \frac{\partial z_{\mathrm{bed}}}{\partial s}\right)} - 1\right]\,, \tag{2.15}$$

with α_{BS} a prescribed coefficient, φ_{fric} the internal angle of friction of bed material (assumed to be constant) and $\partial z_{\mathrm{bed}}/\partial n$ the bed slope in the direction of the local flow.

The bed level change is purely a function of divergence of bedload sediment transport and of net exchange of suspended sediment between water column and bed,

$$\frac{\partial H}{\partial t} = \frac{1}{1-p}\left(\frac{\partial q_{\mathrm{b},x}}{\partial x} + \frac{\partial q_{\mathrm{b},y}}{\partial y} + \frac{w_{\mathrm{s}}(c_{\mathrm{eq}} - c)}{T_{\mathrm{sd}}}\right) . \tag{2.16}$$

Here, p is the porosity of the bed.

Numerical aspects

The above described equations are solved on a rectilinear staggered grid. Length L and width B of the basin are fixed, as are the dimensions of the sea. Different locations of the inlets are used during this research, with a distance Δx_{inl} between the two inlets. To solve the equations discussed earlier, a time step of Δt is used with an alternating direction implicit scheme. For the spatial discretisation, a cyclic method is applied. To make the model runs less computationally expensive, the domain is split into three separate (but interacting) parts, that run parallel. The first part consists of the updrift half of the basin with the associated inlet and nearshore sea. The second consists of the downdrift half of the basin with the associated inlet and nearshore sea. The last part consists of the parts of the sea that are far removed from the inlets.

At each time step, the bed level change that results from eq. (2.16) is multiplied by a morphological factor f_{M} [Lesser et al., 2004] and the bed level is updated. A morphological factor is used to reduce computational time, because morphological changes take place on much longer timescales ($\sim$ years) than hydrodynamic changes (tidal period $\sim 12.5\,\mathrm{h}$). Using a morphological factor introduces an error in the calculated bed level. In order to reduce computational time, but keep this error acceptable, f_{M} is increased in several steps, leading to an initially small value of f_{M}, when the morphological changes are the largest (when starting from a flat bathymetry).

When the local water depth $h < 0.1\,\mathrm{m}$ in a computation cell, the cell is considered to be a dry cell. To allow for dry cells (initially present or cells that become dry during the model run) to be eroded, a scheme described by Van der Wegen & Roelvink [2008] is used. According to this scheme, all eroded sediment from a wet computational cell adjacent to a dry cell, is actually eroded from the dry cell, but further dealt with as if eroded from the wet cell. This process can continue until the dry cell turns into a wet cell itself.

Model set-up

As a reference case, of which the hydrodynamics and morphological evolution of the bed will be extensively studied, a model experiment is designed with parameter setting as listed in table 2.1 (research question 1). This reference case will be used to compare the results for different inlet spacing and for an instant lowering of the bed with. The values of the morphological factor f_{M}, that is increased in several steps, are listed in table 2.2. This experiment is continued up to 185 yr of morphological evolution, because by than the morphological changes of the bed are very small compared to earlier values during the simulation.

The grid resolution is maximum in the basin and inlets, where a constant resolution of $(1/50)\,\mathrm{m}^{-1}$ is applied in both x- and y-direction. Such high resolution is used to be able to solve the expected development of the channel structure in detail. Furthermore, the width of

the inlets consists of at least 10 grid cells, which makes it possible to resolve the morphologic development of the inlets in reasonable detail. The resolution decreases away from the tidal inlets to a minimum of $(1/850)\,\mathrm{m}^{-1}$ in the x-direction and $(1/600)\,\mathrm{m}^{-1}$ in the y-direction.

To make it possible for the model to widen the inlets, just below $y = 12.5\,\mathrm{km}$ (seaward boundary of the basin) three rows of initially dry cells are added (2 m above mean sea level). Futhermore, left and right of each inlet erodible banks are located (width of 5 grid cells, 2 m above mean sea level), which are also initially dry. Finally, at the seaward side of each inlet, both left and right, erodible banks are added of dimensions 15×3 grid cells. These erodible banks, whose location is also indicated by the dark red bands in fig. 2.1, prevent extreme erosion of the bottom in the inlet that takes place when the banks are fixed. Note that only the erodible banks located at the edge of the barrier islands can be eroded, so islands cannot disappear.

L	12 km	ω_2	$1.405 \times 10^{-4}\,\mathrm{s}^{-1}$
B	3 km	A_2	1 m
L_{inl}	500 m	D_{H}	$25\,\mathrm{m}^2\mathrm{s}^{-1}$
B_{inl}	500 m	ρ	$1000\,\mathrm{kg\ m}^{-3}$
L_{sea}	32.5 km	ρ_{s}	$2.65 \times 10^3\,\mathrm{kg\ m}^{-3}$
B_{sea}	12 km	ν	$1.14 \times 10^{-6}\,\mathrm{m}^2\mathrm{s}^{-1}$
Δx_{inl}	6 km	D_{50}	$200\,\mu\mathrm{m}$
H_{b}	-2 m	α_{BS}	1
H_{s}	-20 m	α_{BN}	20
f	$8.8 \times 10^{-5}\,\mathrm{s}^{-1}$	φ_{fric}	$30°$
g	$9.81\,\mathrm{m\ s}^{-2}$	p	0.4
C	$65\,\mathrm{m}^{1/2}\mathrm{s}^{-1}$	Δt	9 s
ν_{e}	$25\,\mathrm{m}^2\mathrm{s}^{-1}$		

Table 2.1: Dimensions and parameter setting of the reference model.

time (M2 periods)	time (years)	f_{M}
0	0	0
8	0	5
30	0.16	10
60	0.58	25
1340	46	50

Table 2.2: Overview of times at which a new value of f_{M} is applied, both in number of M2 tidal periods and in years of morphological evolution.

To study the effect of the distance between the two inlets on the asymmetry of the total tidal inlet system (research question 2), the configuration of the reference experiment is adapted only by changing distance Δx_{inl}. In addition to $\Delta x_{\mathrm{inl}} = 6\,\mathrm{km}$ of the reference case (table 2.1), experiments with $\Delta x_{\mathrm{inl}} = 9\,\mathrm{km}$ (inlets far apart, in short called 'far') and $\Delta x_{\mathrm{inl}} = 3\,\mathrm{km}$ (inlets close together, in short called 'close') are designed. In each experiment, the inlets are located symmetrically with respect to the geometrical centre of the basin.

Lastly, to study the effect of a sudden lowering of the bed level in the basin (research question 3), three different experiments are designed. Each of them starts with the final bathymetry of the reference run (after 185 yr), where the bed level in the basin is lowered according to a

two-dimensional Gaussian function,

$$\Delta H(x,y) = a \exp\left[-\frac{(x-\mu_x)^2}{2\sigma_x^2} - \frac{(y-\mu_y)^2}{2\sigma_y^2}\right]. \tag{2.17}$$

In this expression, a is the peak height (in m), (μ_x, μ_y) are the coordinates of the centre of the peak (in km) and σ_x and σ_y the standard deviations in x- and y-direction, respectively. Three different cases are considered to study both the effect of location and of intensity of lowering: 1.) maximum lowering of 1 m in the updrift basin (in short called '1 m updrift'), 2.) maximum lowering of 2 m in the updrift basin (in short called '2 m updrift'), and 3.) maximum lowering of 1 m in the centre of the basin (in short called '1 m centre'). Values for the parameters in eq. (2.17) for these three cases are given in table 2.3. Each of these runs continues up to 255 yr, which means a duration of 70 yr after lowering of the bed level ($t = 185$ yr). After these 70 yr the morphological changes are small compared to the initial changes. To be able to distinguish effects of the lowering from the evolution that would also be present without lowering of the bed level, the reference run (discussed earlier) is also continued for another 70 yr.

run	Parameters of Gaussian lowering of the bed level				
1 m updrift	$a = 1$ m	$\mu_x = 16.5$ km	$\mu_y = 14.5$ km	$\sigma_x = 1$ km	$\sigma_y = 1$ km
2 m updrift	$a = 2$ m	$\mu_x = 16.5$ km	$\mu_y = 14.5$ km	$\sigma_x = 1$ km	$\sigma_y = 1$ km
1 m centre	$a = 1$ m	$\mu_x = 13.5$ km	$\mu_y = 13.0$ km	$\sigma_x = 1$ km	$\sigma_y = 1$ km

Table 2.3: Parameter setting of the two-dimensional Gaussian surface for lowering the bed level, eq. (2.17).

2.1.3 Analytical model

Apart from the numerical model described above, an analytical model will be used to explain certain observations in the numerical model results. This model is described by Ridderinkhof [1988] and Buijsman & Ridderinkhof [2007], and will be shortly introduced here. For a more extensive discussion, including some corrections to the original publications, the reader is referred to appendix A.

The used analytical model is based on the depth-averaged one-dimensional shallow water equations, in terms of water volume transport Q (instead of velocity, which is the case in the numerical model) and non-dimensional. The friction is linearised, a constant density is assumed, and no atmospheric effects are taken into account (e.g., no wind stress). Furthermore, no sediment transports are calculated and the bed level is kept constant. The domain of this analytical model consists of a single channel with two open ends, representing the inlets. Both ends are forced with a single harmonic component of sea level elevation, with a phase difference ϕ between the inlets. The channel consists of two sides, comparable to the updrift and downdrift sub-basin in the numerical model.

Relevant dimensional scales in the analytical model are the width (B_A), the length (L_A) and the depth (H_A) of the updrift channel, together with the imposed sea level amplitude at the updrift open boundary (Z_A). These parameters are converted to the downdrift situation by multiplying with dimensionless parameters b' ℓ', h' and Z', respectively.

2.2 Methods

2.2.1 Harmonic analysis and the tidal ellipse

To be able to analyse the effect of tidal asymmetry generated in the tidal basin (discussed later on), a harmonic analysis is applied to decompose the original time series of different variables into components attributed to the residual value (M0), the M2 tidal component, and its multiples M4, M6, ... The amplitudes and phases of the different components of for instance sea level η satisfy

$$\eta(t) = \sum_n |\eta_n| \cos\left(\tfrac{n}{2}\omega_2 t - \phi_n\right) , \qquad n = 0, 2, 4, \ldots, n_{\text{freq}} . \tag{2.18}$$

Here $n = 0$ denotes the residual component (with by definition $\phi_0 = 0$), and $n \geq 2$ denotes amplitudes and phases of tidal components Mn. To avoid effects of aliasing on higher order tidal components, the tidal frequencies taken into account should be smaller than the so-called Nyquist frequency $f_{\text{N}} = \frac{1}{2\Delta t}$ (half the sampling frequency). Therefore, only tidal components with periods $T_n > 2\Delta t$ are allowed, with Δt the time step in the output of the numerical model. The minimum period T_n that is allowed according to this criterium defines n_{freq} in eq. (2.18). It should be noted that when shoals get partly submerged, the calculated tidal components should be interpreted with care. For that reason, the M2 and higher order harmonics are only shown for grid cells where $H - |\min(\eta_n)| > 0.1\,\text{m}$. This value of 0.1 m is the actual water depth below which the model treats a cell as dry.

From the harmonic components of both longshore and cross-shore velocity (u and v, respectively), the so-called tidal ellipse can be constructed, for each harmonic component. Due to the sinusoidal behaviour of both u and v, the velocity vector $\mathbf{u}$ describes an elliptic path. This way, a tidal ellipse is described by four amplitude and phase lag parameters U_n, $\psi_{u,n}$, V_n and $\psi_{v,n}$ being amplitude and phase of u- and v-components, respectively,

$$u = U_n \cos(\omega_n t - \psi_{u,n}) , \qquad v = V_n \cos(\omega_n t - \psi_{v,n}) . \tag{2.19}$$

The subscript n again denotes which harmonic component is considered, with $n = 0, 2, 4, \ldots$ corresponding to the M0, M2, M4, ... components. Note that the tidal frequency for each component is given by $\omega_n = \frac{n}{2}\omega_2$. In the following derivation, the subscript n will be left out for clarity of notation. However, the same procedure holds for each harmonic component.

Following Prandle [1982], a tidal ellipse can also be described by two opposite rotating circular radial vectors by introducing a complex velocity $w = u + \mathrm{i}v$. It turns out that

$$\begin{aligned} w &= U\cos(\omega t - \psi_u) + \mathrm{i}V\cos(\omega t - \psi_v) \\ &= w_{\text{p}}\mathrm{e}^{\mathrm{i}\omega t} + w_{\text{m}}\mathrm{e}^{-\mathrm{i}\omega t} \\ &= W_{\text{p}}\mathrm{e}^{\mathrm{i}(\omega t + \theta_{\text{p}})} + W_{\text{m}}\mathrm{e}^{-\mathrm{i}(\omega t - \theta_{\text{m}})} , \end{aligned} \tag{2.20}$$

with new notations w_{p}, w_{m}, W_{p} and W_{m} described by

$$\begin{aligned} w_{\text{p}} &= \frac{U\mathrm{e}^{-\mathrm{i}\psi_u} + \mathrm{i}V\mathrm{e}^{-\mathrm{i}\psi_v}}{2} \equiv W_{\text{p}}\mathrm{e}^{\mathrm{i}\theta_{\text{p}}} , \\ w_{\text{m}} &= \frac{U\mathrm{e}^{\mathrm{i}\psi_u} + \mathrm{i}V\mathrm{e}^{\mathrm{i}\psi_v}}{2} \equiv W_{\text{m}}\mathrm{e}^{\mathrm{i}\theta_{\text{m}}} . \end{aligned} \tag{2.21}$$

This indeed describes an ellipse composed of two opposite rotating circular radial vectors, as is visualised in fig. 2.2.

Using the two-circle definition of an ellipse, a tidal ellipse can be described by four new parameters: *semi-major axis* (SEMA), *eccentricity* (ECC), *inclination* (INC) and *phase* (θ) which are mathematically defined as

$$\begin{aligned}
\mathrm{SEMA} &= \max|w| = W_\mathrm{p} + W_\mathrm{m}\,, \\
\mathrm{ECC} &= \frac{\mathrm{SEMI}}{\mathrm{SEMA}} = \frac{\min|w|}{\max|w|} = \frac{W_\mathrm{p} - W_\mathrm{m}}{W_\mathrm{p} + W_\mathrm{m}}\,, \\
\mathrm{INC} &= \arg\left(w_\mathrm{max}\right) = \frac{\theta_\mathrm{m} + \theta_\mathrm{p}}{2} + r\pi\,, \\
\theta &= \omega t_\mathrm{max} = \frac{\theta_\mathrm{m} - \theta_\mathrm{p}}{2} + r\pi\,,
\end{aligned} \tag{2.22}$$

in which SEMI indicates the semi-minor axis of the ellipse. The factor r is fixed by using the northern axis convention [Foreman, 1978],

$$r = \mathrm{int}\left[\frac{\frac{\theta_\mathrm{m}+\theta_\mathrm{p}}{2} + 2\pi \pmod{2\pi}}{\pi}\right]\,, \tag{2.23}$$

with int a function that takes the integer part of the argument.

The above defined tidal ellipse parameters are interpreted as described next, following Xu [2002]. The semi-major axis SEMA is the maximum current velocity during a tidal cycle ($|\mathrm{OP}|$ in fig. 2.2). The eccentricity ECC is the ratio of semi-minor axis over semi-major axis (ratio $|\mathrm{OQ}|/|\mathrm{OP}|$ in fig. 2.2), so $0 < \mathrm{ECC} \leq 1$ with $\mathrm{ECC} = 1$ indicating a circular velocity-path. Additionally, a sign is assigned to the eccentricity, due to the fact that in above definitions the semi-minor axis SEMI is negative for $W_\mathrm{m} > W_\mathrm{p}$. A positive (negative) eccentricity indicates that the ellipse is traversed in anti-clockwise (clockwise) direction. The inclination INC is the angle (in radians) between the positive u-axis and the semi-major axis, with (according to Foreman [1978]) only the semi-major axis with $v \geq 0$ taken into account, resulting in the interval $[0, \pi]$. Finally, the phase θ indicates the time t_max at which the maximum current occurs for $v \geq 0$, i.e. $\theta = \frac{2\pi}{T} t_\mathrm{max}$ (T being the tidal period). In accordance with the northern axis convention of Foreman [1978], the phase is indicated in the interval $[0, 2\pi]$, but (because a maximum current is reached twice per tidal period) the phase will be mostly indicated in the interval $[0, \pi]$ in this thesis. In fig. 2.2, the phase is $\angle$ROP or $\angle$GOP.

2.2.2 Weighted centre of channel volume

The weighted centre of channel volume in the back-barrier basin (x_{CM}, y_{CM}) is defined as the 1st-order moment ($M_x^{(1)}$, $M_y^{(1)}$) of channel volume (with larger depth than initially, so $H < -2\,\mathrm{m}$) divided by the total volume of the channels, i.e.

$$\begin{aligned}
x_\mathrm{CM} &\equiv M_x^{(1)}/M^{(0)} = \frac{1}{V_\mathrm{c}} \int\limits_{\substack{\mathrm{basin} \\ H<-2\,\mathrm{m}}} x H(x,y)\,\mathrm{d}x\,\mathrm{d}y\,, \\
y_\mathrm{CM} &\equiv M_y^{(1)}/M^{(0)} = \frac{1}{V_\mathrm{c}} \int\limits_{\substack{\mathrm{basin} \\ H<-2\,\mathrm{m}}} y H(x,y)\,\mathrm{d}x\,\mathrm{d}y\,,
\end{aligned} \tag{2.24}$$

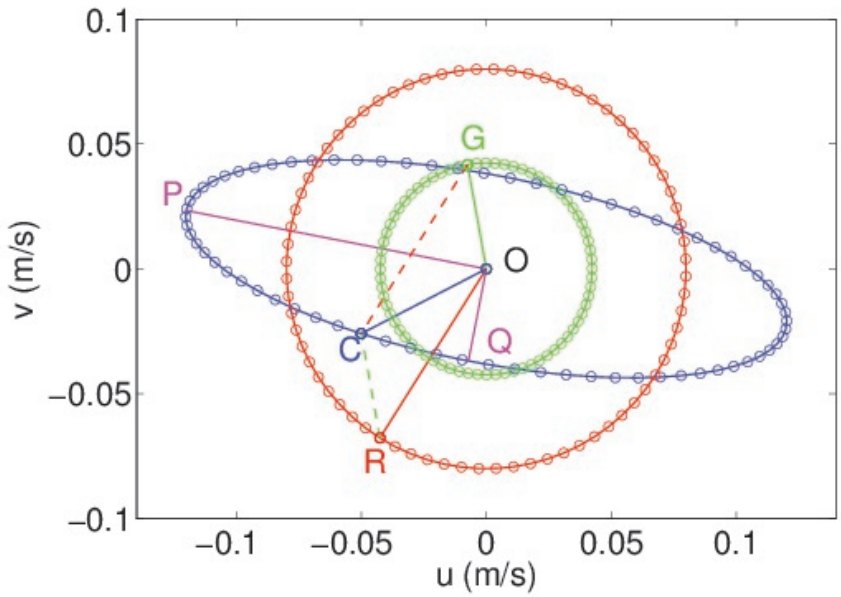

Figure 2.2: An example of a tidal ellipse (blue curve), with results from point R rotating over the red circle in clockwise and point G over the green one in anti-clockwise direction. The actual velocity vector is indicated by OC and the maximum current by OP. (based on [Xu, 2002])

where the total channel volume (being the 0th-order moment, $M^{(0)}$) is defined as

$$V_{\text{c}} \equiv M^{(0)} = \int\limits_{\substack{\text{basin} \\ H<-2\,\text{m}}} H(x,y)\,\mathrm{d}x\,\mathrm{d}y\,. \tag{2.25}$$

This weighted centre of channel volume can be thought of as the centre of mass of a mould of the channel volume. Therefore, the weighted centre of channel volume will from now on simply be called the centre of mass of the channels.

A measure of the spreading of the channels is defined as the 2nd-order central moment ($\tilde{M}_x^{(2)}$, $\tilde{M}_y^{(2)}$) of channel volume divided by the total volume of the channels, viz.

$$\begin{aligned} \text{var}[x] &\equiv \tilde{M}_x^{(2)}/M^{(0)} = \frac{1}{V_{\text{c}}} \int\limits_{\substack{\text{basin} \\ H<-2\,\text{m}}} (x - x_{\text{CM}})^2 H(x,y)\,\mathrm{d}x\,\mathrm{d}y\,, \\ \text{var}[y] &\equiv \tilde{M}_y^{(2)}/M^{(0)} = \frac{1}{V_{\text{c}}} \int\limits_{\substack{\text{basin} \\ H<-2\,\text{m}}} (y - y_{\text{CM}})^2 H(x,y)\,\mathrm{d}x\,\mathrm{d}y\,. \end{aligned} \tag{2.26}$$

For simplicity, this will be called the 'variance' of the channel volume, after its probabilistic analog.

2.2.3 Sediment exchange between compartments

The total tidal inlet system considered in this research consists of a sea, two inlets and a back-barrier basin. The latter consists of an updrift sub-basin and a downdrift sub-basin, each

belonging to one inlet. In order to determine the volumetric sediment exchange rate (q, in m^3/s) between the different compartments of the system, the mean has to be taken over several tidal periods. However, this requires a time step in the output data which is of the same order as the computational time step during the whole simulation, which is computationally expensive. A more efficient method is to determine the volumetric sediment exchange rate from the time evolution of the total volume of deposited sediment (S, in m^3) and the porosity (p) using

$$\begin{aligned} (1-p)\frac{\mathrm{d}S_\mathrm{i}^\mathrm{u}}{\mathrm{d}t} &= q_\mathrm{si}^\mathrm{u} - q_\mathrm{ib}^\mathrm{u}\,, & (1-p)\frac{\mathrm{d}S_\mathrm{b}^\mathrm{u}}{\mathrm{d}t} &= q_\mathrm{ib}^\mathrm{u} + q_\mathrm{du}\,, \\ (1-p)\frac{\mathrm{d}S_\mathrm{i}^\mathrm{d}}{\mathrm{d}t} &= q_\mathrm{si}^\mathrm{d} - q_\mathrm{ib}^\mathrm{d}\,, & (1-p)\frac{\mathrm{d}S_\mathrm{b}^\mathrm{d}}{\mathrm{d}t} &= q_\mathrm{ib}^\mathrm{d} - q_\mathrm{du}\,. \end{aligned} \tag{2.27}$$

Here, the sediment exchange rates are defined as: from sea to updrift inlet (q_si^u), from updrift inlet to updrift sub-basin (q_ib^u), from sea to downdrift inlet (q_si^d), from downdrift inlet to downdrift sub-basin (q_ib^d) and from downdrift to updrift sub-basin (q_du). Furthermore, the total volume of deposited sediment is defined in the updrift inlet (S_i^u), the updrift sub-basin (S_b^u), the downdrift inlet (S_i^d) and the downdrift sub-basin (S_b^d). These variables are shown in fig. 2.3.

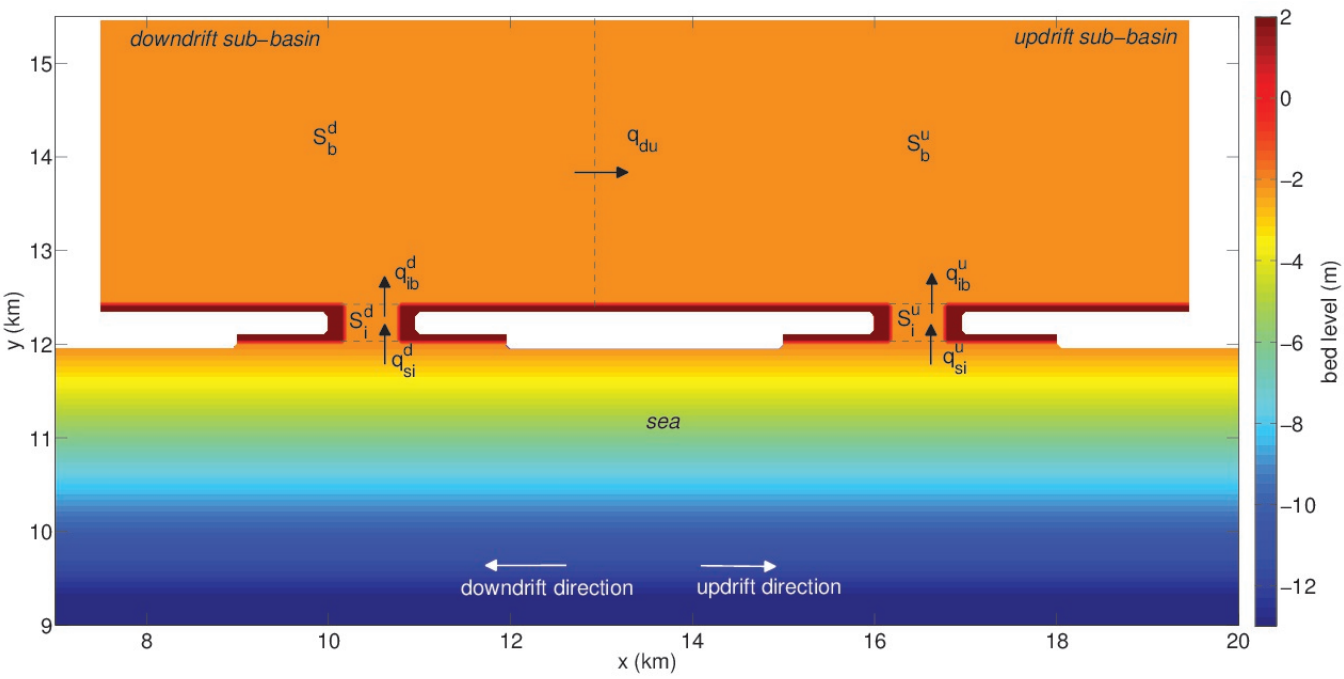

Figure 2.3: Colour plot of the initial bathymetry of the system, with 0 m indicating mean sea level. The different parts of the domain (sea, inlets and sub-basins) are separated by dashed lines. The symbols S and q (with sub- and superscripts) of eq. (2.27) are shown, denoting total deposited sediment (in m^3) in each part of the domain and sediment exchanges rates between different parts of the domain (in m^3/s), respectively.

Note that there are four variables denoting deposited sediment (S) and five denoting sediment exchange rates (q). This results in an underdetermination of this system of equations when using it for calculation of the sediment exchange rates. As will be shown later, the sediment exchange between the sub-basins is negligible compared to the other sediment exchanges ($|q_\mathrm{du}| \ll |q_\mathrm{si}^\mathrm{u}|$, $|q_\mathrm{ib}^\mathrm{u}|$, $|q_\mathrm{si}^\mathrm{d}|$, $|q_\mathrm{ib}^\mathrm{d}|$). As a result, only four variables q are left, and can be determined

as follows:

$$
\begin{aligned}
q_{\mathrm{ib}}^{\mathrm{u}} &\approx (1-p)\frac{\mathrm{d}S_{\mathrm{b}}^{\mathrm{u}}}{\mathrm{d}t}\,, & q_{\mathrm{si}}^{\mathrm{u}} &\approx (1-p)\frac{\mathrm{d}(S_{\mathrm{i}}^{\mathrm{u}}+S_{\mathrm{b}}^{\mathrm{u}})}{\mathrm{d}t}\,,\\
q_{\mathrm{ib}}^{\mathrm{d}} &\approx (1-p)\frac{\mathrm{d}S_{\mathrm{b}}^{\mathrm{d}}}{\mathrm{d}t}\,, & q_{\mathrm{si}}^{\mathrm{d}} &\approx (1-p)\frac{\mathrm{d}\left(S_{\mathrm{i}}^{\mathrm{d}}+S_{\mathrm{b}}^{\mathrm{d}}\right)}{\mathrm{d}t}\,.
\end{aligned}
\tag{2.28}
$$

Note, however, that this is only an approximation. When a small net sediment flux between the basins is present in the downdrift direction ($q_{\mathrm{du}} < 0$), on can expect a slight underestimation of the fluxes in the updrift part, and an overestimation in the downdrift part. When $q_{\mathrm{du}} > 0$ the opposite is expected.

2.2.4 Tidal asymmetry

Due to nonlinear terms in the equations of motion, tides will be asymmetrical in terms of currents and sediment transport, even if the system is forced by a symmetrical tide. A tidal inlet is flood (ebb) dominant if maximum flood (ebb) currents are larger than maximum ebb (flood) currents and if the flood (ebb) period has a shorter duration [Friedrichs & Aubrey, 1988]. The main source of tidal asymmetry is due to joint action of the M2 tidal component and its even overtides (M4, M6, ...) [Fry & Aubrey, 1990].

In order to quantify the effect of tidal asymmetry and of the mean flow on the net transport of coarse sediment, a simple formulation for the sediment transport is adopted in eq. (2.29), viz.

$$
q_x = \hat{q}\left(u^2+v^2\right)u\,, \qquad q_y = \hat{q}\left(u^2+v^2\right)v\,. \tag{2.29}
$$

Here, $\hat{q}$ is a constant with units $\mathrm{s^2m^{-1}}$, u and v are velocities in x- and y-direction, respectively, and q_x and q_y are sediment transports in both directions. Furthermore, using eq. (2.18) up to and including the M4 component, u and v are decomposed as

$$
\begin{aligned}
u &\approx u_0 + u_2\cos(\omega_2 t - \psi_{u,2}) + u_4\cos(2\omega_2 t - \psi_{u,4})\,,\\
v &\approx v_0 + v_2\cos(\omega_2 t - \psi_{v,2}) + v_4\cos(2\omega_2 t - \psi_{v,4})\,,
\end{aligned}
\tag{2.30}
$$

with the subscripts indicating the harmonic components and residual component, ω_2 indicating the M2 angular velocity (in radians), and $\psi_{u,n}$ and $\psi_{v,n}$ the phase of u- and v-components, respectively, for harmonic component Mn. Extending the one-dimensional approach of Van de Kreeke & Robaczewska [1993] to two dimensions, it is assumed that u_0/u_2, u_4/u_2, v_0/v_2 and v_4/v_2 are $\mathcal{O}(\varepsilon)$, with $\varepsilon \ll 1$. Combining eq. (2.29)–(2.30), neglecting terms of $\mathcal{O}(\varepsilon^3)$ or smaller and averaging over the M2 tidal period (indicated by $\langle . \rangle$) results in

$$
\begin{aligned}
\langle q_x\rangle \approx \hat{q}\Bigg[&\frac{3}{2}u_0u_2^2 + \frac{1}{2}u_0v_2^2 + v_0u_2v_2\cos(\psi_{u,2}-\psi_{v,2}) + \frac{3}{4}u_2^2u_4\cos(\psi_{u,4}-2\psi_{u,2})\\
&+\frac{1}{4}v_2^2u_4\cos(\psi_{u,4}-2\psi_{v,2}) + \frac{1}{2}u_2v_2v_4\cos(\psi_{u,2}+\psi_{v,2}-\psi_{v,4})\Bigg]\,,\\
\langle q_y\rangle \approx \hat{q}\Bigg[&\frac{3}{2}v_0v_2^2 + \frac{1}{2}v_0u_2^2 + u_0u_2v_2\cos(\psi_{u,2}-\psi_{v,2}) + \frac{3}{4}v_2^2v_4\cos(\psi_{v,4}-2\psi_{v,2})\\
&+\frac{1}{4}u_2^2v_4\cos(\psi_{v,4}-2\psi_{u,2}) + \frac{1}{2}u_2v_2u_4\cos(\psi_{u,2}+\psi_{v,2}-\psi_{u,4})\Bigg]\,.
\end{aligned}
\tag{2.31}
$$

For both x- and y-component in eq. (2.31), the first three terms on the right-hand side are due to joint action of the residual and M2 components (residual flow) and the last three terms are due to joint action of the M2 and M4 components (tidal asymmetry). When taking into account additional higher harmonics in eq. (2.30), the result of eq. (2.31) remains the same (not shown here), because additional terms are either zero or maximum of $\mathcal{O}(\varepsilon^3)$ if those additional harmonics have amplitudes much smaller than that of M2.

3. Results

3.1 Temporal evolution: reference case

3.1.1 Division into two sub-systems

Tidal waves entering the basin through both inlets will meet in the basin, and cause a minimum in the velocity amplitude somewhere in the centre of the basin. This suggests that the total basin can be divided into two sub-basins.

In order to define a boundary between these two sub-basins, the maximum of the absolute longshore velocity component, averaged over the width B of the basin, is plotted as a function of longshore coordinate x (see fig. 3.1). It turns out that minima occur at the location of both inlets, and somewhere in the middle of the basin. However, the location of this minimum does not coincide with the geometrical centre of the basin. This is caused by the phase difference of the tidal wave (of 3°) between the two inlets. The indicated minima occur at $x = 13.15\,\mathrm{km}$, $x = 12.9\,\mathrm{km}$, $x = 13.05\,\mathrm{km}$, $x = 12.8\,\mathrm{km}$ and $x = 12.75\,\mathrm{km}$ at the initial state and after 20, 50, 100 and 185 yr, respectively. Based on the final stage (after 185 yr), the downdrift sub-basin is defined by all grid cells of the basin up to 12.75 km, and the updrift sub-basin by all grid cells from 12.8 km onwards. Note that the smooth shape of the curve for $t = 0\,\mathrm{yr}$ is caused by the uniform initial depth.

Based on the location of the channels and the shoals, the boundary between the two sub-basins appears to be located between the computational grid cels at 12.85 and 12.9 km. This is in good agreement with the just defined division of the two sub-basins, based on the values obtained from fig. 3.1.

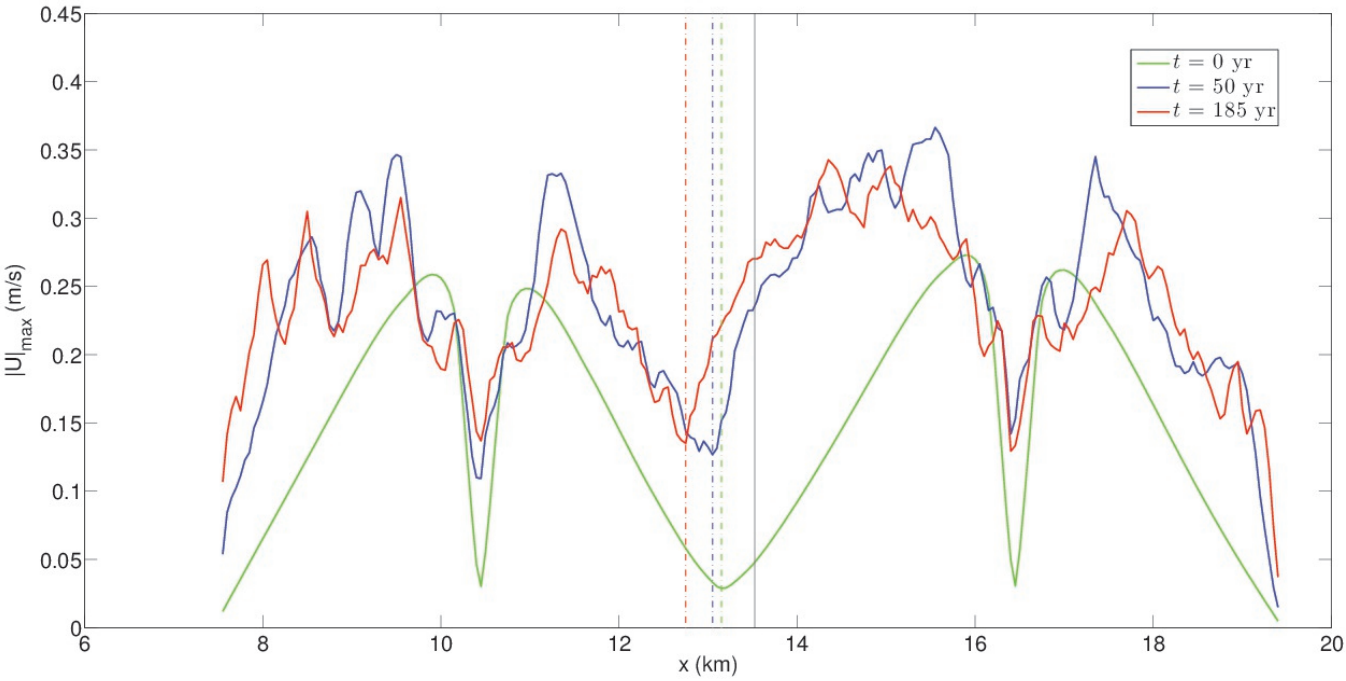

Figure 3.1: The maximum of the absolute longshore velocity $|U|_{\max}$ in the basin, averaged over the basin width. Different times are indicated by the colours, where green indicates the initial state (so no morphological evolution yet), blue 50 yr and red 185 yr.
The minimum is attained in the middle part of the basin (between $x = 11$ and 15 km), with the x-values of the minima given by the dashed-dotted lines. The geometrical centre of the basin is given by the solid black line.

3.1.2 Morphology

In order to capture the main morphological features, figs. 3.2 and 3.3 show the bed level elevation (with respect to the undisturbed sea level) and the change therein (with respect to the initial bed level of 2 m below mean sea level), respectively, at different times. Starting from an initially flat bathymetry in the inlet and the back-barrier basin and a linearly sloping bottom in the nearshore sea, as was introduced in fig. 2.1, both inlets start to deepen. Furthermore, channels and shoals appear in the basin, and sediment is deposited on ebb-tidal deltas that are located seaward of the inlets (figs. 3.2 and 3.3). These ebb-tidal deltas are located somewhat updrift compared to the inlets and are sickle-shaped. During the morphological evolution, the ebb-tidal deltas grow both in area and in volume. Besides this growth, a shift in the updrift direction occurs of especially the downdrift delta. Fig. 3.3 shows another interesting feature, namely an extension of the updrift ebb-tidal delta in the downdrift direction and somewhat offshore, which starts to appear after 50 yr. This extension has even a larger change in depth than the downdrift ebb-tidal delta. As a result of both the updrift shift of the downdrift delta and the downdrift extension of the updrift delta, the deltas eventually merge. This is revealed in fig. 3.4, where the change in bed level (with respect to the initial bed level) is shown after 368 yr.

It it evident that the system behaves asymmetrically, with the channel-shoal system in the updrift sub-basin being more pronounced than that in the downdrift sub-basin. Also, the ebb-tidal delta near the updrift inlet is larger than that near the downdrift inlet and a larger part

of the banks surrounding the updrift inlet is eroded (compared to the downdrift inlet). Besides this asymmetry, figs. 3.2 and 3.3 reveal that the channel networks of both sub-basins do not merge, suggesting the formation of a tidal watershed in the basin.

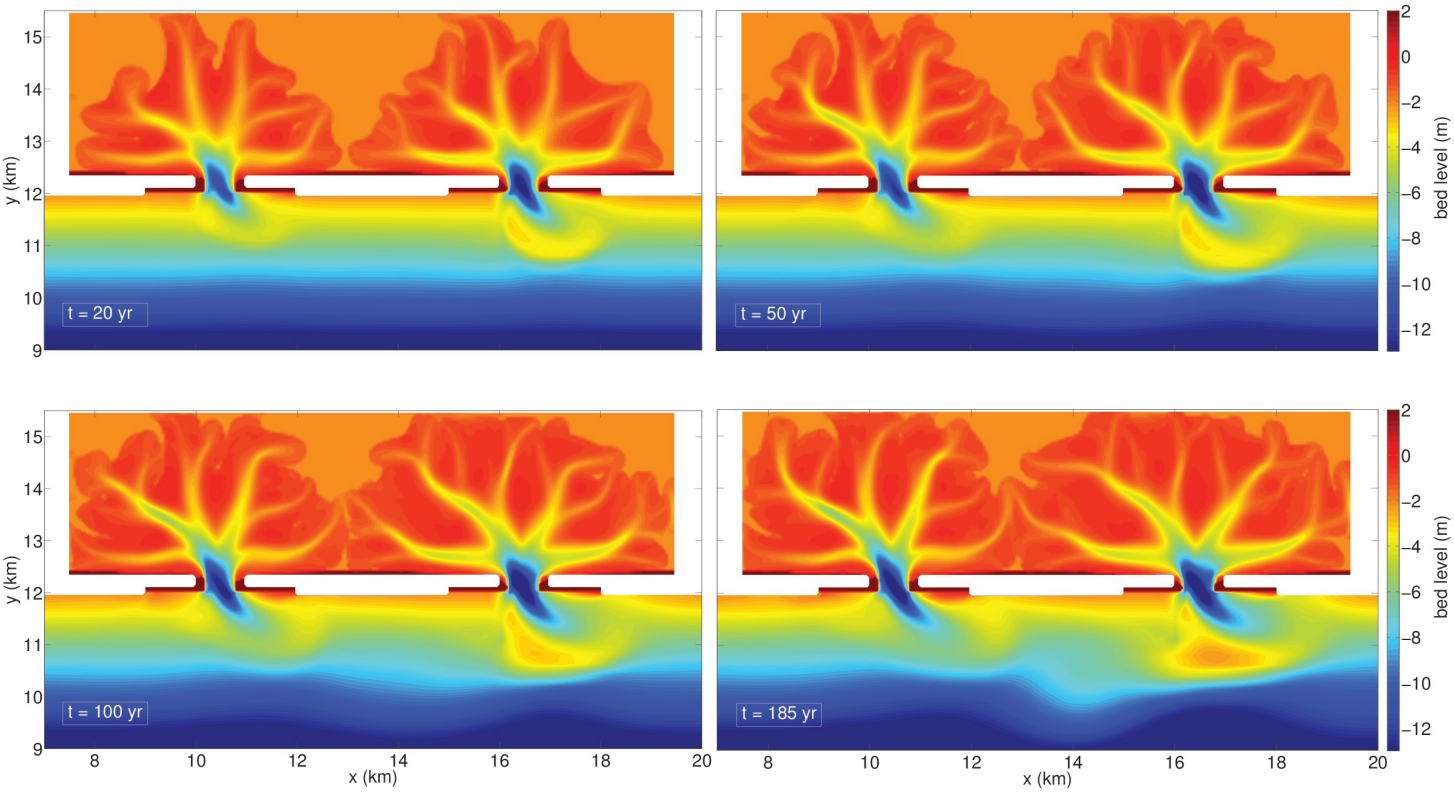

Figure 3.2: Colour plots of the bed level (in meters) in the domain at different times, with 0 representing mean water level.

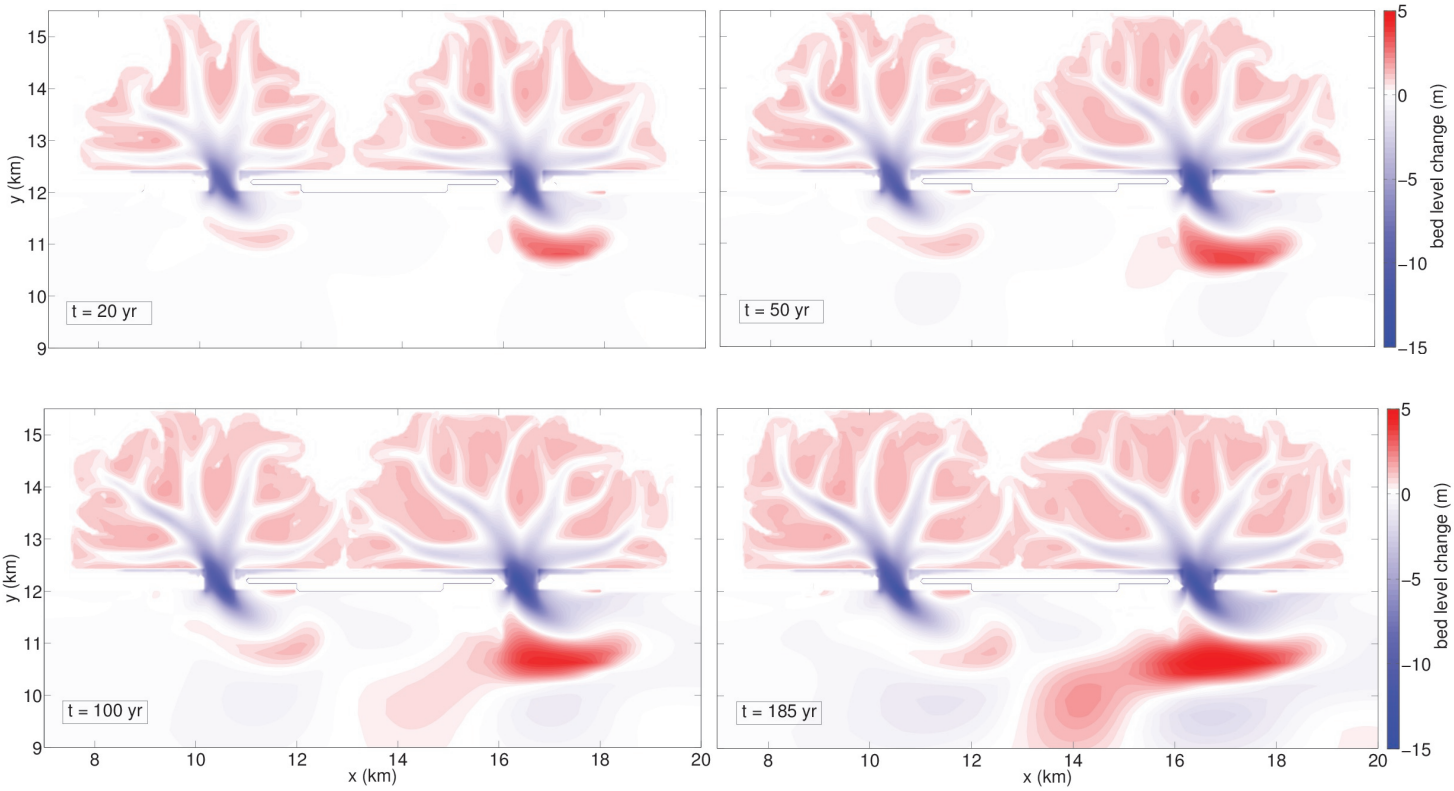

Figure 3.3: Colour plots of the change in bed level (in meters) in the domain at different times, with red representing levels higher and blue lower than the initial bed level of 2 m below mean sea level.

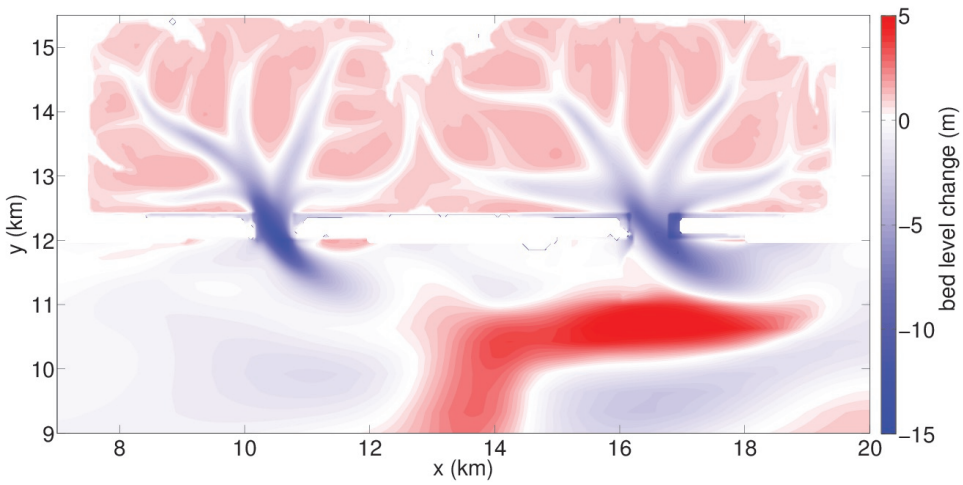

Figure 3.4: Colour plot of the change in bed level in the reference domain after 368 yr, with red representing levels higher and blue lower than the initial bed level of 2 m below mean sea level.

3.1.3 Hydrodynamics

In order to understand the morphodynamic patterns and asymmetries as described in the previous section, also the hydrodynamic evolution of the system is examined. In order to do so, a harmonic decomposition of both longshore and cross-shore currents u and v, and of the sea level elevation η is carried out. It turns out that besides the M2 tidal component, which is used to force the system with, also tidal residual flow and M4 (first overtide of M2) are important. The latter is generated by nonlinear terms in the equations of motion and the interaction of the M2 tidal wave with the complex bottom topography.

Residual flow

Fig. 3.5 shows patterns of the residual current at two different times, viz. at the initial state and after 185 yr. It is clear that initially (uniform depth in basin and inlets, left panel of fig. 3.5) the two sub-systems hardly interact in terms of residual flow and behave remarkably similar. Of course this is also triggered by the symmetric positioning of the two inlets, being 1/4 basinwidth removed from either side of the basin. The general pattern of the residual is a residual circulation cell: a net cross-shore flow just landward of the inlet, directed towards the back of the basin, which turns to both sides and returns to the inlet almost parallel to the coast. In the nearshore sea an almost shore-parallel residual flow towards the inlet is recognisable in the left panel of fig. 3.5, by far most dominant at the updrift side of each inlet. Besides this longshore flow, an almost cross-shore residual flow away from the inlet exists.

After 185 yr (right panel of fig. 3.5), the morphological patterns described in the previous section have formed, which comes with a totally different residual flow pattern. There is a net flow from the updrift sub-basin to the downdrift sub-basin. Furthermore, the updrift residual circulation cell of the updrift basin is still partly recognisable. However, the dominant pattern is a residual flow from the updrift inlet towards the downdrift inlet. In the nearshore sea, a large residual flow over the updrift ebb-tidal delta is present.

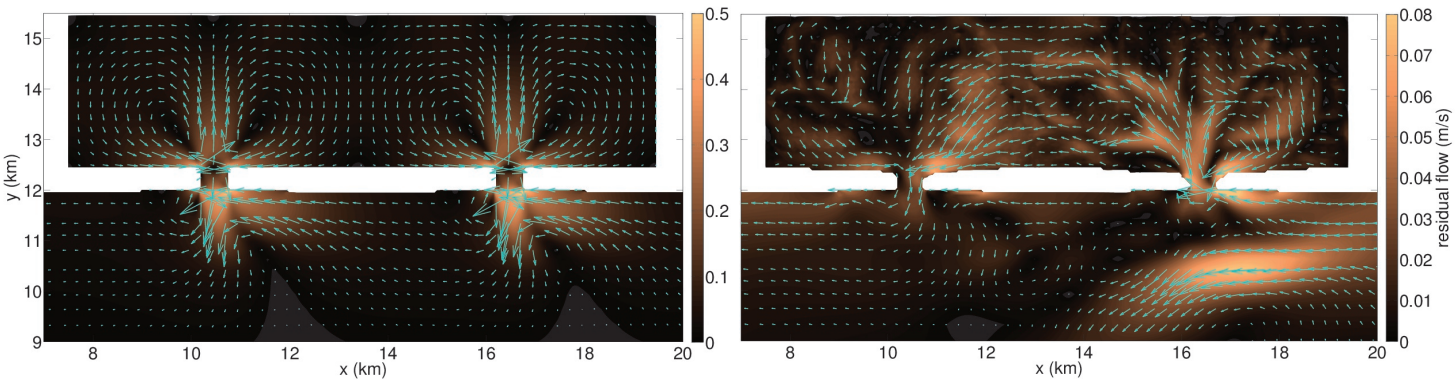

Figure 3.5: Vector field of the residual flow in the domain at the initial state (left) and after 185 yr (right). The magnitude of the flow (in m/s) is also highlighted by the colours.

In fig. 3.6 the residual flow, averaged over the basin width, is shown at the separation between the sub-basins (as defined in § 3.1.1) at the initial state and after 20 yr, 50 yr, 100 yr and 185 yr. The residual flow from updrift to downdrift sub-basin (negative values) is clearly increasing in time.

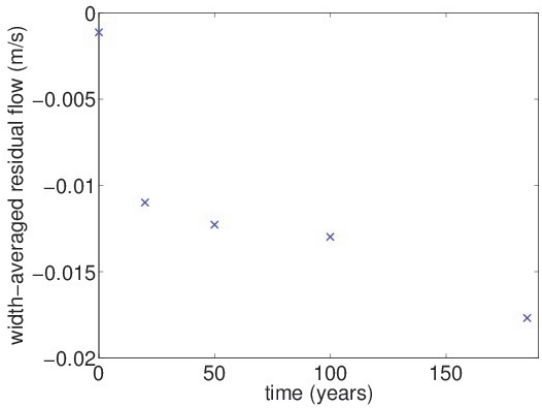

Figure 3.6: Residual flow averaged over the basin width, at the separation between the sub-basins, versus time. Five different times are shown, viz. the initial state, $t = 20\,\mathrm{yr}$, $t = 50\,\mathrm{yr}$, $t = 100\,\mathrm{yr}$ and $t = 185\,\mathrm{yr}$.

Harmonic components

For the M2 tidal components, the amplitude and phase of sea level elevation η are shown in fig. 3.7, together with the characteristics of the tidal ellipse describing the velocity, both at the initial state (left column) and after 185 yr (right column). From the M2 component of η (upper row), it becomes clear that the tidal wave initially moves slowly in the inlet (progressive wave, contour lines close together), and that there is standing wave behaviour in the basin, which is expected for short basins. However, after 185 yr, there is a clearly propagating wave in the basin, which propagates slower in the updrift sub-basin than in the downdrift sub-basin. Still, there is an almost constant sea level amplitude of 1.1 m in the basin, which is somewhat higher than the forced 1 m amplitude. To further investigate the standing and propagating wave behaviour in both inlets, fig. 3.9 shows the difference $\theta - \phi$ between the phases of the tidal ellipse and of the sea level elevation. The M2 tidal component is shown in blue, with the left (right) panel indicating the downdrift (updrift) inlet. Directly from the initial state, $\theta_{\mathrm{M2}} - \phi_{\mathrm{M2}}$ drops in both inlets to approximately $\pi/2$, indicating the transition from dominant propagating to dominant standing wave behaviour.

Regarding the tidal ellipse (see § 2.2.1), it is shown in fig. 3.7 that the maximum velocity magnitude is initially much larger in the inlet than in the basin and the sea. Furthermore, the phase of the ellipse in the sea decreases towards the coast, which implies that the maximum current in the sea occurs earlier close to the coast than farther away. In the basin, the phase increases landward of the inlets in the cross-shore direction and decreases in the longshore direction to the left and right of both inlets. From the initial inclination (bottom left panel of fig. 3.7), a similar pattern as for the residual velocity in the left panel of fig. 3.5 can be recognised, i.e., the previously described residual cell. The M2 tidal wave enters the basin in the cross-shore direction (inclination $\sim \pi/2$) and turns sideways (inclination ~ 0), seaward and back to the inlet. The eccentricity shows that at the stagnation points (where the phase of the ellipse is not defined), the ellipses are circular. At those location, the velocity has (almost) vanished.

After 185 yr the largest M2 currents are found in the offshore sea, over the ebb-tidal deltas and in the updrift inlet. Furthermore, in the channels the M2 current magnitude mostly decreases with increasing distance from the inlets, but values in the updrift sub-basin are signifi-

cantly larger than in the downdrift sub-basin. Over the shoals velocities are very low. From the eccentricity it is concluded that in the channels the velocity is mostly unidirectional, and from the inclination it is seen that currents are in the along-channel direction, as expected. At the downdrift side of each inlet, there is an area of large eccentricity. An important difference with $t = 0\,\mathrm{yr}$ is the orientation of the main channel in the inlet, which has shifted from cross-shore to a slanted orientation with a significant longshore component.

The second most important tidal constituent is M4, which is visualised in fig. 3.8 by the amplitude and phase of sea level elevation η (upper row), and the characteristics of the tidal ellipse describing the velocity (middle and bottom row), both at at the initial state (left column) and after 185 yr (right column). In the upper panels of fig. 3.8, it is shown that the M4 contribution of sea level elevation to the total signals is negligible in the sea (cf. upper panels of fig. 3.7). In the basin, there is initially again a uniform amplitude of η, although a slightly larger amplitude can be seen in the downdrift part. Furthermore, the amplitude increases in the inlets towards the basin. After 185 yr, the amplitude of M4 sea level elevation in the channels is comparable to that in sea, but increases towards the quasi-undisturbed bottom at the edges of the basin. Overall it can be stated that the generated M4 component has a larger amplitude in the downdrift sub-basin (compared to the updrift sub-basin). In the updrift sub-basin, there is quite a strong phase propagation towards the inlet. For the downdrift basin, a small phase propagation towards the inlet is observed (although not visible in fig. 3.8) of several tenths of radians, indicating that the M4 tidal component is generated in the basin. The right panel of fig. 3.9 shows the difference between the phase of tidal ellipse (θ) and sea level elevation (ϕ) of the M4 tidal component (in red). The same as for the M2 tidal component, the M4 component shows a transition from dominant progressive wave behaviour ($\theta - \phi \sim 0$) to dominant standing wave behaviour ($\theta - \phi \sim \pi/2$). However, the transition takes longer and is not as clear as for the M2 component.

Regarding the M4 tidal ellipse (middle and bottom row of fig. 3.8), initially there is a strong M4 component in the proximity of the inlet (which is the same area as for the initial M2 ellipse, cf. 3.7), but with a semi-major axis that is smaller than the semi-major axis of the M2 ellipse. Also, the phase propagation of the M4 tidal ellipse in the basin shows similar behaviour as that of the M2 tidal ellipse. Furthermore, the eccentricity and inclination in the basin show similar behaviour as for the M2 case. After 185 yr, only in the parts of the channels located away from the inlets, a significant M4 velocity magnitude is observed. However, in (the proximity of) the inlets and in the sea it is negligible compared to the M2 semi-major axis. From the eccentricity and inclination it can again be concluded that the currents are mainly unidirectional and in the direction of the channel, except for the updrift sub-basin in the proximity of the inlet. Here large values of the M4 eccentricity are observed, indicating cross-shore and longshore M4 velocities of equally large magnitude.

Regarding sea level elevation, η, amplitudes of M6 and M8 are in the whole domain smaller than 0.05 m and negligible compared to the total signal of the sea level elevation (not shown here). However, this is not the case for the M6 and M8 components of the total velocity signal. In order to quantify the importance of M6 and M8 components to the total velocity signal, the semi-major axis of the M6 and M8 tidal ellipses (indicating maximum velocity magnitude in a tidal period) is visualised in fig. 3.10 at the initial state (left) after 185 yr (right). It can be concluded that M6 and M8 are initially only important in the inlet, which is most probably due to large bottom friction. Fig. 3.11 shows the maximum during a tidal cycle of the ratio $|\boldsymbol{\tau}_\mathrm{b}|/\tau_\mathrm{cr}$ at different times in the morphological evolution, where it is evident (from the upper panel)

that the bottom shear stress magnitude $|\boldsymbol{\tau}_\mathrm{b}|$ is much larger than the critical shear stress τ_cr at the initial state in the domain, supporting the previous statement about large bottom friction.

Especially in the initial years, there is a strong erosion of the banks surrounding the inlet, causing a smoother flow and lower bottom shear stress (middle and bottom row of fig. 3.11), and therefore a decrease of the semi-major axes of the tidal ellipses of the the higher harmonics. At later stages in the evolution of the channel network, M6 and M8 are only of importance at the end of the channels, with M6 having the largest magnitude, which is shown in the right panels of fig. 3.10.

Net sediment transport patterns

Fig. 3.12 shows magnitude and direction of the net sediment transport per unit length at different times during the morphological evolution. As is shown, there is a large net sediment transport (per unit length) over the updrift ebb-tidal delta, which gives rise to the observed offshore and downdrift extension of this delta. Also, the intensity of the net transport decreases in time, with maximum values reaching from $1.4 \times 10^{-6}\,\mathrm{m^2/s}$ after 50 yr to $1.0 \times 10^{-6}\,\mathrm{m^2/s}$ after 185 yr, leading to a slow down of the morphological evolution of the delta.

In the initial case (upper panel in fig. 3.12) net sediment transport is located in the proximity of the inlets, and directed mainly out of the inlets (both landwards and seawards). However, once the morphological evolution has started, the main sediment transport is not only in the inlets and over the ebb-tidal delta, but also in the developed channels in the basin (fig. 3.12, middle and bottom row; cf. fig. 3.3). Over the shoals there is hardly any sediment transport. This difference between channels and shoals is mainly caused by the bottom shear stress, which is larger than the critical shear stress in the channels and lower or approximately equal to the critical shear stress over the shoals (cf. fig. 3.11). In the initial years of morphological evolution, there is a large net sediment transport in the longshore direction towards the centre of the basin (mainly at the seaward side of the updrift sub-basin, but to a lesser extend also in the downdrift sub-basin), that has almost completely disappeared after 185 yr.

This pattern of large net sediment transport in the channels and small transport over the shoals is confirmed by fig. 3.13, which shows the divergence of the net sediment transport in the domain. In areas with large divergence much sediment is eroded, whereas in areas with large convergence (negative values of divergence) sediment deposition takes place. This indicates that in the downdrift sub-basin two main channels are formed. In orientation, one channel is rotated approximately 45°clockwise with respect to the net transport in the sea. The second one is rotated approximately 115°clockwise with respect tot the net transport in the sea. According to fig. 3.12, the former channel has the largest net sediment transport per length, which remains during the whole evolution. In the updrift sub-basin the pattern of the divergence is less clear, although convergence over the shoals and divergence in the channels is also here the main pattern. As was the case for the downdrift sub-basin, also in the updrift sub-basin two main channels develop. This is especially clear after 185 yr (bottom right panel in fig. 3.13), from which it is concluded that the orientation of these two channels is the same as mentioned already for the downdrift sub-basin. It turns out that the downdrift inlet keeps eroding during the whole morphological evolution (divergence of net sediment transport), whereas the updrift inlet changes from completely eroding towards a state of slight deposition of sediment on the downdrift side (convergence of net sediment transport). Finally, note that there is almost no

evolution of the developed channel any more after 185 yr (see fig. 3.13). This could point at the formation of a tidal watershed, although one cannot speak of an effective separation of two sub-systems, because there still is a residual flow (cf. fig. 3.5).

For further inspection of the net sediment transport patterns, the net sediment transport (per unit length) in the basin is averaged over the basin width, which is visualised in fig. 3.14. In this figure, four different times during the simulation are considered, viz. 20 yr, 50 yr, 100 yr and 185 yr. In this figure, it is shown that the net mean transport is directed from the inlets towards the sides of the basin and from the inlets towards the centre of the basin. Therefore a location of zero net transport occurs in the middle of the basin. In the course of time, this location of zero net transport shifts towards the downdrift side, as was also the case for the minimum in the maximum absolute width-averaged longshore velocity ($|U|_{\max}$, cf. fig. 3.1). Based on this observation, it can be concluded that for all times, there is negligible exchange of sediment between the sub-basins. Note that the net mean sediment transport is larger at the downdrift side of both sub-basins, indicating that the dominant transport direction in the basin is downdrift. This is also in accordance with fig. 3.12 (especially the panels after 20 yr and 50 yr), where net sediment per length in the basin on the downdrift side of the inlets is larger than on the updrift side of the inlets.

Note that the net sediment transport in the inlets is directed into the basin, indicating flood dominance. For the downdrift inlet this is the case for the whole width of the inlet. For the updrift inlet there is a small channel at the updrift side of the inlet which is ebb-dominant and consequently exporting sediment. This is the case during the whole evolution. To examine this general sediment import behaviour more extensively, the results of fig. 3.12 are recalculated, but instead of using the extended transport formulation discussed in eq. (2.6)–(2.14) a simple formulation is used, viz. eq. (2.29). The net sediment transport resulting from this simple transport formulation is shown in fig. 3.15. The overall characteristics are the same as already shown from the extended transport formulation in fig. 3.12. However, fig. 3.15 shows larger sediment transport over the shoals, which is mainly due to the absence of a critical shear stress in the simple formulation.

The net sediment transport is parameterised by eq. (2.31) and split into a part due to joint action of residual flow and M2 tidal velocities and a part due to tidal asymmetry, which are both shown in fig. 3.16 at the initial state and after 50 yr and 185 yr. Initially the part of the transport due to the residual flow (upper left panel of fig. 3.16) is directed seawards in the inlets, with a slightly larger magnitude in the updrift inlet. In the basin, close to the inlet, a landward transport occurs, which is much weaker than the seaward transport. For the part induced by tidal asymmetry (upper right panel of fig. 3.16), the transport in the inlet is directed towards the basin. Based on the direction of transport, the total sediment transport at the initial state (upper panel in fig. 3.15) in the proximity of the inlet is at the landward side dominated by tidal asymmetry and at the seaward side dominated by the residual flow.

After 50 yr (middle row of fig. 3.16), the sediment transport in the downdrift sub-basin is largely due to tidal asymmetry, whereas the dominant transport in the updrift sub-basin is induced by the residual flow. As was already concluded from fig. 3.12, the net sediment transport in both inlets is directed into the basin (flood dominace), which is also in agreement with the direction of the just mentioned dominant transports. However, this is not evident and will be discussed later on. Besides both inlets having a net importing effect of sediment, they still experience a seaward component: in the downdrift inlet the part induced by the

residual flow is directed seaward, and in the updrift inlet the part induced by tidal asymmetry is directed seaward. These components contribute to the formation of the ebb-tidal deltas. Yet, the seaward transport in the updrift basin is larger than that in the downdrift basin. As a result, the updrift ebb-tidal delta is larger than the downdrift one (cf. fig. 3.3). Over the seaward extension of the updrift ebb-tidal delta, which was noticed before (cf. fig. 3.3), a large transport is seen only due to the residual flow (left column in fig. 3.16). After 185 yr (bottom row of fig. 3.16), the net sediment transport patterns are almost the same as those at $t = 50$ yr, except for the decreased transport magnitudes in the basin.

To study the main cause of net sediment import of the system (largely due to the residual flow in the updrift subsystem and due to tidal asymmetry in the downdrift subsystem, as discussed earlier), the terms in eq. (2.31) are studied next (in the inlets). Fig. 3.17 shows the temporal evolution of $\cos(2\theta_{\mathrm{M2}} - \theta_{\mathrm{M4}})$ (phase difference of tidal ellipse, red) and $\cos(2\phi_{\mathrm{M2}} - \phi_{\mathrm{M4}})$ (phase difference of sea level, blue), both for the centre of the downdrift inlet (left panel) and the centre of the updrift inlet (right panel). The phase of the sea level is only included to compare its behaviour to the phase of the tidal ellipse, but does not play a role in eq. (2.31). For the downdrift inlet, the phase difference of the tidal ellipse is quite constant in time, whereas the cosine of the phase difference of the sea level decreases. For the updrift inlet, exactly the opposite is observed. Because only $\cos(2\theta_{\mathrm{M2}} - \theta_{\mathrm{M4}})$ plays a role in the simple transport formulation of eq. (2.31), it is concluded that the phase difference between the M2 and M4 tidal components only decreases sediment transport in the updrift inlet. Because the cosine is in both inlets positive, in both inlets a sediment import is observed.

Fig. 3.18 shows the temporal evolution of the residual velocity (green) and of the semi-major axis of M2 (blue) and M4 (red) tidal ellipses, all relative to the values at $t = 185$ yr. For the centre of the updrift inlet (right panel) the M2 component hardly changes over time (except for a large decrease in the first few years and a gentle increase during the rest of the evolution). However, residual flow increases in time, which has an increasing effect on the net sediment transport. This effect is counteracted by a decreasing M4 semi-major axis. For the centre of the downdrift inlet (left panel in fig. 3.18) M2 and M4 are the main contributors to a decreasing sediment transport, whereas the effect of the residual flow is negligible.

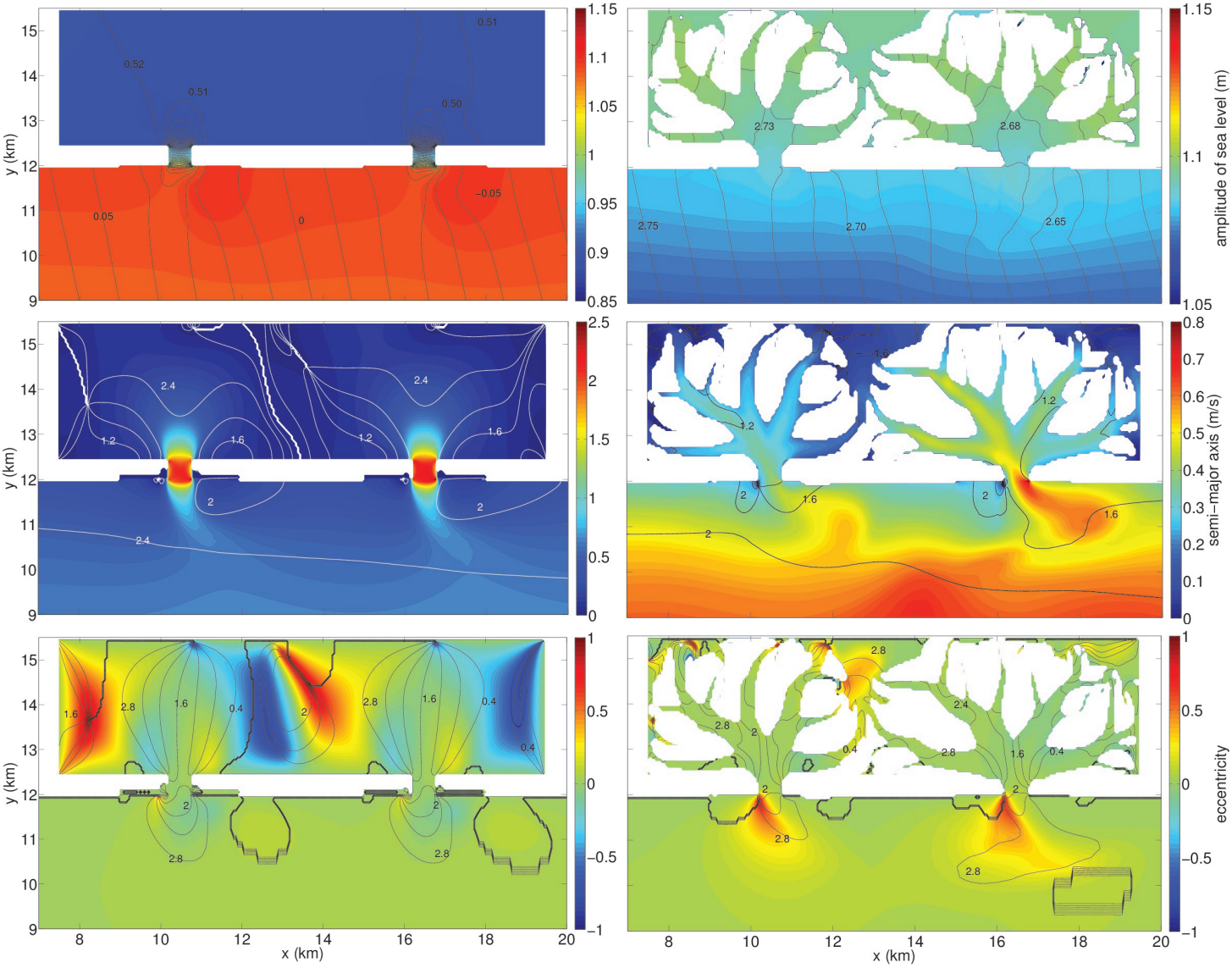

Figure 3.7: M2 components of vertical and horizontal tides at the initial state (left) and after 185 yr (right). Upper row: amplitude (colours, in meters) and phase (lines, in radians) of M2 sea level component. Middle row: semi-major axis (colours, in m/s) and phase (lines, in radians) of the M2 tidal ellipse. Bottom row: eccentricity (colours) and inclination (lines, in radians) of the M2 tidal ellipse.
Grid cells that are partly submerged during a tidal cycle are excluded.

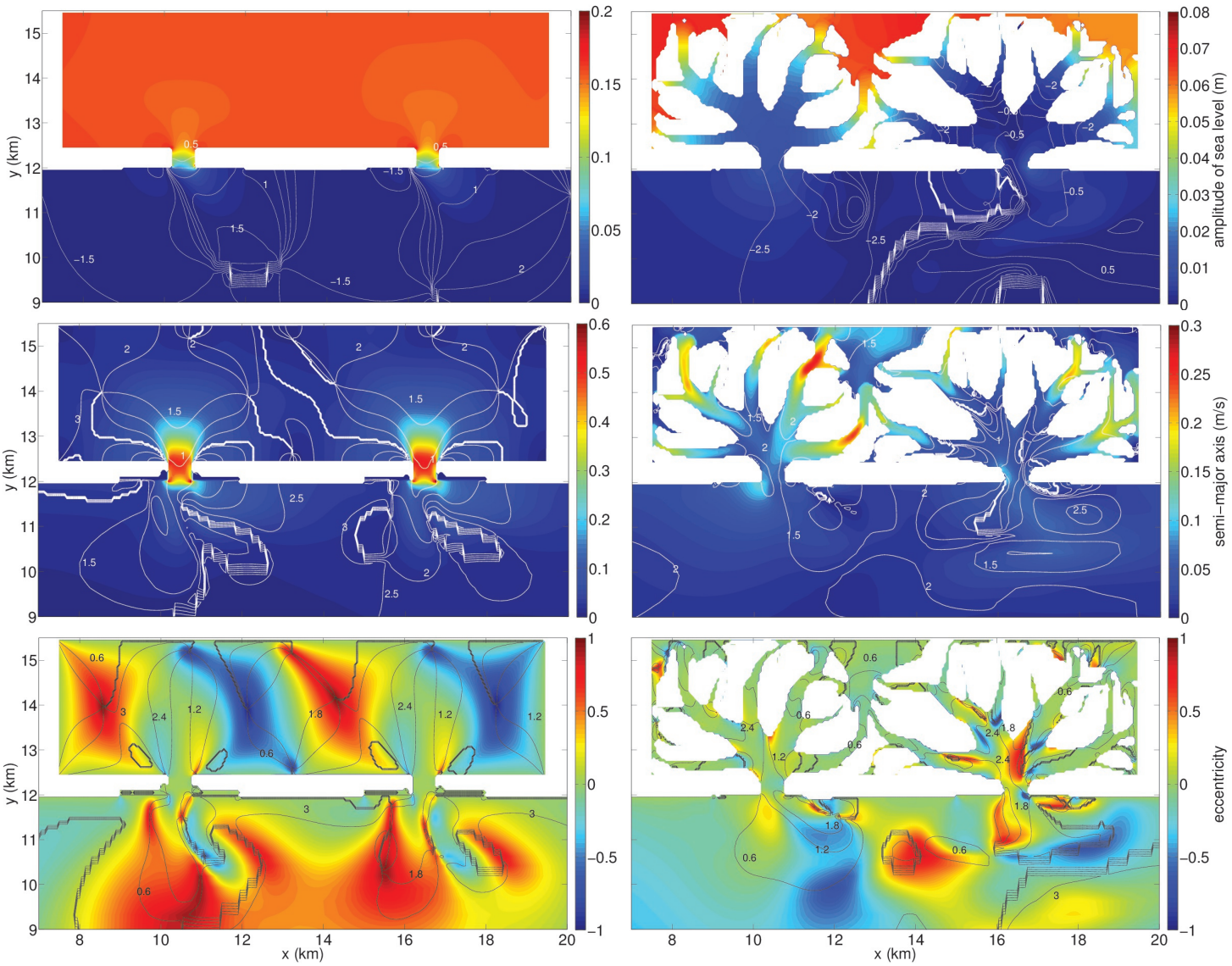

Figure 3.8: M4 components of vertical and horizontal tides at the initial state (left) and after 185 yr (right). Upper row: amplitude (colours, in meters) and phase (lines, in radians) of M4 sea level component. Middle row: semi-major axis (colours, in m/s) and phase (lines, in radians) of the M4 tidal ellipse. Bottom row: eccentricity (colours) and inclination (lines, in radians) of the M4 tidal ellipse.
Grid cells that are partly submerged during a tidal cycle are excluded.

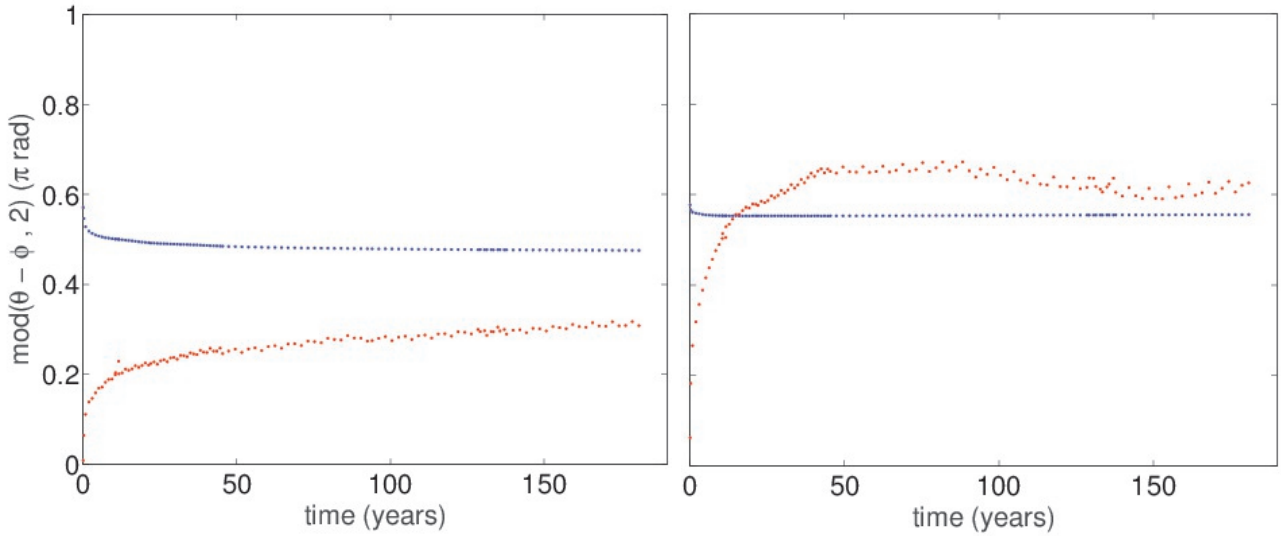

Figure 3.9: Phase difference between velocity (θ) and sea level (ϕ), in units of π radians. Shown are both M2 (blue) and M4 (red) components and downdrift (left) and updrift (right) inlets.

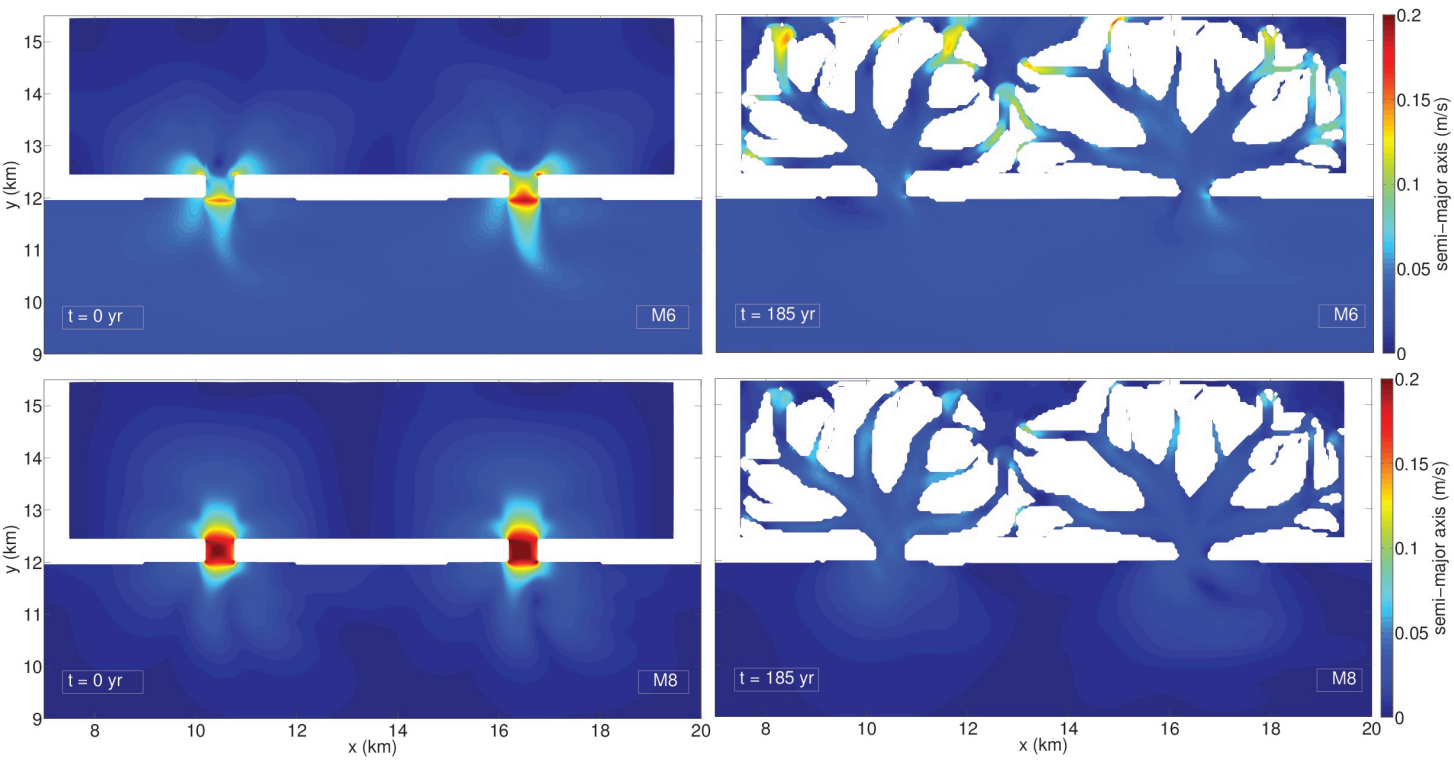

Figure 3.10: Colour plots of the semi-major axis of M6 (upper row) and M8 (lower row) tidal ellipses in the domain at the initial state (left) and after 185 yr (right). Units are m s^{-1} Grid cells that are partly submerged during a tidal cycle are excluded.

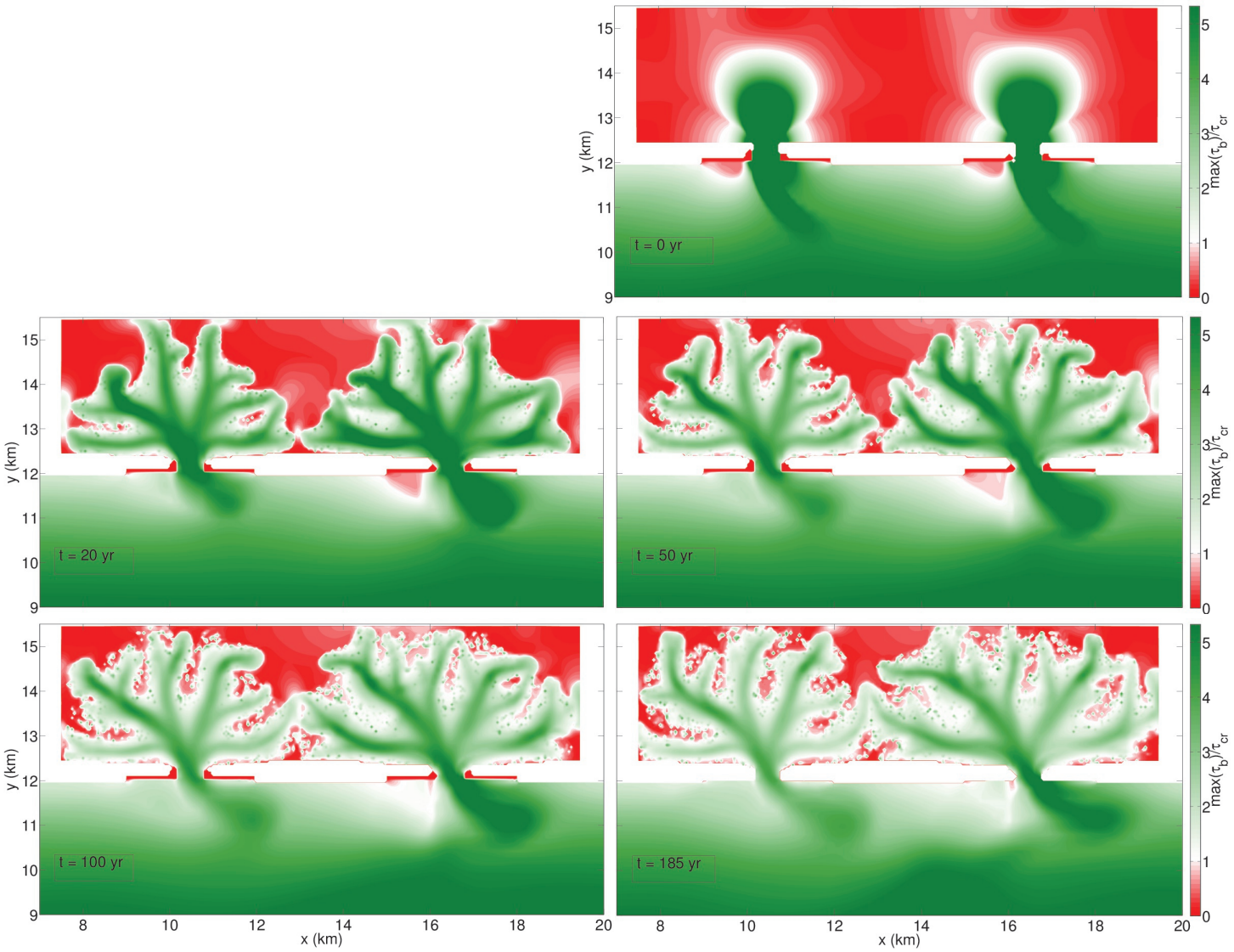

Figure 3.11: Ratio of bed shear stress magnitude ($|\boldsymbol{\tau}_\mathrm{b}|$, cf. eq. (2.2)) over critical shear stress (τ_crit, cf. eq. (2.13)) in the domain at different times. The maximum during a tidal cycle is considered.

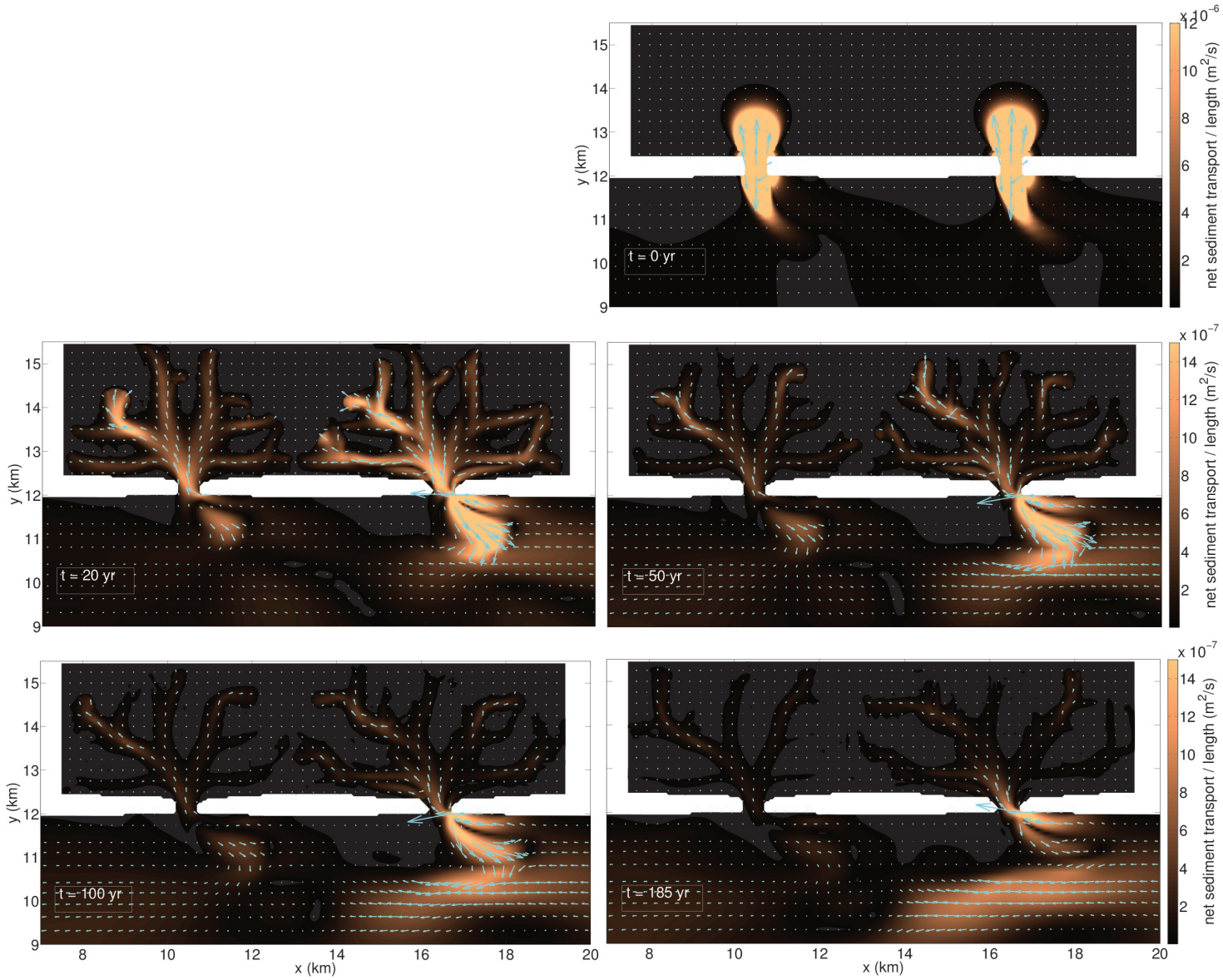

Figure 3.12: Vector field of the net sediment transport per unit length in the domain (in m^2/s) at different times. The magnitude of the transport is also highlighted by the colours.

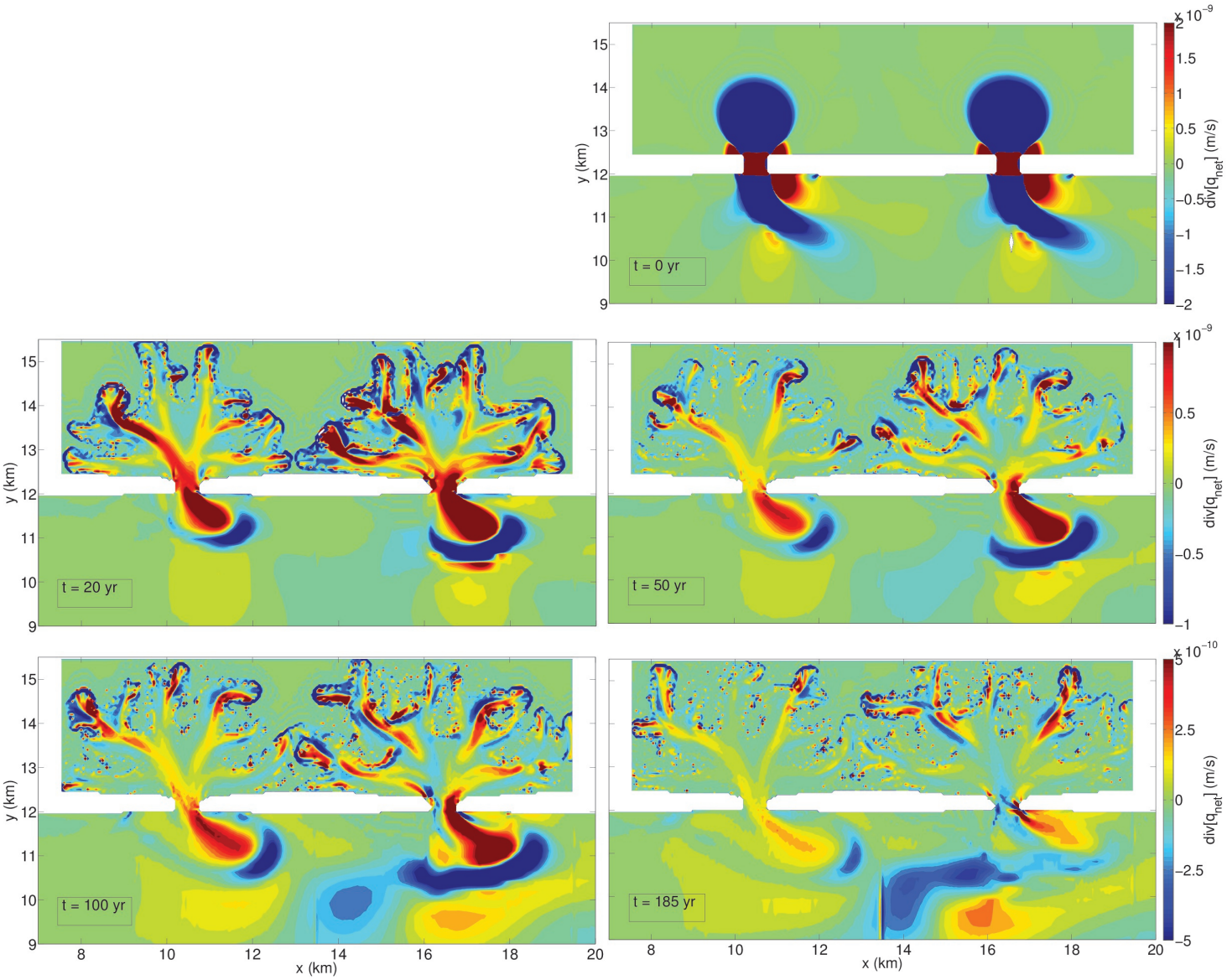

Figure 3.13: Divergence (in m/s) of the net sediment transport per unit length in the basin, at different times.

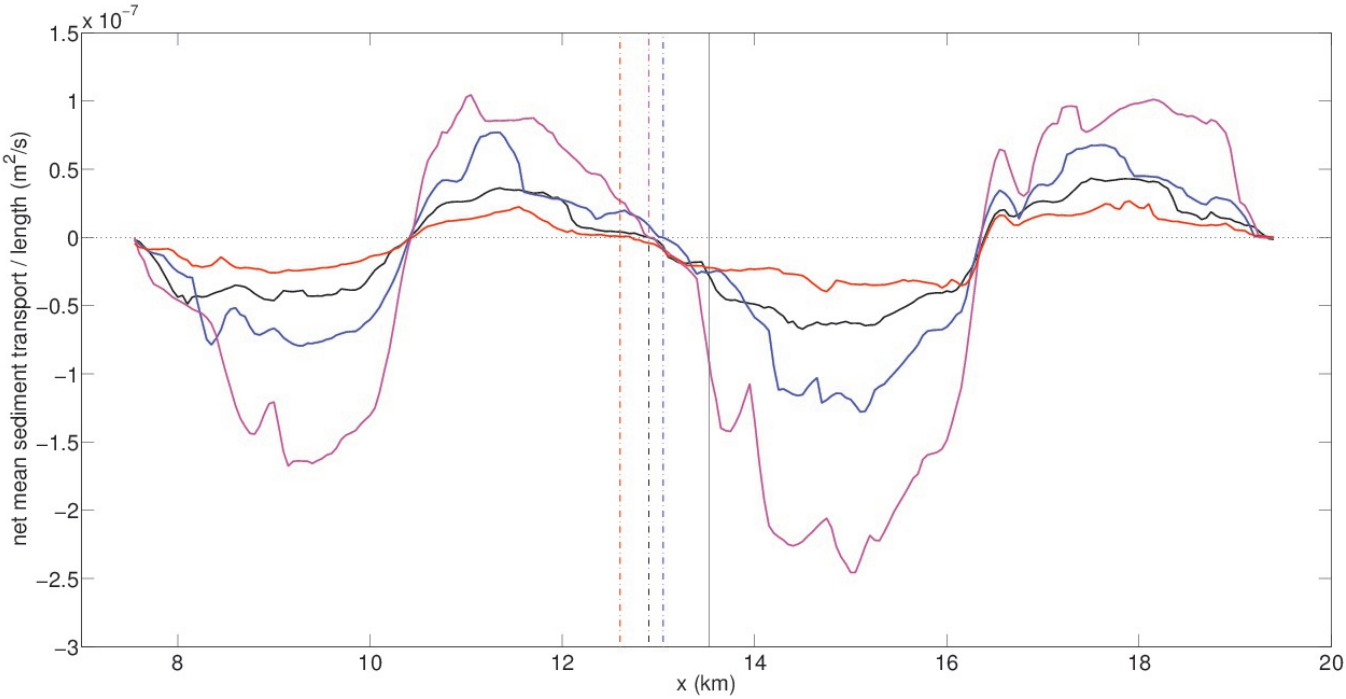

Figure 3.14: The net sediment transport (per unit length) averaged over the width of the basin (in m^2/s), versus longshore distance x, with positive (negative) values indicating transport in the updrift (downdrift) direction. Different times are indicated by the colours, where magenta indicates 20 yr, blue 50 yr, black 100 yr and red 185 yr. Note that the blue and red lines indicate the same moments in time as in fig. 3.1.
The minimum of the absolute value of the net mean sediment transport is determined in the middle part of the basin (between $x = 11$ and 15 km), with the x-values of the minima given by the dashed-dotted lines. Note that the x-values of the minimum at 20 and 100 yr coincide. The geometrical centre of the basin is given by the solid black line.

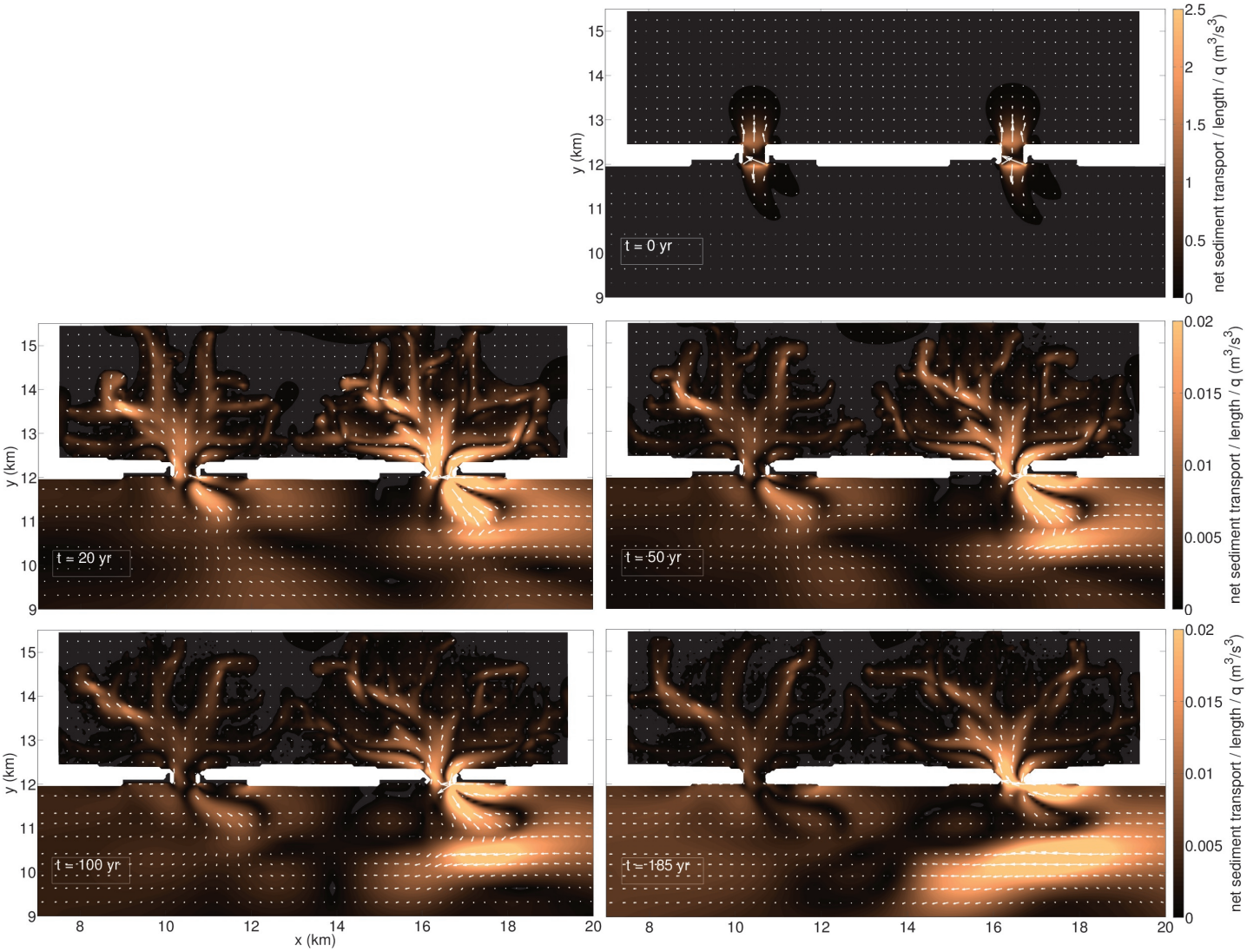

Figure 3.15: Vector field of the net sediment transport (divided by a constant $\hat{q}$, see § 2.2.4), as parameterised by eq. (2.31). The initial transport and four different times during the morphological evolution are shown. Magnitudes of the transport are also highlighted by the colours.

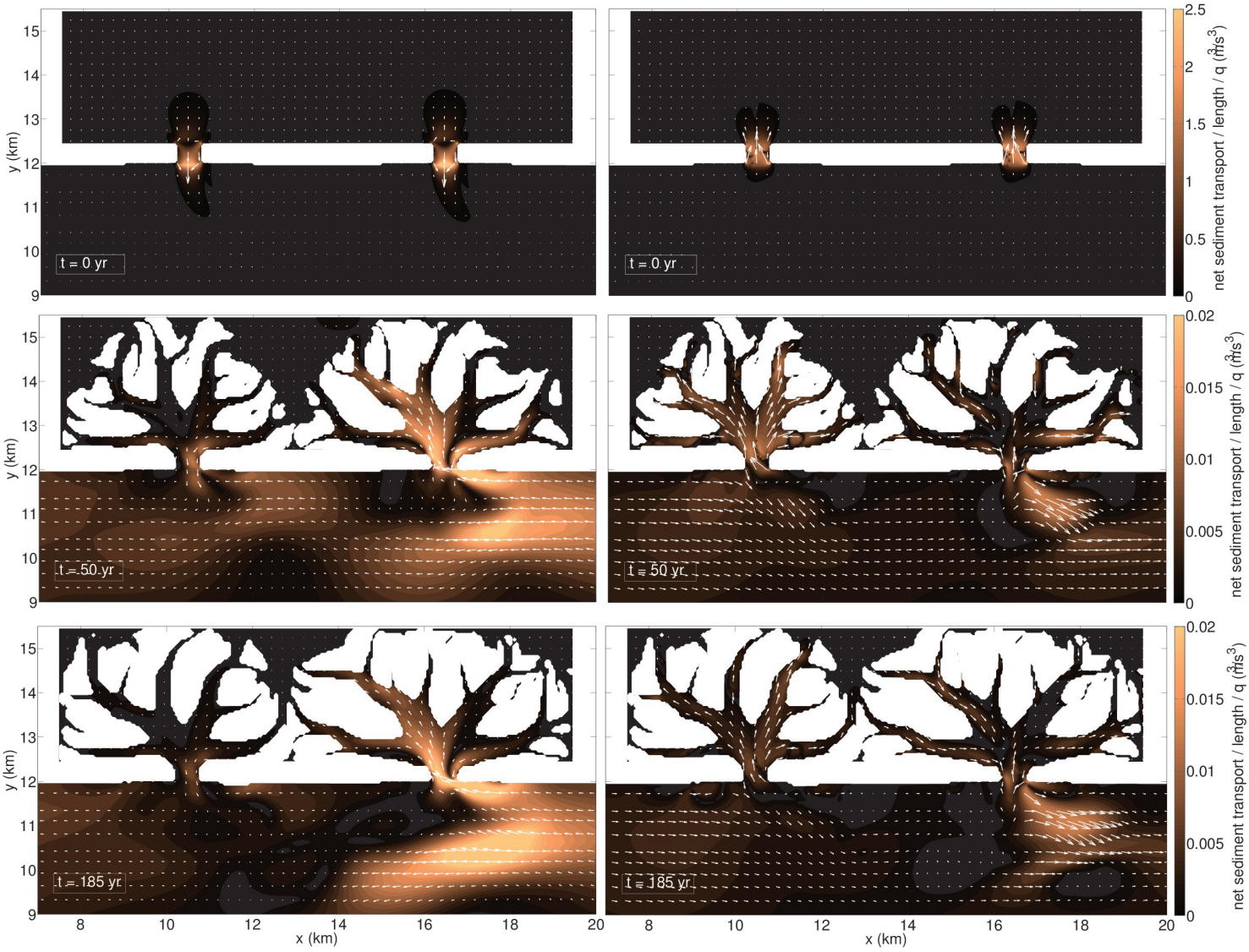

Figure 3.16: Vector field of the net sediment transport (divided by a constant $\hat{q}$, see § 2.2.4) due to joint action of residual and M2 tidal velocities (left column) and due to joint action of M2 and M4 tidal velocities (asymmetry, right column), as parameterised by eq. (2.31). Three different times are shown. Magnitudes of the transport are also highlighted by the colours.
Grid cells that are partly submerged during a tidal cycle are excluded.

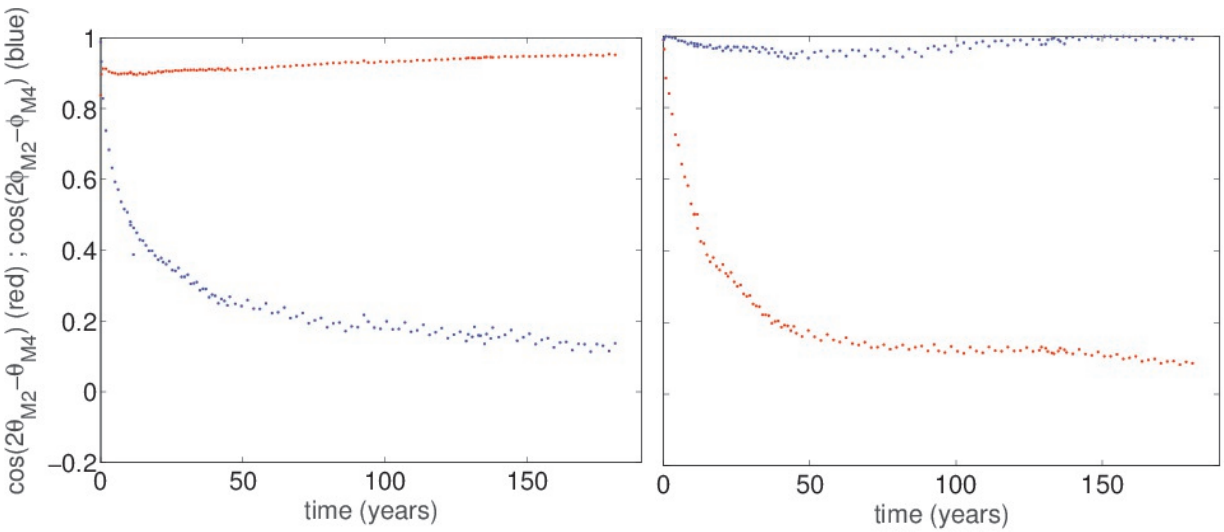

Figure 3.17: The cosine of the phase difference between the M2 and M4 tidal current ellipses ($\cos(2\theta_{\mathrm{M2}} - \theta_{\mathrm{M4}})$, red) and the cosine of the phase difference between M2 and M4 components of sea level elevation ($\cos(2\phi_{\mathrm{M2}} - \phi_{\mathrm{M4}})$, blue) in time. Left: in the centre of the downdrift inlet. Right: in the centre of the updrift inlet.

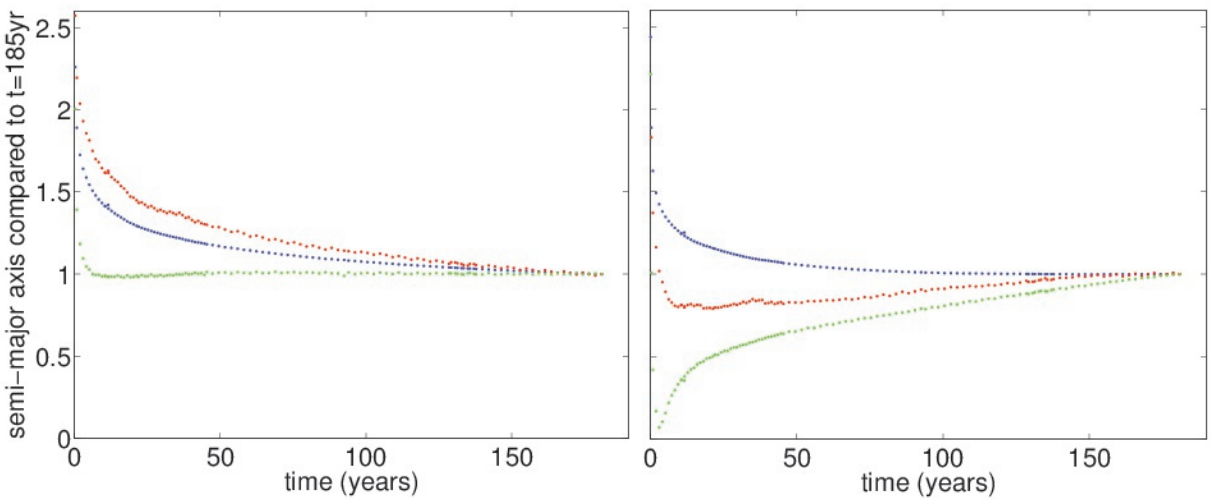

Figure 3.18: Residual velocity and semi-major axis of M2 and M4 tidal ellipses in time. Green indicates M0 (residual component), blue indicates M2 and red indicates M4. Left: in the centre of the downdrift inlet. Right: in the centre of the updrift inlet.

3.1.4 Evolution of morphometric parameters

To evaluate the temporal evolution of the system, several morphometric parameters are introduced in this section and their evolution in time is studied. The main question to answer with the gained knowledge is whether the system tends to evolve towards an equilibrium state.

The first parameter that will be evaluated, is the centre of mass of the channels in the basin, as introduced in § 2.2.2. The evolution of the centre of mass in time is drawn in the (x, y)-plane in the left panel of fig. 3.19, where the updrift (downdrift) sub-basin is indicated in red (blue). The origin of the coordinate system in this panel is the initial position of the centre of mass, being in the middle of the most landward side of the inlet. The centres of mass of both channel systems start to shift in the downdrift direction (with the most pronounced shift in the first 25 years), which is caused by the orientation of the main channel (cf. 3.13 at $t = 20\,\mathrm{yr}$). However, after 75 yr the centre of mass of the updrift basin reverses direction, and evolves back updrift. This behaviour is not directly clear from the evolution of the downdrift centre of mass. However, a slow down in spatial evolution of the centre of mass takes place from $t = 0\,\mathrm{yr}$ towards $t = 75\,\mathrm{yr}$ (indicated by a decreasing distance between the blue dots in the left panel of fig. 3.19), which accelerates again after this time. The main direction of morphologic evolution in the downdrift sub-basin is downdrift, and the main direction of morphologic evolution in the updrift sub-basin is initially downdrift, but after 75 yr updrift. This last behaviour is an indication for the development of a tidal watershed between the two sub-basins, which is a result of convergent sediment transports in the centre of the basin. When the channels of the updrift sub-basin meet the watershed, they simply cannot expand any more on the downdrift side, because sedimentation near the watershed takes place. Yet at the edge of the basin, the channels can still evolve. The continuous downdrift movement of the downdrift centre of mass is explained by the downdrift orientation of the main channel in the inlet and the downdrift sub-basin. However, between 50 yr and 75 yr, the centre of mass stabilises (see left panel of fig. 3.19), after which the downdrift trend starts again. This has to do with a similar mechanism as discussed for the updrift sub-basin. Namely, the main orientation of the channels is downdrift, inducing a downdrift motion of the centre of mass. After some time the downdrift edge of the basin is reached and downdrift motion slows down. Finally, after 75 yr, the channels also reach the watershed at the updrift side of the downdrift sub-basin, reducing the updrift trend. From that moment on, the downdrift directed motion of the centre of mass of the channels is continued.

To have a measure for the spreading of the channels, a spatial variance is used, as defined in eq. (2.26). The evolution of this variance in time is drawn in the (x, y)-plane in the right panel of fig. 3.19, where the updrift (downdrift) sub-basin is indicated in red (blue). The origin of the coordinate system in this panel is the initial variance of the channels in the basin, which is by definition zero. To assess whether the channel system develops spatially uniform or not, four additional lines are added. The solid black line ($\mathrm{var}[x] = \mathrm{var}[y]$) indicates equal expansion in both directions. The dashed black line ($\mathrm{var}[x] = 4\mathrm{var}[y]$) is a correction on the solid line when the dimensions of half the basin (6 by 3 km) are taken into account. Finally the dotted lines are a correction when the specific dimensions of downdrift sub-basin (blue) and updrift sub-basin (red) are taken into account.

For the entire evolution, both sub-systems evolve predominantly in the x-direction (red and blue curve below solid black line). However, already in the initial evolution it is clear that the downdrift system evolves relatively more in the y-direction than the updrift system, which

it continues to do, even compared to the dimensions of the downdrift sub-basin (blue curve above dotted blue line). However, where the downdrift system has in the course of time an ever increasing y-dominance, this is not the case for the updrift system, which varies quite strongly in time, but has overall a quite uniform distribution of channels in both directions (relative to the dimensions of the sub-basin). This is seen in the right panel of fig. 3.19 by the red curve staying from $t = 25$ yr onwards between the dashed line and the red dotted line.

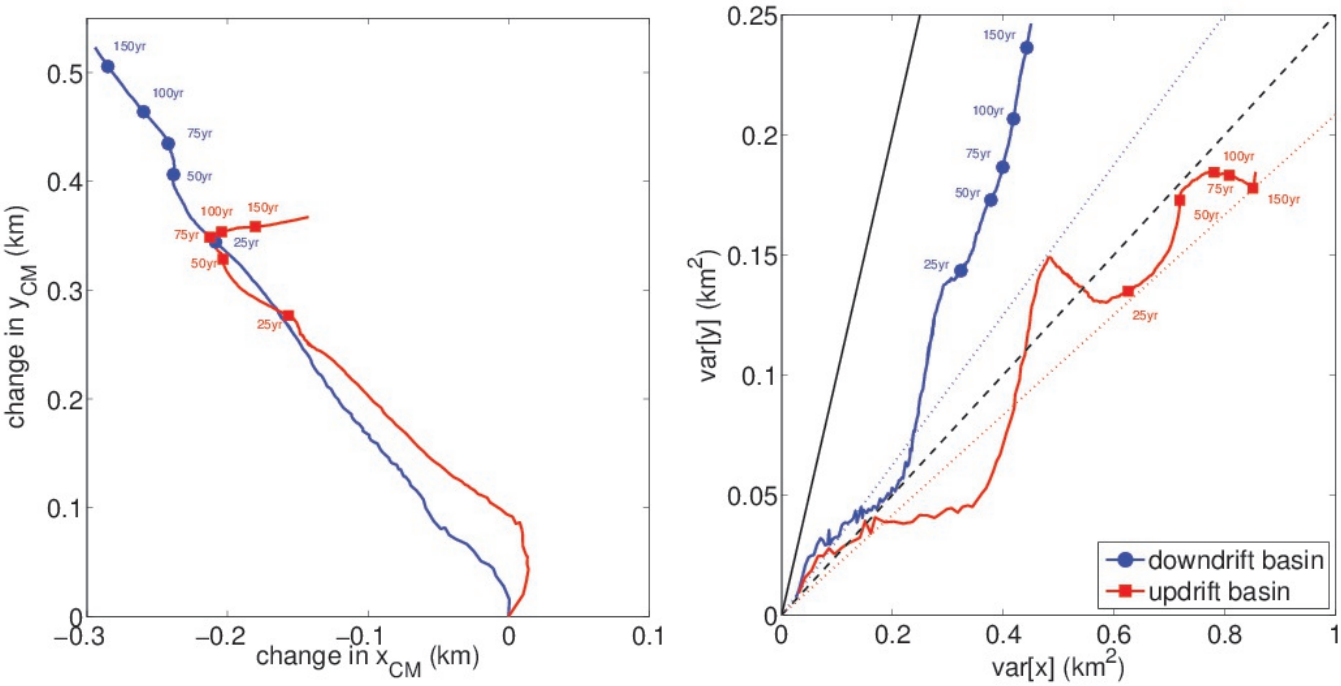

Figure 3.19: Left panel: evolution of the position of the centres of mass ($\mathbf{x}_{\mathrm{CM}}$) of the channels in the updrift (red) and in the downdrift (blue) sub-basin.
Right panel: evolution of x-variance (var[x]) and y-variance (var[y]) of the centres of mass in both sub-basins.
In both panels, the symbols indicate t = 25, 50, 75, 100 and 150 yr. The solid line indicates uniform spatial variation in x- and y-direction. The dashed line indicates var[x] = 4var[y] (equal spatial variation in both directions relative to the dimensions of a 6 by 3 km basin). The upper (blue) and lower (red) dotted lines indicate equal spatial variation in both directions relative to the dimensions of the downdrift and updrift sub-basin respectively.

From the path of the centre of mass, it is not evident whether the system moves towards an equilibrium or not, although changes in the last decades are much less than earlier in the evolution. However, fig. 3.12 already revealed that the net sediment transport per unit length decreases in time, both in the inlet and in the channels. Therefore a new morphometric parameter is introduced to investigate the temporal evolution towards a possible equilibrium state, namely the total deposited sediment volume (in m^3). This volume is determined by integrating the change in bed level over the domain. This total deposited sediment volume is shown in fig. 3.20, where the downdrift (updrift) inlet is indicated by blue (red) curves. The solid curves indicate the sub-basins and the dashed curves indicate the inlets. Additionally, a black dash-dotted line is shown, indicating the total deposited sediment volume in the total of the basin and both inlets. The temporal evolution of deposited sediment in fig. 3.20 confirms again that the total system is importing sediment (dash-dotted line is positive), with the updrift sub-basin

being dominant over the downdrift sub-basin, both in total deposited sediment in the basin and in total eroded sediment in the inlet. Furthermore, a slowdown is observed in sedimentation of both sub-basins and inlets. However, the deposited sediment in the total of basin and inlets (dash-dotted line) does not converge to a (quasi-)equilibrium, but increases almost linearly from $t = 100\,\mathrm{yr}$ onwards.

Note that it is no surprise that the updrift sub-basin is dominant over the downdrift sub-basin in terms of total deposited sediment volume, because the basin area of the former is larger (due to the phase difference between the inlets). To correct for this, fig. 3.21 shows the fraction of the basin area that has a bed level smaller than 1.1 m below mean sea level, where 1.1 m is the average sea level amplitude in the basin. Thus, fig. 3.21 shows the fraction of the basin area consisting of shoals that are partly submerged during a tidal cycle. It is seen from this figure that the fraction of the basin consisting of shoals is approximately equal in both sub-basins.

Yet, the evolution of total deposited sediment volume is not enough to draw conclusions about whether the system moves towards an equilibrium or not. For instance, local erosion and sedimentation within a sub-basin is not noticed in that approach. Therefore, also the total volume of the channels in the basins is considered, which is shown in fig. 3.22. Here the channels are (consistent with the approach in § 2.2.2) defined as all parts of the basin with a depth larger than the initial depth of 2 m. The blue (red) curve again indicates the downdrift (updrift) sub-basin. Fig. 3.22 reveals that the rate of change of channel volume approaches zero, pointing at an evolution of at least the channels towards a (quasi-)equilibrium state.

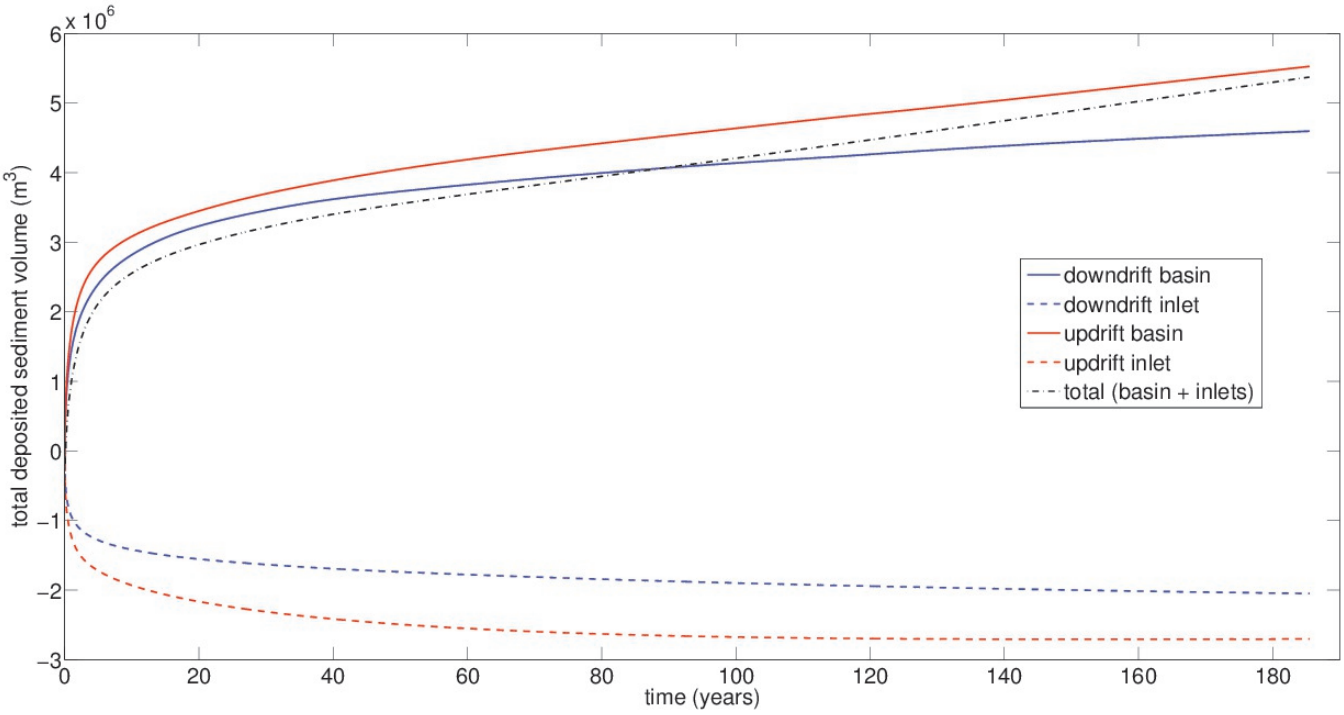

Figure 3.20: Total deposited sediment volume versus time in both inlets, sub-basins and the total system of basin and inlets (excluding the sea).

As a final morphometric parameter, the volumetric sediment exchange rates between the different compartments of the system are considered. This volumetric sediment exchange rate

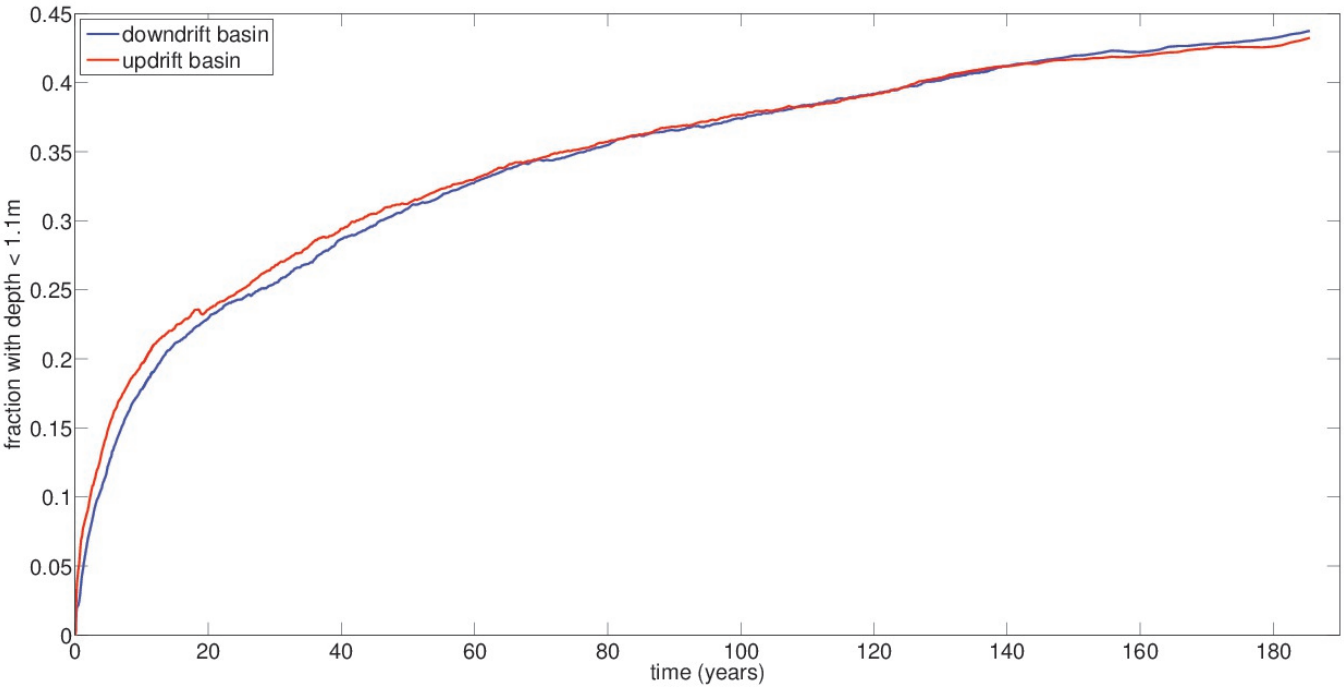

Figure 3.21: Fraction of the basin area with a bed level of less than 1.1 m below mean sea level versus time, indicating the fraction of the basin consisting of partly submerged shoals. The red (blue) curve denotes the updrift (downdrift) sub-basin.

was introduced in § 2.2.3, where it was discussed that it is derived from the total deposited sediment volume for computational reasons. Because the sediment exchange between updrift and downdrift sub-basin is small (cf. e.g., fig. 3.14), the sediment exchange rate between sea, inlets and sub-basins can be estimated by eq. (2.28). The approximation of the sediment exchange rate is shown by the curves in fig. 3.23. Again, blue (red) indicates the downdrift (updrift) sub-basin. Furthermore, the exchange rate from sea to inlet is indicated by the solid lines and the exchange rate from inlet to basin by the dashed lines. Additionally, the exact values (determined by taking the mean value over several tidal periods) are shown at four different times for exchange rates from sea to inlet (diamonds), from inlet to basin (circles) and from downdrift to updrift sub-basin (green squares). Note that the latter is in the approximated curves assumed to be zero.

Fig 3.23 shows during the first 50 yr a decrease in volumetric sediment exchange rate between sea and inlets and between inlets and basin. Also, the the net transport from sea to inlets (solid lines) is larger than the net transport from inlets to basin (dashed lines) in the downdrift sub-system during the whole evolution, which indicates erosion of the inlets. However, in the updrift sub-system a slight inversion takes place, indicating slight sedimentation in the updrift inlet after 185 yr. Furthermore the difference between the two mentioned exchange rates decreases in time, especially for the updrift sub-system, indicating decreasing erosion of the inlets. These findings are in accordance with the previous results (cf. e.g., fig. 3.13). From $t = 140$ yr onwards, the updrift inlet merely functions as a pass-through for sediment that is imported from sea into the updrift sub-basin. Because both sub-systems keep importing sediment, it turns out that no (quasi-)equilibrium is established or will be established within a reasonable timespan after 185 yr in terms of negligible morphological changes. However, both inlets are (almost) stabilised,

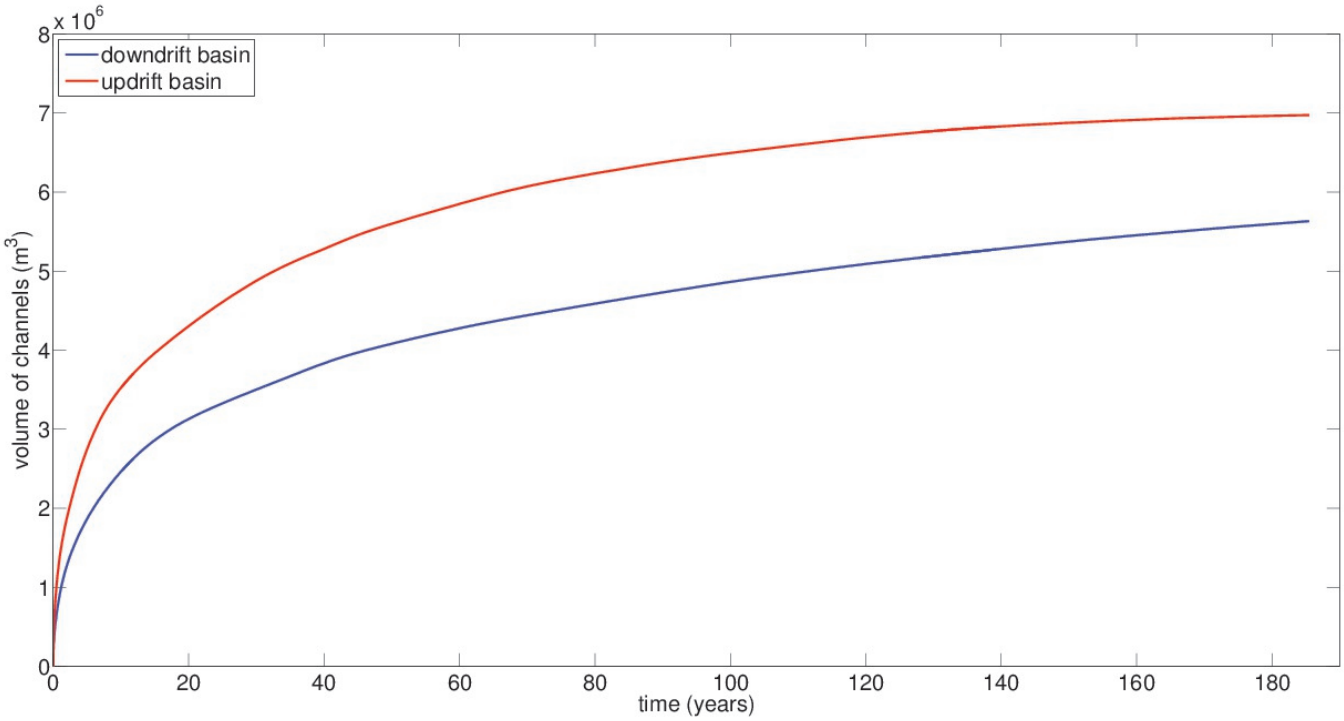

Figure 3.22: Total volume of the channels in the basin (parts with a depth larger than the initial depth of 2 m) versus time for both sub-basins.

so a stable situation (in terms of two inlets staying open) is reached.

Note that up to 70 yr in fig. 3.23 a quite strong variability occurs, which is an artefact of non-zero sediment transport over the (artificially fixed) separation of the two sub-systems. However, because the sediment exchange rate between the sub-basins is still much smaller than the other sediment exchange rates, the approximated exchange rates of fig. 3.23 serve as a good first approximation. From 70 yr onwards, when the actual separation of the two sub-systems has stabilised, the sediment exchange between the sub-basins approaches zero and the approximation of eq. (2.28) holds.

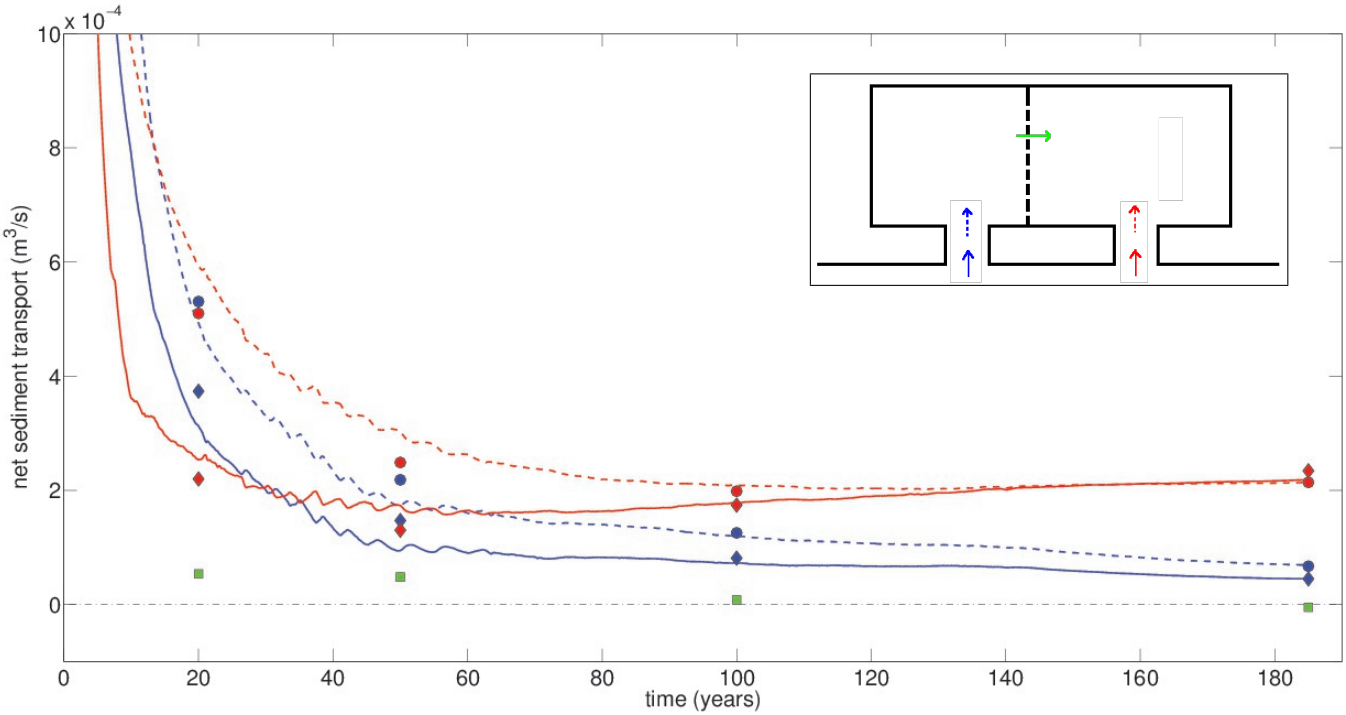

Figure 3.23: Volumetric sediment exchange rates between different parts of the domain (inlets and sub-basins). Red indicates the updrift part and blue the downdrift part.
The symbols indicate net sediment transports from sea to inlet (diamonds) and from inlet to basin (circles) at some moments in time, determined directly from the model data. Additionally, transports from downdrift to updrift basin are visualised by the green squares. These values are non-zero as a result of the artificially fixed separation between the two sub-basins (as defined in § 3.1.1).
The curves indicate volumetric sediment exchange rates from sea to inlet (solid) and from inlet to basin (dashed), calculated from the total deposited sediment volume (cf. eq. (2.28)). The transport between the two sub-basins is neglected here.

3.1.5 Tidal watershed

As already stated in previous sections, there is — especially in net sediment transport — a clear separation of the two sub-basins (cf. figs. 3.12 and 3.14), with a net transport of almost zero, especially after 100 yr. Moreover, fig. 3.14 shows convergence of the net sediment transport in the basin around the separation between the two sub-basins, thereby indicating the development of a tidal watershed. Especially in the initial years of evolution, a non-zero sediment exchange can occur between the two sub-basins (see e.g. the green squares in fig. 3.23 with especially at $t = 50$ yr a value well above zero). Yet, this is caused by the assumption that the separation of the two sub-basins is at a fixed location, whereas in reality it varies slightly in time (cf. fig. 3.1). Besides from the net sediment transports, it becomes clear from the patterns of bed level change shown in fig. 3.3 that the channels of the two sub-systems do not merge and that a topographic high develops from the seaward side of the separation between the sub-basins in the positive cross-shore (y-)direction.

3.2 Changing distance between the inlets

3.2.1 Division into two sub-systems

In this section, three different distances between the inlets will be considered, namely 3 km ('close'), 6 km ('reference') and 9 km ('far'). As was done in fig. 3.1 for the reference case, the location of the boundary between the two sub-basins is quantified by averaging the maximum of the absolute longshore velocity component ($|U_{\max}|$) at $t = 185$ yr over the basin width, and determining local minima. The maximum absolute longshore velocity component is shown for all three cases in fig. 3.24, together with the location of the inlets (dotted lines) and the geometric centre of the basin (solid black line). The minimum near the geometrical centre of the basin is defined as the boundary between the two sub-systems, resulting in locations of $x = 12.6$ km, $x = 12.75$ km and $x = 13.1$ km for distances of 3 km, 6 km and 9 km between the inlets, respectively, and indicated in fig. 3.24 by the dash-dotted lines.

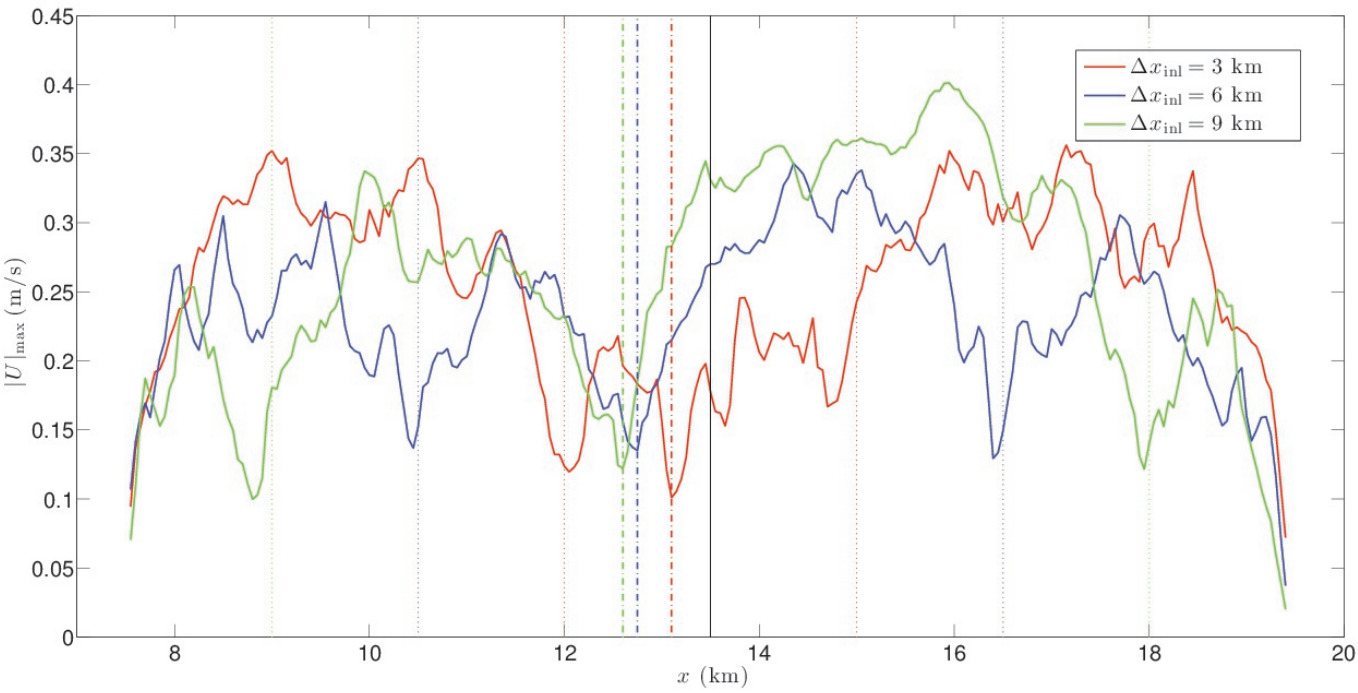

Figure 3.24: The maximum absolute longshore velocity $|U|_{\max}$ in the basin after 185 yr, averaged over the basin width, versus longshore distance x. The distance between the inlets is indicated by the colour: red indicates 'close', blue indicates 'reference' and green indicates 'far'.
The minimum of the maximum width-averaged longshore velocity is determined in the middle part of the basin (between $x = 12.3$ and 14.7 km), with the x-values of the minima given by the dashed-dotted lines. The geometrical centre of the basin is given by the solid black line, and the centres of the inlets are indicated by the coloured dotted lines.

As is shown in fig. 3.24, the boundary between the sub-systems shifts downdrift with increasing distance between the inlets. To investigate this behaviour more closely, an analytical model of Ridderinkhof [1988] is used (see also appendix A) to investigate the effect of the phase difference between the inlets on the maximum of the absolute water transport. Fig. 3.25 shows the maximum of the dimensionless absolute water transport $|q'|$ versus dimensionless distance x'

for four different phase differences of the water level between the inlets, viz. 0°(black), 1.5°(red), 3°(blue) and 4.5°(green). The last three phase differences correspond to the 'close', 'reference' and 'far' cases in the present research, respectively. Specifications on the used parameter values will not be discussed here, but are given in the caption of the figure (for further discussion on the parameter values, see appendix A). From fig. 3.25 it appears that an increasing phase difference (resulting from an increasing distance between the inlets) causes the minimum in $\max(|q'|)$ (and therefore the boundary between the two sub-systems) to shift downdrift.

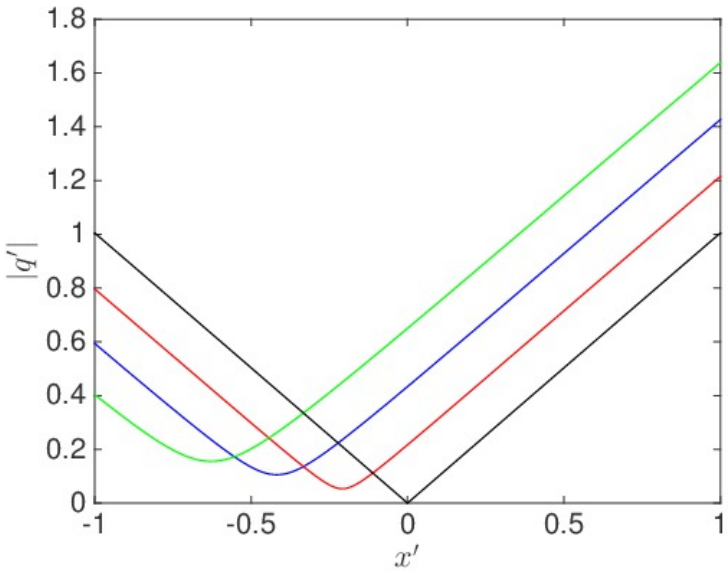

Figure 3.25: The maximum of the dimensionless absolute water transport versus dimensionless distance, making use of the conceptual model of Ridderinkhof [1988] (see appendix A). Four different phase differences between the inlets are shown, viz. $\phi = 0°$ (black), $\phi = 1.5°$ (red), $\phi = 3°$ (blue) and $\phi = 4.5°$ (green). Following model parameter values are used: $b' = h' = l' = Z' = 1$; $C_{\mathrm{D}} = 0.0024$; $\alpha = 3/4$; $H_A = 2\,\mathrm{m}$; $L_A = 4\,\mathrm{km}$; $B_A = 4.5\,\mathrm{km}$; $Z_A = 1.1\,\mathrm{m}$.

Another interesting aspect from fig. 3.24 is the appearance of local minima in $|U|_{\max}$ at the longitudinal positions of the inlets (indicated with dotted lines), which were already visible in fig. 3.1. However, for almost all inlets, these local minima are shifted in the downdrift direction. The reason for the appearance of these minima in $|U|_{\max}$ near the longitudinal positions of the inlets is the divergent behaviour of the flow at the landward side of the inlets (cf. e.g. the unidirectional and along-channel behaviour of the M2 tidal velocity in fig. 3.7). Fig. 3.24 shows that the more an inlet is located towards the downdrift-side of a sub-basin, the more the minimum of $|U|_{\max}$ is shifted downdrift compared to the location of the inlet.

3.2.2 Morphology

In order to capture the main morphological features, fig. 3.26 shows the patterns of the bed level (with respect to the undisturbed sea level) and the change in bed level (compared to the initial bed level) after 185 yr for three different distances between the inlet centres, namely 3 km, 6 km (reference) and 9 km. The main orientation of the updrift channels changes from the updrift tot the downdrift direction with increasing inlet spacing. This is related to the tidal watershed being located closer to the inlets for a small inlet spacing (upper panels of fig. 3.26). Furthermore,

due to the coastal boundary of the basin on the downdrift side, the main orientation of the downdrift channels has changed from the updrift to the downdrift direction in case of a large distance between the inlets (bottom panels of fig. 3.26). This implies that, where the channels were quite uniformly spread in each sub-basin in the reference case (middle panels of fig. 3.26), the main channels in the system with a small distance between the inlets are direct away from division between the sub-basins, and the main channels in the system with a large distance between the inlets are direct towards the division between the sub-basins.

Considering the ebb-tidal deltas, large differences exist between the three studied inlet spacings. In the case of a small distance between the inlets, effectively only one delta is present after 185 yr, whereas for a large distance there are two separate deltas present. In case of a separate delta at the downdrift basin, it is much smaller in area and volume than its updrift counterpart. Note that the maximum bed level change of the separate ebb-tidal deltas increases slightly with increasing distance between the inlets.

3.2.3 Net sediment transport patterns

Fig. 3.27 shows the patterns of net sediment transport (per unit length) in the domain for a distance between the inlets of (from top to bottom) 3 km, 6 km and 9 km at the initial state. For all cases, the general pattern is the same as for the reference case (middle panel of fig. 3.27), namely a residual circulation cell (cf. § 3.1.3). Furthermore, the boundary between downdrift and updrift circulation cells (indicated by cross-shore net transport in the basin towards the seaward side of the basin) is located more downdrift when the distance between the inlets increases. The net sediment transport pattern in the sea is for all three cases similar: a large ebb-dominated pathway at each inlet, which is slightly tilted updrift and a smaller flood-dominated pathway at the updrift side of each inlet, which has a strong updrift orientation.

The pattern of net sediment transport (per unit length) in the domain for the three different distances between the inlets, both after 20 yr and after 185 yr is shown in fig. 3.28. Again, from top to bottom the inlet spacing increases, from 3 km to 6 km and finally 9 km. One of the major differences between the three cases is the direction of main net sediment transport. For a small distance between the inlets, this is away from the separation of the sub-basins, whereas for a large distance the main net transport is towards the separation of the sub-basins. This behaviour of the system is mainly determined by the dimensions of the basin, making only small evolution of channels in the other direction possible. However, a large net sediment transport towards the separation of the sub-basins can also enhance the formation of the tidal watershed. For the net sediment transport in the near-shore sea at $t = 20$ yr (left column of fig. 3.28), no large differences between the three cases are observed, so the main patterns found in § 3.1.3 still apply.

To determine the main channels in terms of the net sediment transport, the divergence of the net sediment transport per length is shown in fig. 3.29 for the three different distances between the inlets, both after 20 yr and after 185 yr. In § 3.1.3 it was already concluded that for the reference case two main channels exist in each sub-basin: one updrift oriented and one downdrift oriented. The upper right panel of fig. 3.29 shows for a small distance between the inlets a downdrift oriented channel in the downdrift sub-basin, and for the updrift sub-basin multiple equally important channels (in terms of net sediment transport), predominantly oriented in the updrift direction. The bottom right panel of fig. 3.29 shows for a large distance between the

inlets an updrift oriented channel in the downdrift sub-basin, and for the updrift sub-basin a dominant channel in the downdrift direction. It turns out that the two main channels that were earlier determined for the reference case in § 3.1.3 (see also middle right panel of fig. 3.29), are more or less a superposition of the main channels that are visible for the 'close' and the 'far' case in the top and bottom row of fig. 3.29, respectively.

Following the procedure of § 3.1.3, the net sediment transport (per unit length) in the basin is averaged over the basin width for further inspection of the net sediment transport. This width-averaged net sediment transport is shown versus the longshore (x-)coordinate in fig. 3.30 for the three distances between the inlets, both at the initial state (top panel) and after 185 yr (bottom panel). The main pattern of the net mean transport being directed from the inlets towards the sides of the basin and from the inlets towards the division of the two sub-basins remains the same as in the reference case (cf. fig. 3.14). Also a location of zero transport occurs in the middle of the basin for all three cases (after 185 yr). For distances of 6 km and 9 km this location of zero transport coincides with the location of the minimum in the maximum absolute width-averaged longshore velocity ($|U|_{\max}$, used as definition for the division between the two sub-basins, cf. fig. 3.24). This indicates negligible sediment exchange between the sub-basins. However, when the inlets are located close together (red curve in fig. 3.30), the location of zero net transport coincides with the geometrical centre of the basin. In spite of this deviation, still a small net sediment transport is found over the boundary between the two sub-basins (compared to net transports outside the interval $12\,\mathrm{km} < x < 14\,\mathrm{km}$).

Note that the intensity of the net longshore width-averaged sediment transport of fig. 3.30 increases with increasing distance between one of the sides of the sub-basin and the inlet (dotted lines in fig. 3.30). This means that for the updrift sub-basin, updrift transport is largest for a small distance between the inlets, and downdrift transport is largest for a large distance between the inlets (for the downdrift sub-basin vice versa). This is already the case for the initial state (upper panel of fig. 3.14), suggesting a purely hydrodynamic origin of this phenomenon.

As was done in fig. 3.15 for the reference case, the net sediment transport patterns (cf. fig. 3.28) are also determined by using the simple transport formulation of eq. (2.29). The parameterised net sediment transport patterns are shown in fig. 3.31 for different distances between the inlets (top to bottom: 3 km, 6 km and 9 km), both after 20 yr (left column) and after 185 yr (right column). The overall characteristics are the same as already shown from the extended transport formulation (cf. fig. 3.28). Note that, as in the reference case, fig. 3.31 shows larger sediment transport over the shoals than observed in fig. 3.28, because critical shear stress is not accounted for in the simple transport formulation. In all three cases and for both inlets, a net import of sediment is observed, which is further examined by splitting the net sediment transport in a part induced by the residual flow (visualised in fig. 3.32) and a part induced by tidal asymmetry (visualised in fig. 3.33). The main net transport patterns in the channels of the basin that can be deduced from these figures are similar for the three cases, although channels and shoals are of course located differently in the basin. Also the net transport in the sea shows similar patterns for the three cases, taking into account that the ebb-tidal deltas are located further apart with increasing distance between the inlets. Thus, the main results of figs. 3.15 and 3.16 hold for all three distances between the inlets.

To have a closer look at the net sediment import through the inlets, a zoomed view of figs. 3.32 and 3.33 is provided in figs. 3.34–3.37. Fig. 3.34 shows the patterns of the parameterised net sediment transport induced by the residual flow in the downdrift inlet, both after 20 yr (left)

and after 185 yr (right). Which shows an export of sediment for all studied cases that decreases in time. The main pattern is the same in all three cases, except for the landward side of the inlet. There, a decreasing sediment import with increasing distance between the inlets is found at the downdrift side and a decreasing export of sediment with increasing distance between the inlets is found at the updrift side. Fig. 3.35 shows the same situation, but for the updrift inlet. The dominant behaviour is net sediment import, but also an exporting pattern is found at the updrift landward side of the inlet. The main importing behaviour strengthens in time, whereas the exporting behaviour weakens in time. Furthermore, the net sediment import (per unit length) is larger for a larger distance between the inlets. Fig. 3.36 shows the patterns of the parameterised net sediment transport induced by tidal asymmetry int the downdrift inlet, both after 20 yr (left) and after 185 yr (right). All cases show similar behaviour as the reference case (an import of sediment), without large differences. Finally, fig. 3.37 shows the same situation, but now for the updrift inlet. Here a net import of sediment is observed, but with an exporting component on the updrift side that becomes broader with increasing distance between the inlets.

As was done in figs. 3.17 and 3.18 for the reference case, the patterns of net sediment transport in the inlets are further studied by determining the evolution of the different components of the simple transport formula (used in figs. 3.31–3.37) in both inlets. Firstly, fig. 3.38 shows the cosine of the phase difference between the M2 and M4 tidal current ellipses versus time, in the centre of each inlet. The left (right) column visualises the downdrift (updrift) basin, and from top to bottom the distance between the inlets increases from 3 km to 6 km and finally 9 km. All three cases show similar behaviour, so the main conclusions of fig. 3.17 remain valid. For the downdrift inlet, the only main difference between the studied cases is a smaller decrease of the sea level phase difference. For the updrift inlet, the main difference between the studied cases is a larger decrease of the phase difference of the tidal ellipse with increasing distance between the inlets, with even a change of sign for a distance of 9 km between the inlets (bottom right panel of fig. 3.38). This is the main cause for the broadening of the sediment export component of the net sediment transport due to tidal asymmetry (and to a lesser extent due to the residual flow) in the updrift inlet for increasing distance between the inlets (cf. right column of fig. 3.37).

Fig. 3.39 shows the other components that contribute to the parameterised net sediment transport, namely residual velocity (green) and semi-major axes of both M2 (blue) and M4 (red) tidal ellipses, all relative to the value at $t = 20$ yr. Again, the left (right) column indicates the downdrift (updrift) inlet and from top to bottom the distance between the inlets increases. All three cases show similar behaviour, so the main conclusions of fig. 3.18 remain valid. The main differences between the studied cases are a decrease of the M4 semi-major axis in the updrift inlet and a large increase of the residual velocity in the updrift inlet with increasing distance between the inlets. The former contributes to the decreased sediment import induced by tidal asymmetry with increasing distance between the inlets (right column of fig. 3.37), whereas the latter is the main cause of the increased sediment import due to the residual flow with increasing distance between the inlets (right column of fig. 3.35).

3.2.4 Evolution of morphometric parameters

In order to evaluate the sediment exchange between the different parts of the system (sea, inlets and sub-basins), two morphometric parameters are evaluated in this section. The first parameter is the total deposited sediment volume, which is visualised versus time in the upper panel of fig. 3.40. the three distances between the inlets are indicated by red (3 km), blue

(6 km, reference) and green (9 km). In this figure, the updrift sub-system is indicated with solid curves and the downdrift sub-system with dashed curves. Both sub-basins are indicated by the positive values (deposited sediment), whereas the inlets are indicated the negative values (eroded sediment), with always more deposited sediment in the sub-basins than eroded sediment in the associated inlet (net import of sediment). The bottom panel of fig. 3.40 shows the total deposited sediment volume in time for both inlets and both sub-basins together, which indicates the total imported sediment in the system. The colours indicate the same cases as in the upper panel.

For all cases, the total deposited sediment in the updrift sub-basin (dotted lines in top panel of fig. 3.40) dominates over that in the downdrift sub-basin (solid lines in top panel of fig. 3.40). However, for increasing distance between the inlets, the difference in deposited sediment in the sub-basin between the downdrift (solid curves) and the updrift sub-basin (dashed curves) decreases. For the case where the inlets are far apart (green curves in top panel of fig. 3.40), this difference has almost disappeared. This is striking, because the difference in sub-basin area increases with increasing inlet spacing (cf. fig. 3.24). Furthermore, for increased inlet spacing, the total eroded sediment increases in the updrift inlet and decreases in the downdrift inlet. Consequently, the difference in total eroded sediment in the inlets increases with increased inlet spacing. When the inlets are located close together, the downdrift inlet has even a larger amount of total eroded sediment than the updrift inlet from 170 yr onwards.

From the bottom panel of fig. 3.40 it is learned that for all studied distances between the inlets, an almost linear increase of total deposited sediment volume occurs, corresponding with a constant net sediment import rate. This net sediment import decreases with increasing inlet spacing, and especially the difference in import between a distance of 3 km (red curve in fig. 3.40) and a distance of 6 km (blue curve in fig. 3.40) is striking. Comparing with the upper panel of fig. 3.40 learns that this large import for a small inlet spacing is mainly the result of a decreasing increase of total deposited sediment volume in the updrift sub-basin (dashed lines with positive values in the upper panel of fig. 3.40). Another contribution of this effect comes from the decreased erosion in the updrift inlet for an inlet spacing of 3 km (compared to 6 km and 9 km, dashed lines with negative values in the upper panel of fig. 3.40). This is caused by the magnitude of the residual flow in the updrift inlet (green curves in right column of fig. 3.39), a decreasing M4 velocity amplitude (red curves in right column of fig. 3.39) and a decreasing phase difference between the M2 and M4 tidal current ellipses (right column of fig. 3.38). Thus, both net sediment transport induced by the residual flow and induced by tidal asymmetry in the updrift sub-system cause a reduction of sediment import in the total system with increasing inlet spacing.

Earlier in this section, it was concluded that after 185 yr the sediment exchange between the sub-basins is (as in the reference case) negligible. Therefore, eq. 2.28 is a reasonable approximation of the net sediment transports between sea, inlets and basin. Therefore, these approximated volumetric sediment exchange rates are the second morphometric parameter studied in this section, and is shown in fig. 3.41, were the top (bottom) panel shows the downdrift (updrift) sub-system. For each of the three different distances between the inlets, in the downdrift sub-system (upper panel in fig. 3.41), net sediment transports from sea to inlet are smaller than transports from inlet to basin. Also, there is hardly any effect of the distance between the inlets on net sediment transport from inlet to basin in the downdrift system. The transport from sea to inlet is slightly smaller when the distance between the inlets is small. For the updrift sub-system (lower panel in fig. 3.41), sediment exchange rates are in all cases larger than in the

downdrift sub-system. The magnitude of the net transport decreases with increasing distance between the inlets. This implies that the further the inlets are separated, the more equal sediment transports in both sub-systems become. Furthermore, in the first 150 yr transport from inlet to basin is larger than that from sea to inlet in the updrift part ($q^{\mathrm{u}}_{\mathrm{ib}} < q^{\mathrm{u}}_{\mathrm{si}}$), indicating erosion of the inlet. This difference decreases in time, and the inequality is in all cases even reversed during the last decades of simulation, indicating slight sedimentation of the inlet.

3.2.5 Tidal watershed

As was discussed for the reference case (see § 3.1.5), the vanishing of the longshore width-averaged net sediment transport is a good indication of the appearance of a tidal watershed. It is clear that the watershed defined in this way is at the location where the minimum in $|U|_{\max}$ is attained for distances of 6 km and 9 km between the inlets. However, for a distance of 3 km between the inlets (red line in the lower panel of fig. 3.24), the watershed appears to be located exactly at the geometrical centre of the basin, whereas the minimum in $|U|_{\max}$ is shifted downdrift. As a measure for the efficiency of the watershed in separating the two sub-basins, the minimum in the absolute maximum width-averaged velocity $|U|_{\max}$ in the basin is used, as was already shown in fig. 3.24. It turns out that the minimum of $|U|_{\max}$ for an inlet spacing of 3 km is smaller than the minimum for an inlet spacing of 6 km or 9 km, which are approximately equal. Thus, the watershed separates the sub-basins more effectively for inlets that are located close together.

As an indication for the rate at which the watershed develops, the convergence of the net sediment transport can be used. However for a larger spacing between the inlets, it takes longer for the channel-shoal systems to meet. Because the morphologic evolution slows down in time (cf. e.g., figs. 3.20 and 3.23), a fair comparison is not possible. Thus, a definitive answer is only obtained when all three systems have reached a (quasi-)equilibrium bathymetry. Nevertheless, the initial net sediment transport patterns can give a first indication of the tendency of the system in its later evolution. The converge of the net longshore sediment transport at the initial state can therefore serve as a measure of rate at which the watershed develops. For that reason, fig. 3.42 shows the divergence of the initial net longshore sediment transport per length, averaged over the basin width, versus the longshore (x)-coordinate. In the inlet region a divergence of the net sediment transport occurs, and somewhat downdrift and updrift of each inlet, a region of convergence of net sediment transport exists. For the development of the watershed the updrift side of the downdrift sub-basin and the downdrift side of the updrift sub-basin are of interest, because these convergent regions will move in time towards the final location of the watershed. For the downdrift sub-basin there is no difference in this convergent behaviour of the net width-averaged longshore sediment transport between the different cases. However, for the updrift sub-basin, the convergence of the net width-averaged longshore sediment transport increases with increasing distance between the inlets. This than leads to the conclusion that the watershed develops more rapidly for a large distance between the inlets.

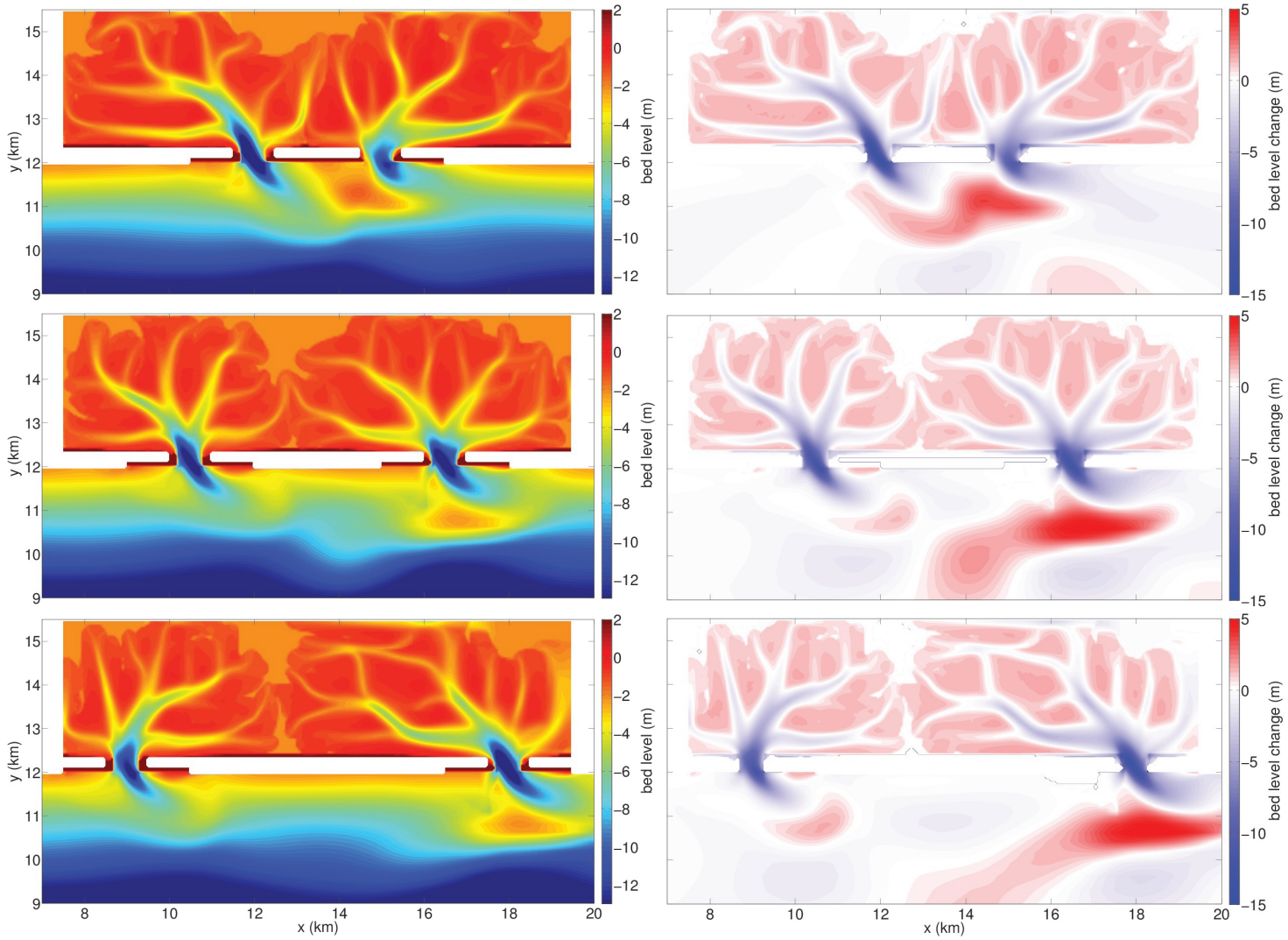

Figure 3.26: Left: colour plots of the bed level (in meters) after 185 yr with 0 representing mean water level. Right: colour plots of the change in bed level (in meters) in the domain after 185 yr, with red representing levels higher and blue lower than the initial bed level of 2 m. From top to down, the distance between the inlets is enlarged from 3 km to 6 km (reference) and finally 9 km.

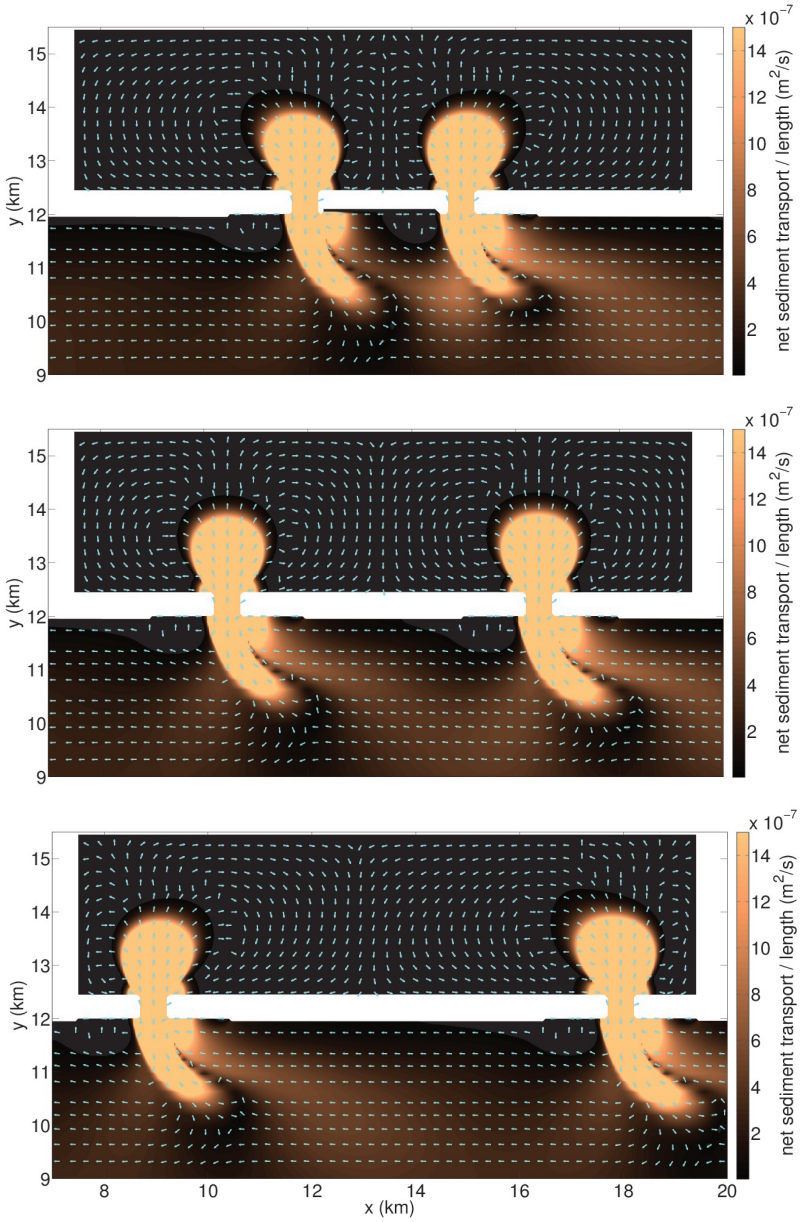

Figure 3.27: Vector field of the net sediment transport per unit length at the initial state. From top to bottom, the rows show an increasing distance between the inlets, viz. 3 km, 6 km and 9 km. The magnitude of the transport is indicated by the colours.

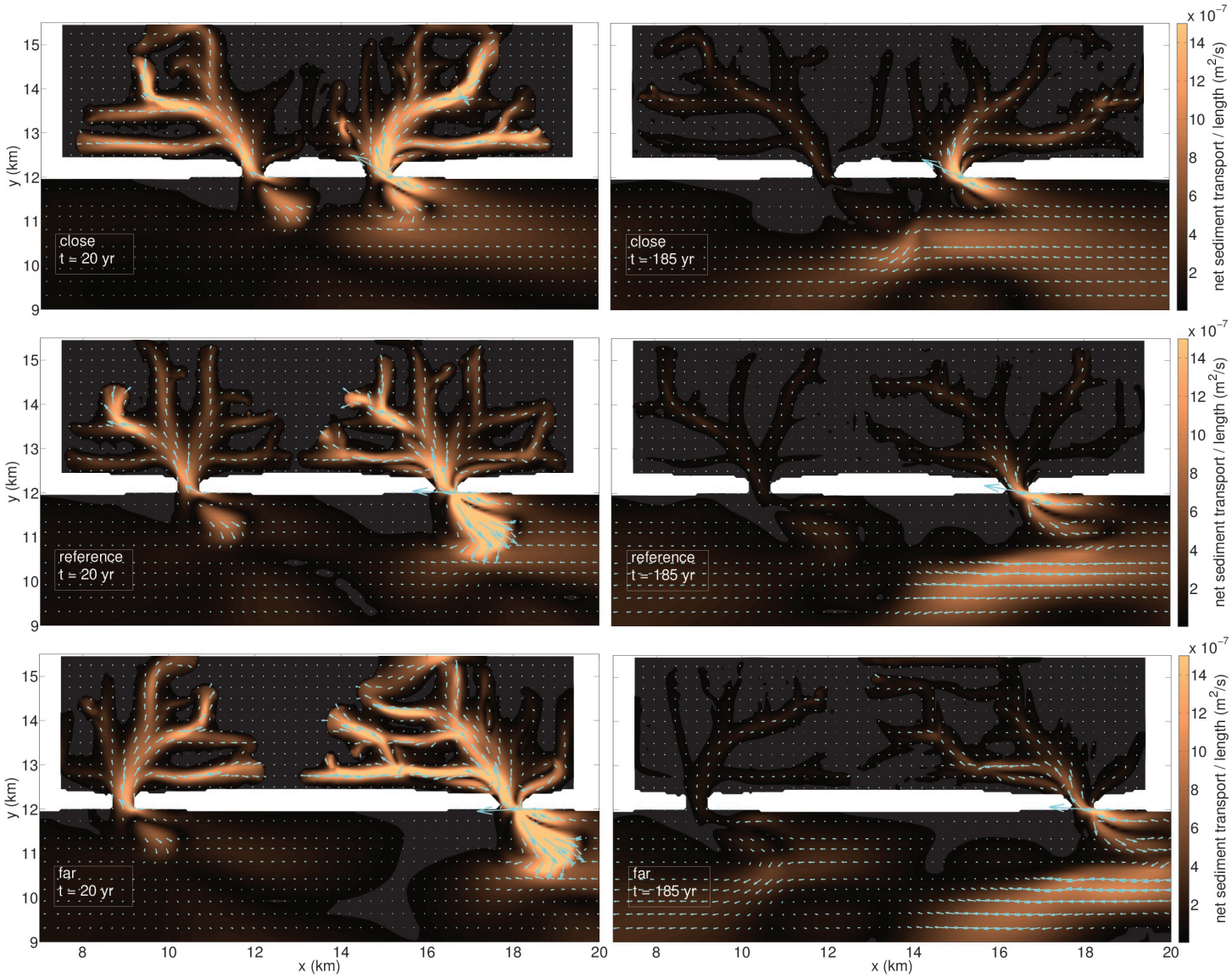

Figure 3.28: Vector field of the net sediment transport per unit length at $t = 20\,\mathrm{yr}$ (left column) and at $t = 185\,\mathrm{yr}$ (right column). From top to bottom, the rows show an increasing distance between the inlets, viz. 3 km, 6 km and 9 km. The magnitude of the transport is highlighted by the colours.

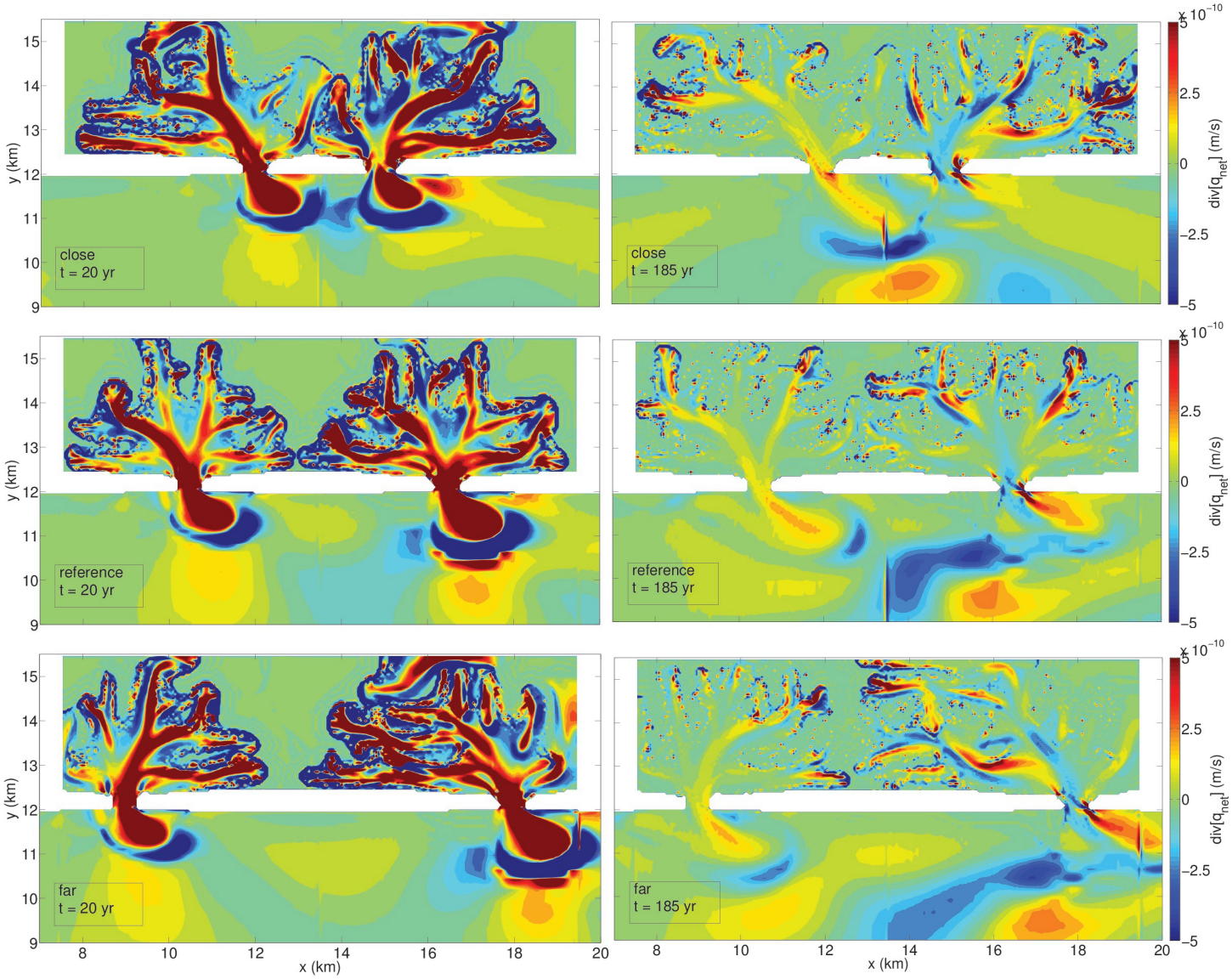

Figure 3.29: Divergence (in m/s) of the net sediment transport per unit length in the basin, at $t = 20\,\mathrm{yr}$ (left column) and at $t = 185\,\mathrm{yr}$ (right column). From top to bottom, the rows show an increasing distance between the inlets, viz. 3 km, 6 km and 9 km.

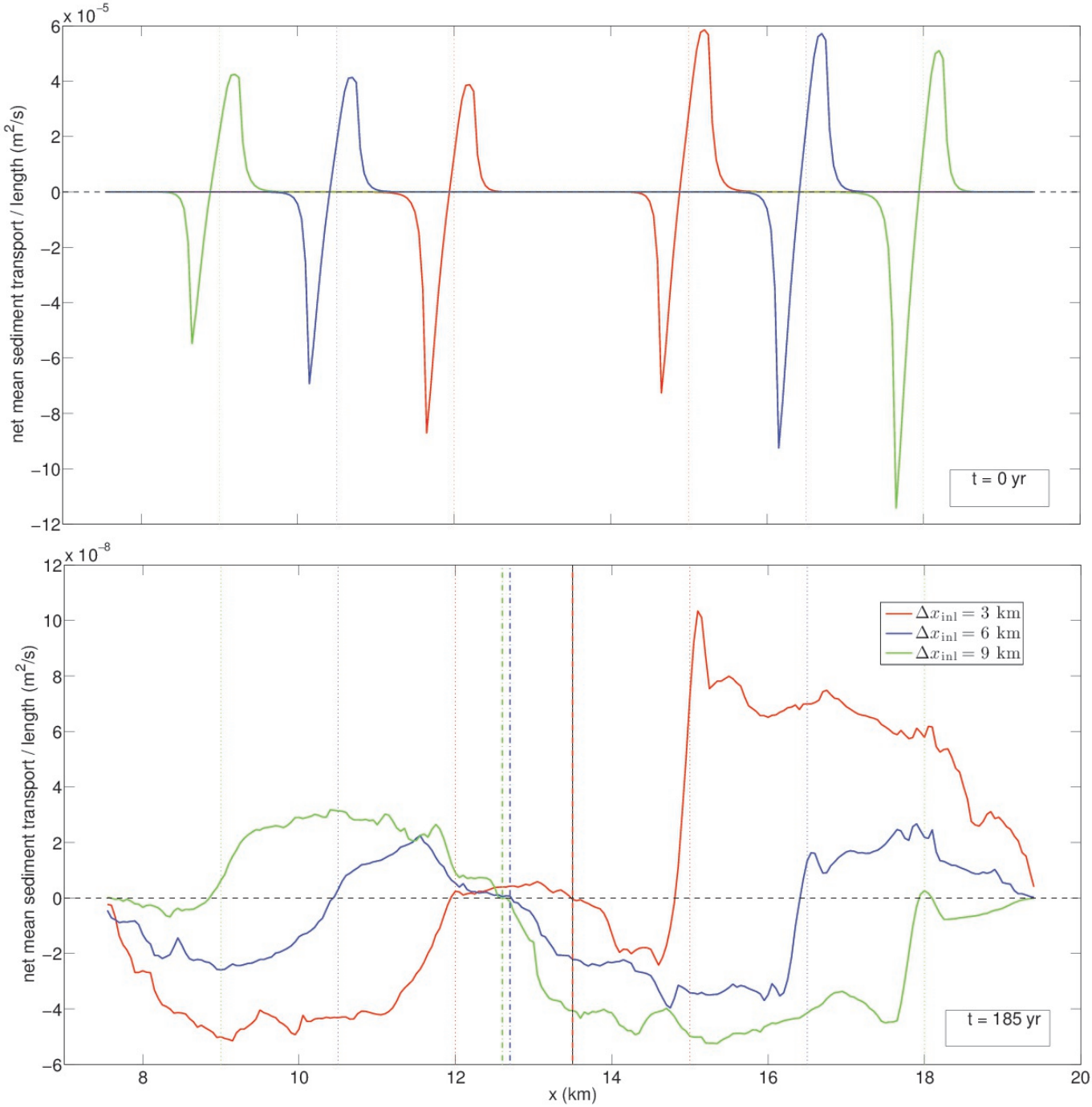

Figure 3.30: The net sediment transport (per unit length) averaged over the width B of the basin, versus longshore distance at the initial state (top panel) and at $t = 185\,\mathrm{yr}$ (bottom panel). The distance between the inlets is indicated by the colours: red indicates 'close', blue indicates 'reference' and green indicates 'far'. The centres of the inlets are indicated by the coloured dotted lines.
Additionally, in the lower panel the minimum of the net width-averaged sediment transport is determined in the middle part of the basin (between $x = 12.3$ and $14.7\,\mathrm{km}$), with the x-values of the minima given by the dashed-dotted lines. The geometrical centre of the basin is given by the solid black line.

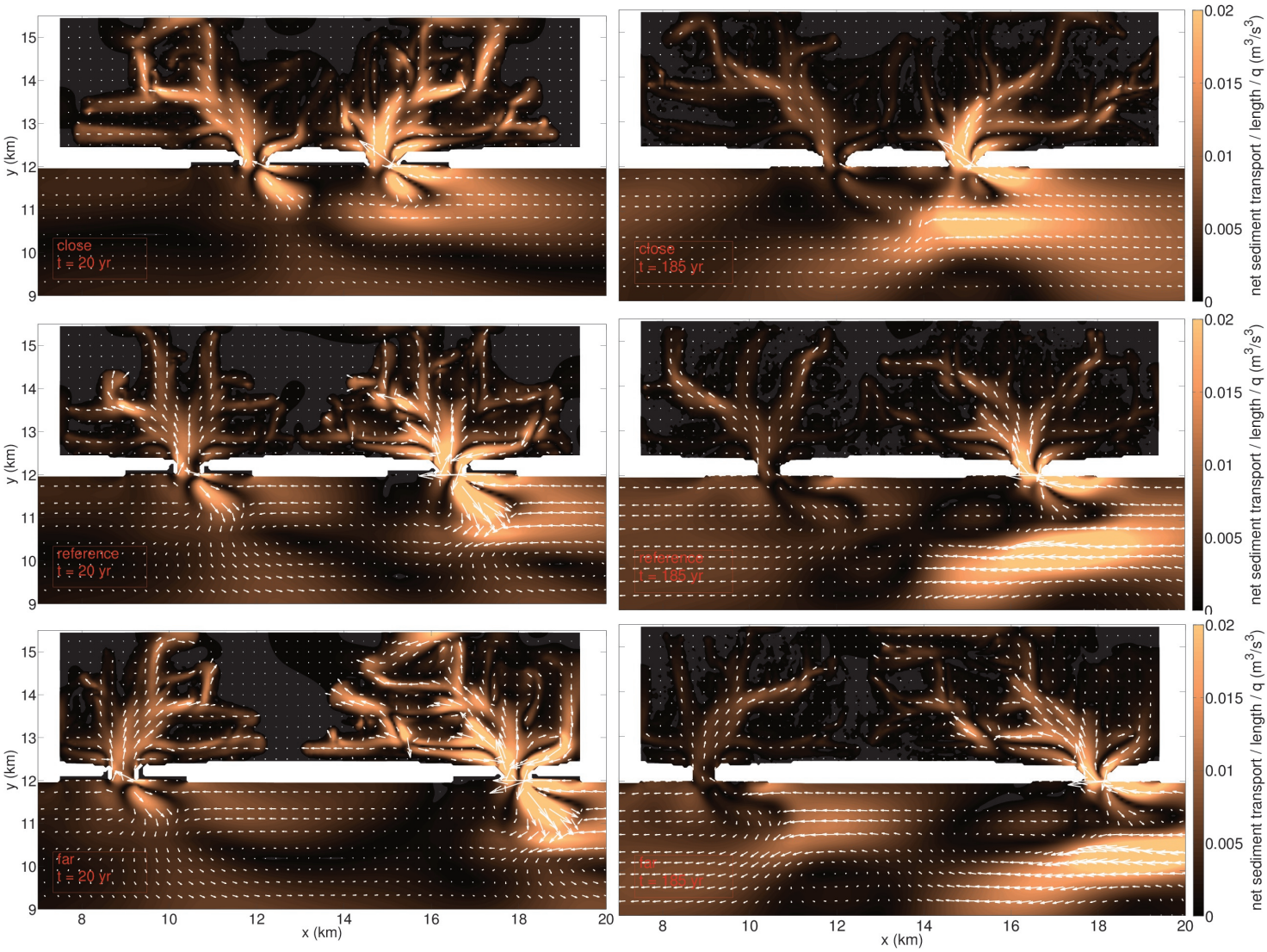

Figure 3.31: Vector field of the net sediment transport (divided by a constant $\hat{q}$, see § 2.2.4) as parameterised by eq. (2.31). Colours highlight the magnitude of the sediment transport. Left column: $t = 20\,\text{yr}$. Right column: $t = 185\,\text{yr}$. From top to bottom, the rows show an increasing distance between the inlets (3 km, 6 km and 9 km). Magnitudes of the transport are highlighted by the colours.

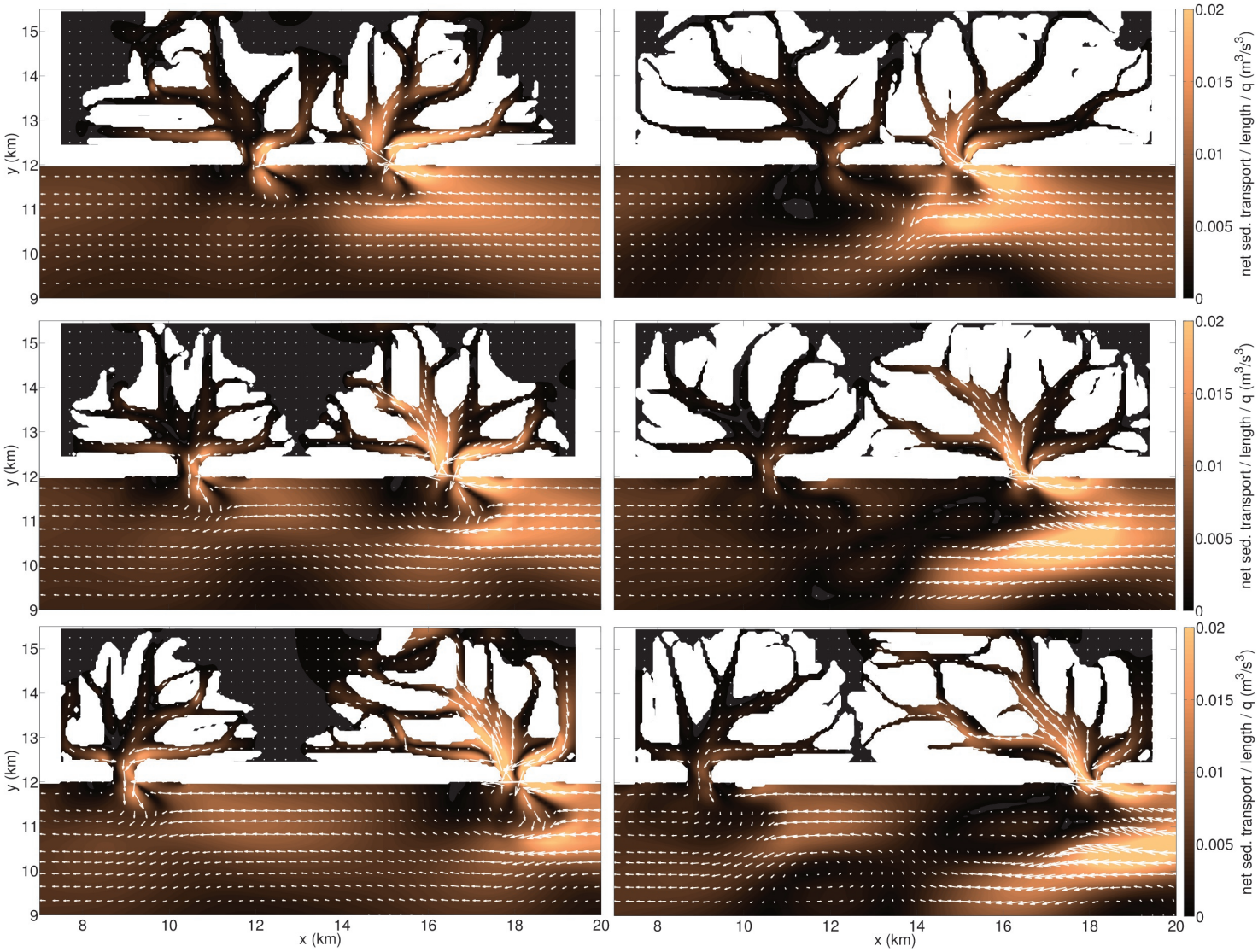

Figure 3.32: Vector field of the net sediment transport (divided by a constant $\hat{q}$, see § 2.2.4) due to interaction of residual/M2 tidal velocities, as parameterised by eq. (2.31). Left column: $t = 20\,\mathrm{yr}$. Right column: $t = 185\,\mathrm{yr}$. From top to bottom, the rows show an increasing distance between the inlets. Magnitudes of the transport are highlighted by the colours. Grid cells that are partly submerged during a tidal cycle are excluded.

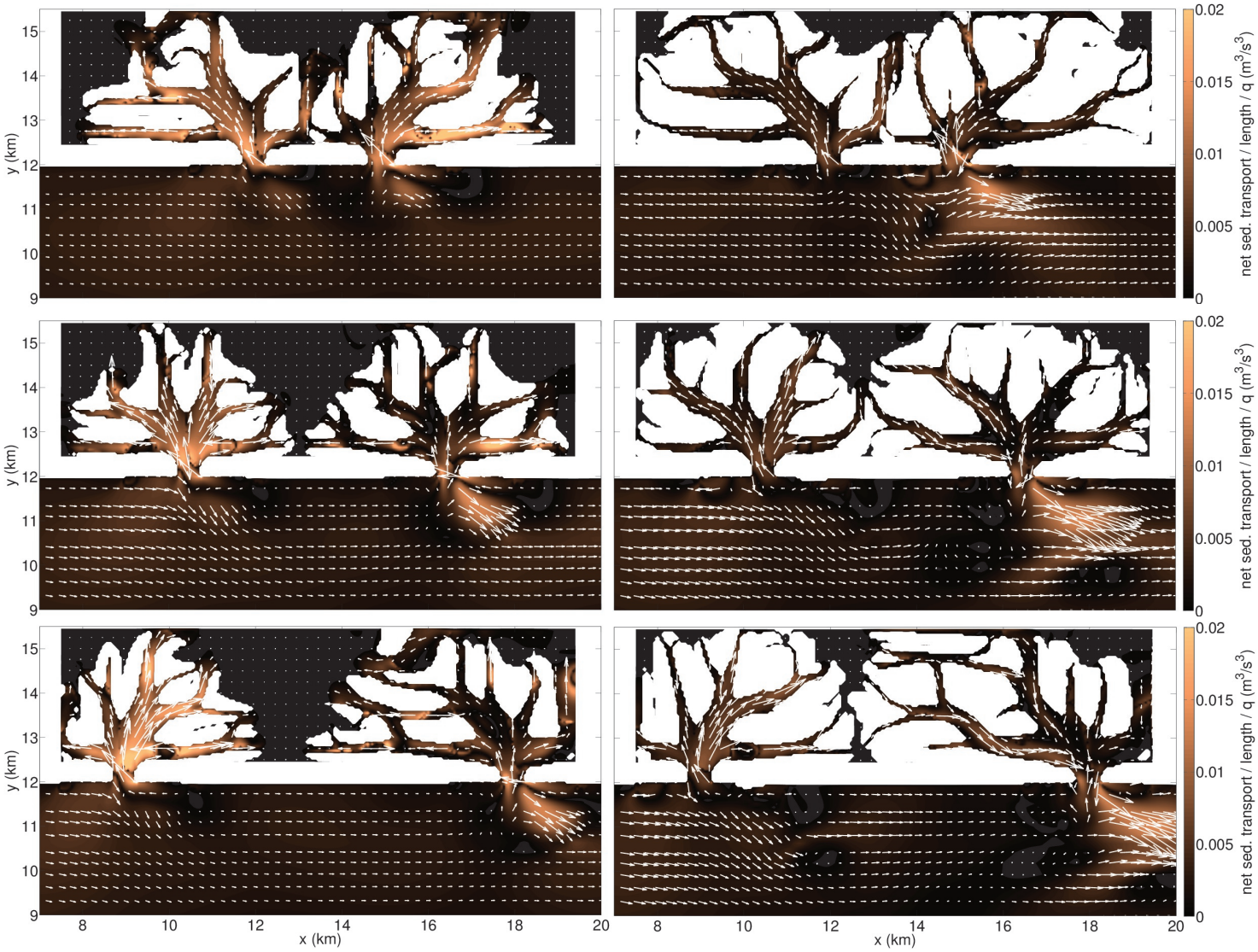

Figure 3.33: Vector field of the net sediment transport (divided by a constant $\hat{q}$, see § 2.2.4) due to joint action of M2 and M4 tidal velocities (tidal asymmetry), as parameterised by eq. (2.31). Left column: $t = 20\,\mathrm{yr}$. Right column: $t = 185\,\mathrm{yr}$. From top to bottom, the rows show an increasing distance between the inlets. Magnitudes of the transport are highlighted by the colours. Grid cells that are partly submerged during a tidal cycle are excluded.

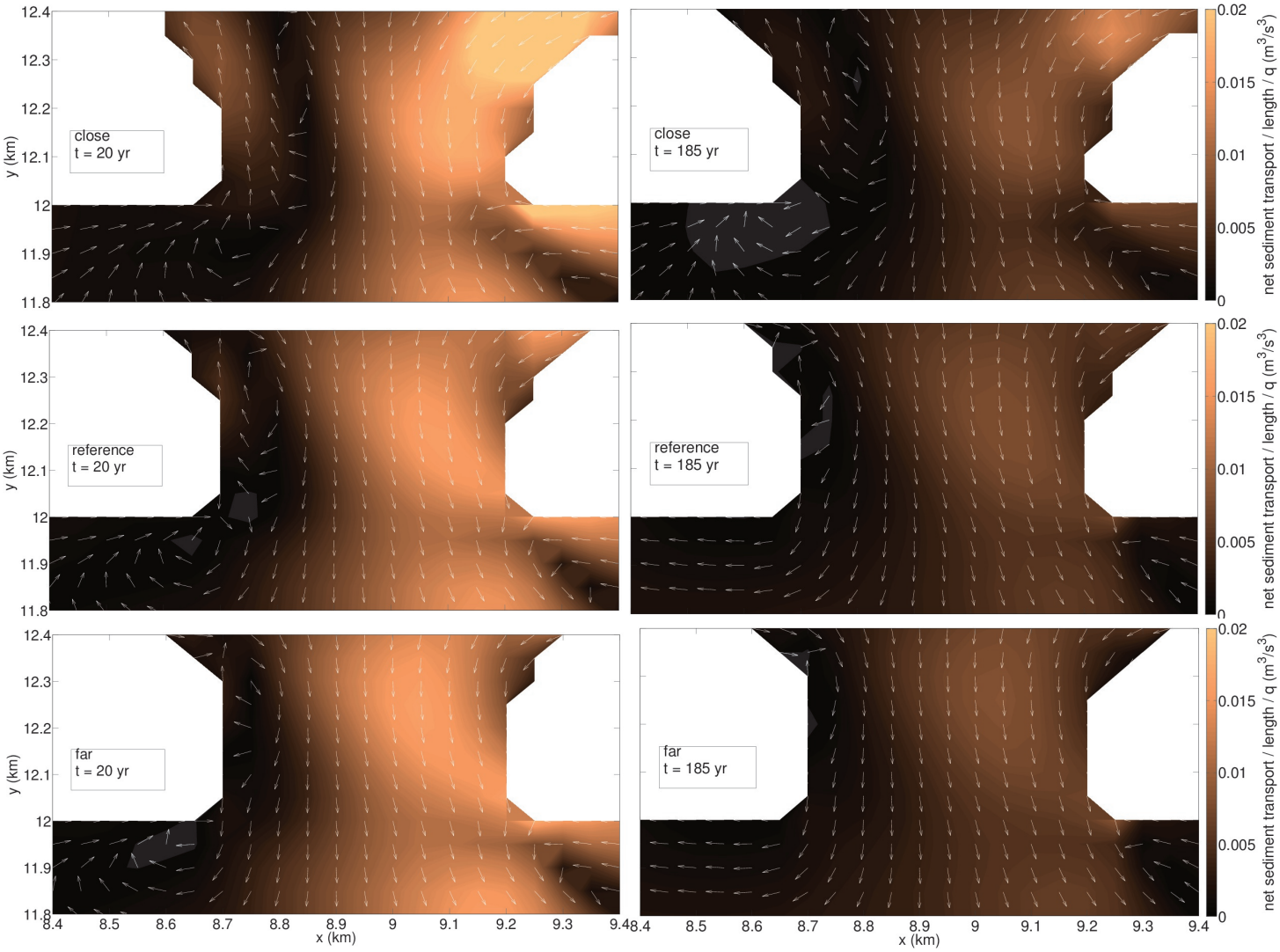

Figure 3.34: Vector field of the net sediment transport (divided by a constant $\hat{q}$, see § 2.2.4) due to joint action of residual and M2 tidal velocities, as parameterised by eq. (2.31) at the downdrift inlet. Colours highlight the magnitude of the sediment transport. Left column: $t = 20\,\mathrm{yr}$. Right column: $t = 185\,\mathrm{yr}$. Top: 3 km between the inlets; middle: 6 km between the inlets (reference case); bottom: 9 km between the inlets.

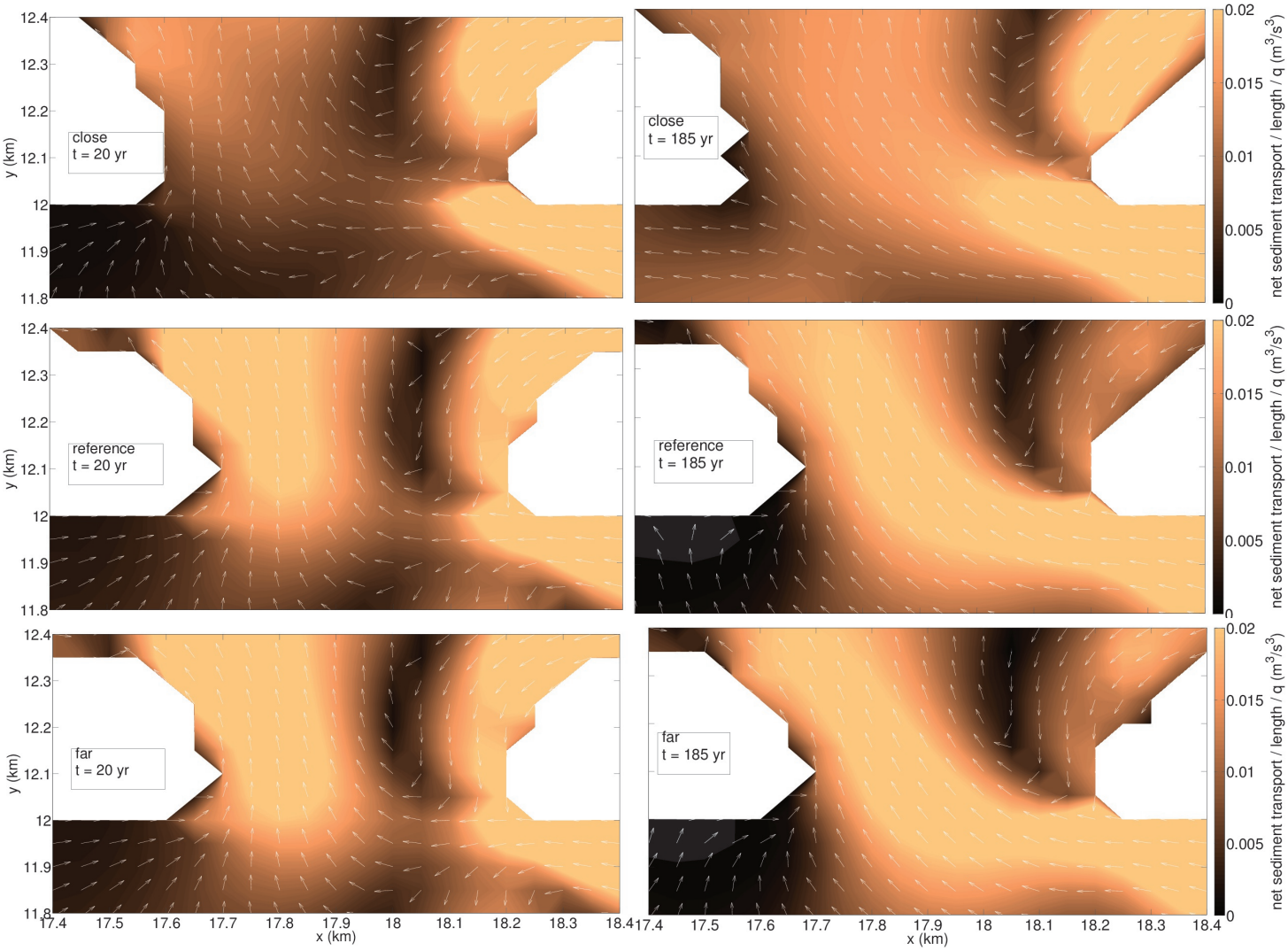

Figure 3.35: Vector field of the net sediment transport (divided by a constant $\hat{q}$, see § 2.2.4) due to joint action of residual and M2 tidal velocities, as parameterised by eq. (2.31) at the updrift inlet. Colours highlight the magnitude of the sediment transport. Left column: $t = 20\,\text{yr}$. Right column: $t = 185\,\text{yr}$. Top: 3 km between the inlets; middle: 6 km between the inlets (reference case); bottom: 9 km between the inlets.

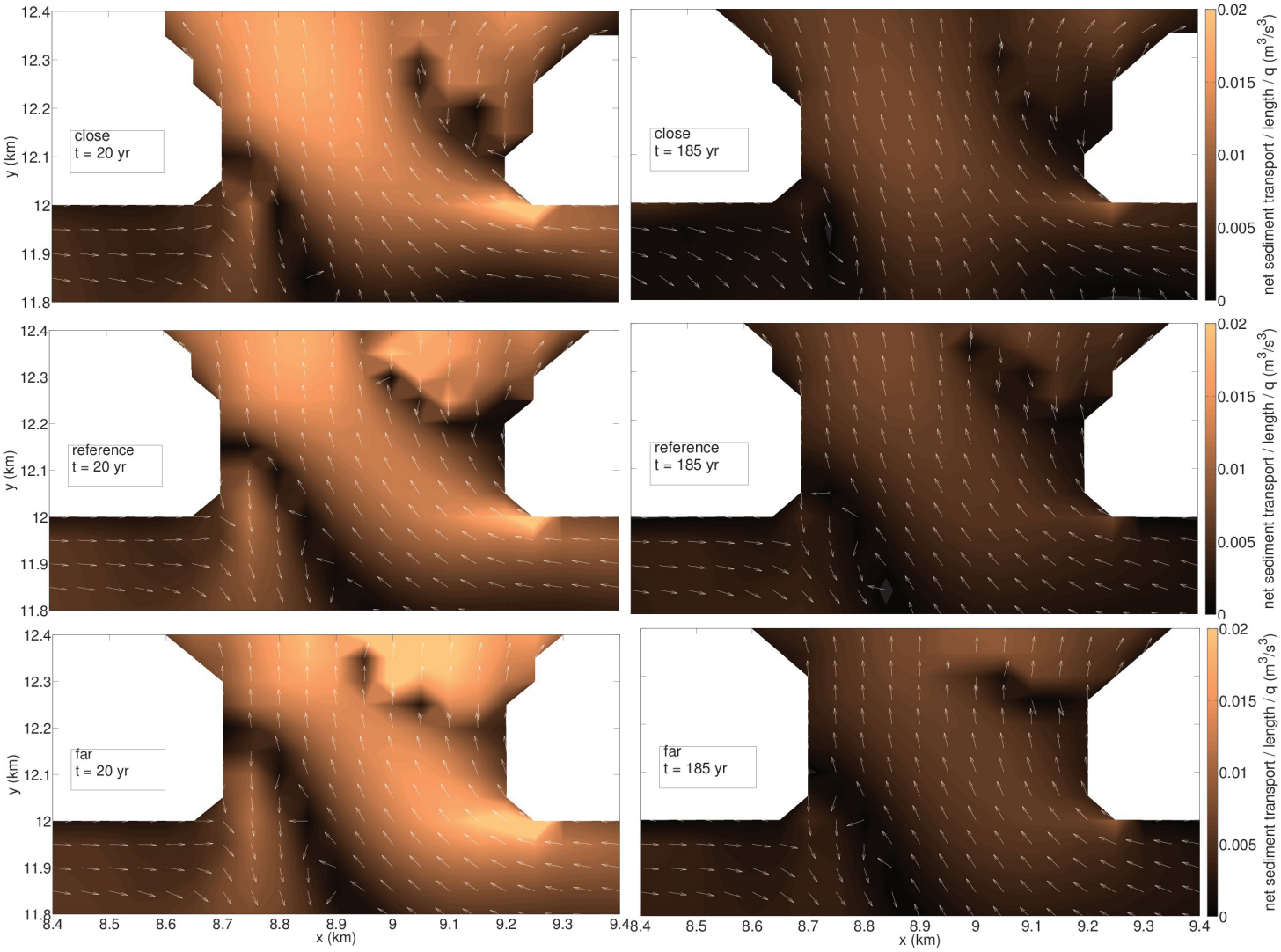

Figure 3.36: Vector field of the net sediment transport (divided by a constant $\hat{q}$, see § 2.2.4) due to joint action of M2 and M4 tidal velocities, as parameterised by eq. (2.31) at the downdrift inlet. Colours highlight the magnitude of the sediment transport. Left column: $t = 20\,\mathrm{yr}$. Right column: $t = 185\,\mathrm{yr}$. Top: 3 km between the inlets; middle: 6 km between the inlets (reference case); bottom: 9 km between the inlets.

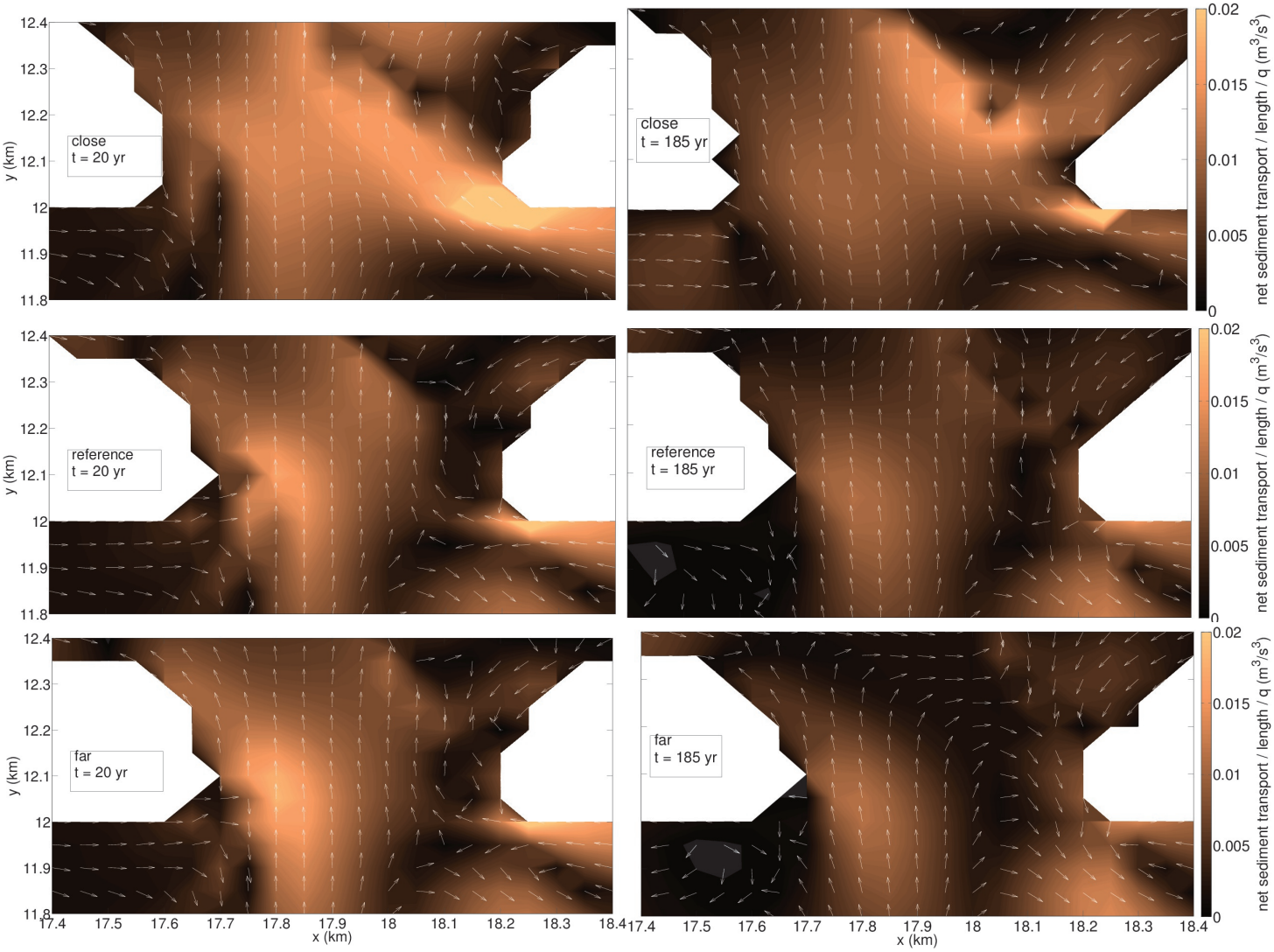

Figure 3.37: Vector field of the net sediment transport (divided by a constant $\hat{q}$, see § 2.2.4) due to joint action of M2 and M4 tidal velocities, as parameterised by eq. (2.31) at the updrift inlet. Colours highlight the magnitude of the sediment transport. Left column: $t = 20\,\text{yr}$. Right column: $t = 185\,\text{yr}$. Top: 3 km between the inlets; middle: 6 km between the inlets (reference case); bottom: 9 km between the inlets.

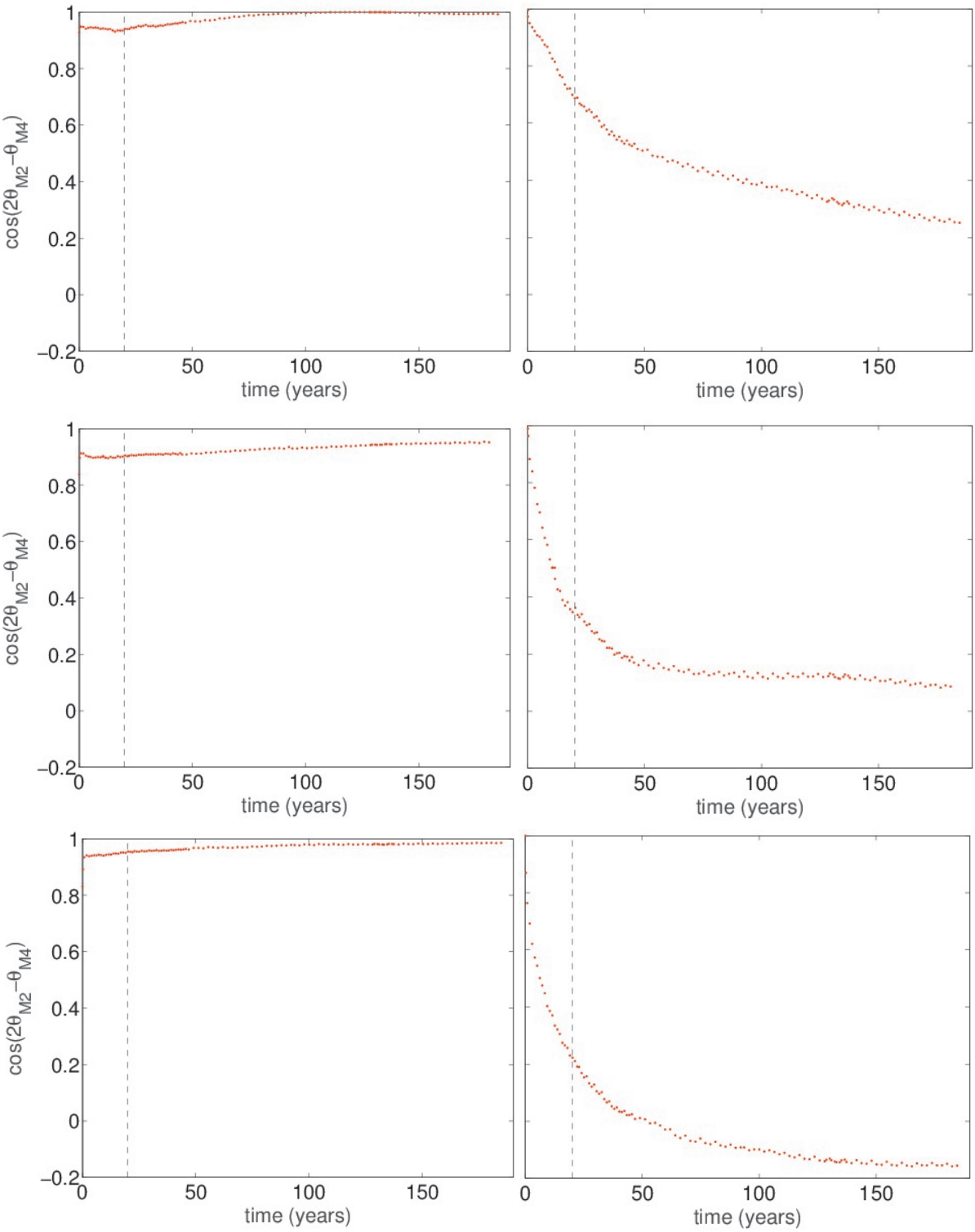

Figure 3.38: The cosine of the phase difference between M2 and M4 tidal velocity ellipses ($\cos(2\theta_{\mathrm{M2}} - \theta_{\mathrm{M4}})$ in time. Left: downdrift inlet. Right: updrift inlet. From top to bottom the distance between the inlets increases: 3 km, 6 km (reference case) and 9 km respectively.

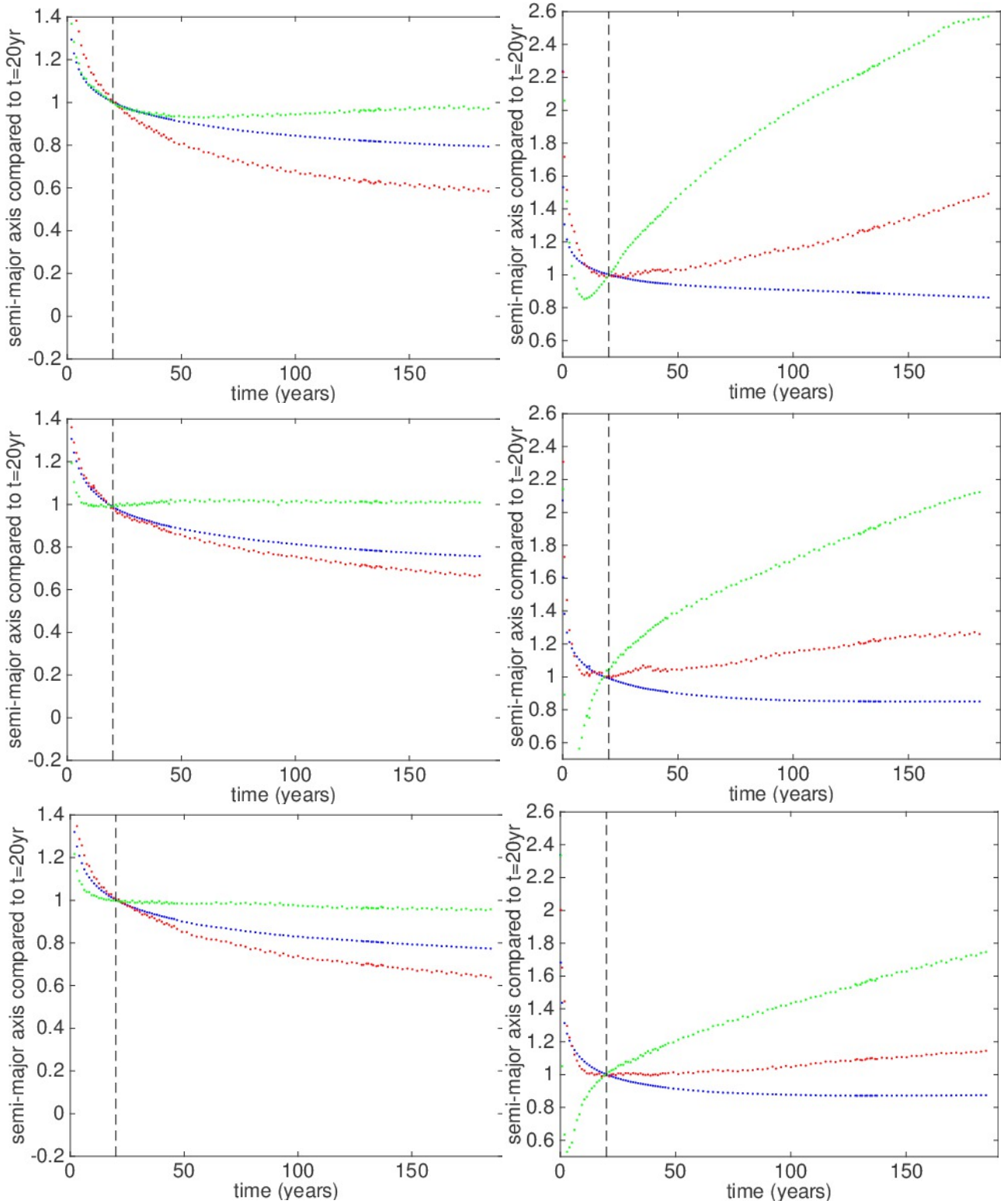

Figure 3.39: The semi-major axis of M2 and M4 tidal ellipses in time. Green indicates M0 (residual component), blue indicates M2 and red indicates M4. Left: downdrift inlet. Right: updrift inlet. From top to bottom the distance between the inlets increases: 3 km, 6 km (reference case) and 9 km respectively. The vertical dashed line indicates $t = 20$ yr.

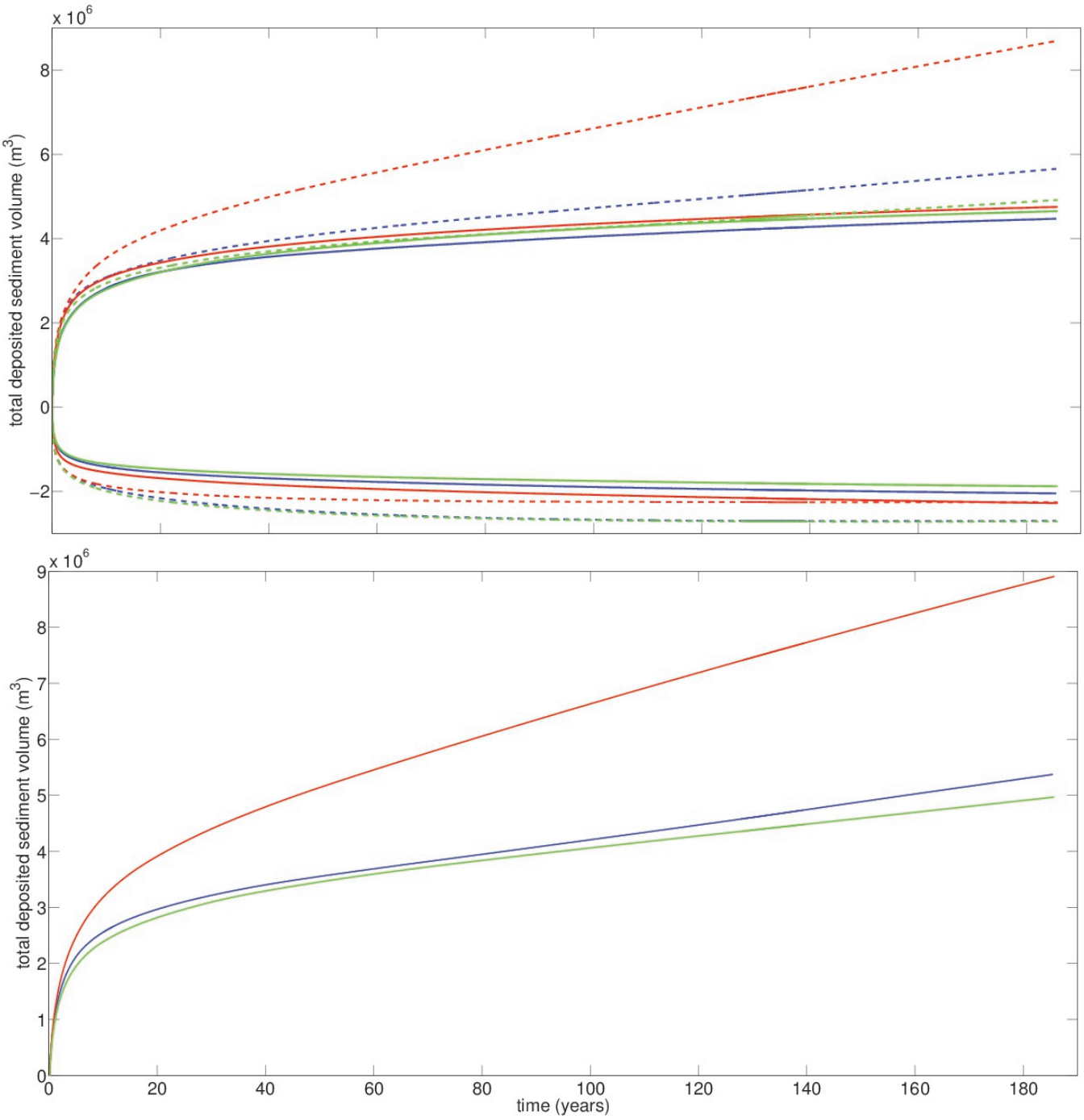

Figure 3.40: Total deposited sediment volume versus time in both inlets and sub-basins, for inlet spacing of 3 km (red), 6 km (blue) and 9 km (green).
Top panel: both inlets and sub-basins separately. The dashed lines indicate the updrift part and the solid lines the downdrift part. Both sub-basins are indicated by the positive values (deposited sediment), whereas the inlets are indicated the negative values (eroded sediment).
Bottom panel: total deposited sediment in inlets and basin together, versus time.

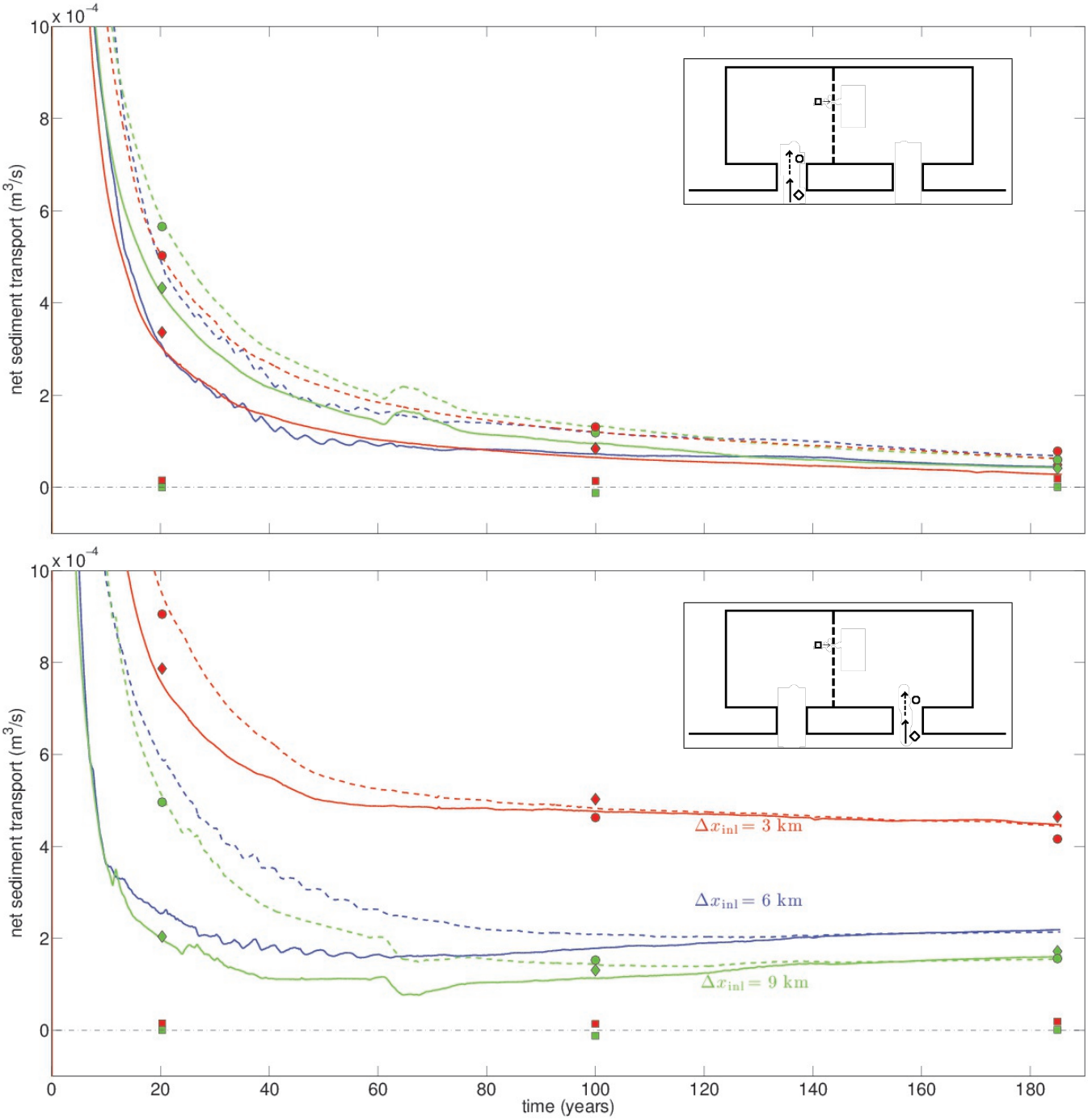

Figure 3.41: Volumetric sediment exchange rates between different parts of the domain (inlets and sub-basins), both for the downdrift sub-system (upper panel) and the updrift sub-system (lower panel). Red indicates a close distance between the inlets (3 km), blue the reference case (6 km) and green a large distance between the inlets (9 km). The symbols indicate net sediment transports from sea to inlet (diamonds) and from inlet to basin (circles) at some moments in time, determined directly from the model data (not shown here for the reference case, see fig. 3.23). Additionally, transports from downdrift to updrift basin are visualised by the green squares. The curves indicate volumetric sediment exchange rates from sea to inlet (solid) and from inlet to basin (dashed) calculated from the total deposited sediment volume (cf. eq. (2.28)). The transport between the two sub-basins is neglected here.

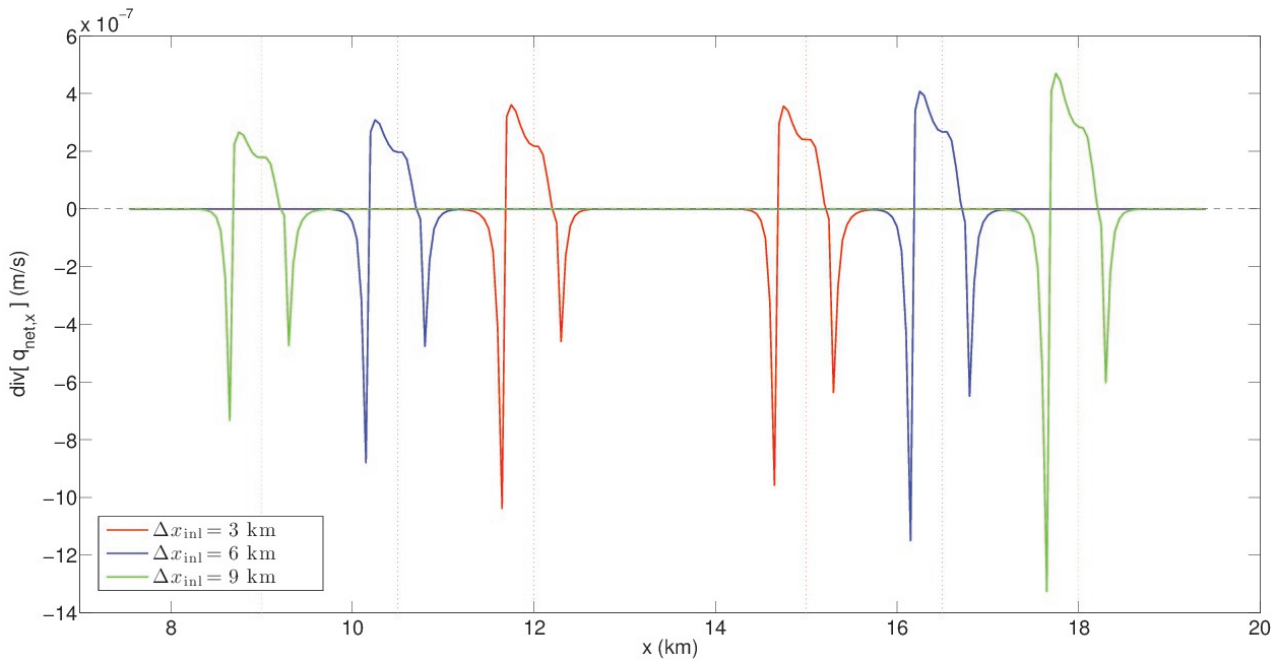

Figure 3.42: The divergence of the net longshore sediment transport averaged over the basin width, versus longshore distance x at the initial state. The distance between the inlets is indicated by the colour: red indicates 3 km, blue indicates 6 km and green indicates 9 km. The centres of the inlets are indicated by the coloured dotted lines.

3.3 Sudden lowering of the bed level

3.3.1 Morphology

To mimic the effect of a sudden lowering of the bottom due to extraction of e.g. gas from below the bed level, the bed level of the reference run (cf. § 3.1) is lowered after 185 yr of morphological evolution according to a Gaussian function in part of the domain. Three different cases are studied: a maximum lowering of 1 m in the updrift sub-basin ('1 m updrift'), a maximum lowering of 2 m in the updrift sub-basin ('2 m updrift'), and a maximum lowering of 1 m in the centre of the basin ('1 m centre'). Specifications of these different cases can be found in table 2.3 on page 13. In order to study the effect of both location and intensity of the imposed depression of the bed level on the morphological evolution, fig. 3.43 shows the morphological pattern directly after lowering (left column) and after 70 yr of adaptation (right column) for the three cases. From top to bottom, the cases '1 m updrift', '1 m centre' and '2 m updrift' are shown, with left the bed level directly after lowering ($t = 185$ yr) and right the bed level after 70 yr of morphological adaptation ($t = 255$ yr). To highlight the changes, fig. 3.44 shows for all three cases the difference in bed level compared to the reference run (at $t = 255$ yr, left column) and the changes that took place in the 70 yr of morphologic adaptation (right column). The peak of the Gaussian (indicating maximum lowering), is denoted by a cross in all panels of figs. 3.43 and 3.44. Additionally, the top right panel of fig. 3.44 contains the difference in bed level between $t = 185$ yr and $t = 255$ yr for the reference case.

It follows that for the downdrift sub-system, there are only minor adaptations during a period of 70 yr after the lowering of the bed level took place (right column of fig. 3.44). Compared to the reference case, the main difference in morphological evolution is a lack of bed level change around the centre of the Gaussian lowering and in the updrift part of the downdrift sub-basin.

The location of the lowering mainly has an effect on the changes in the updrift sub-basin. When the lowering takes place in the updrift sub-basin (second row of fig. 3.44), morphological changes are confined to the downdrift part of this sub-basin, whereas a lowering close to the watershed (third row of fig. 3.44) effects almost the whole updrift sub-basin. For the downdrift sub-basin, the main effect of the location of lowering on the morphological changes is that less morphological changes appear close to the watershed in case of lowering in the centre of the basin. The updrift inlet experiences in both cases more erosion than the reference case (left column of fig. 3.44), but in the case of lowering near the watershed, the downdrift part of the updrift inlet will also be subject to sedimentation.

Increasing the intensity of the imposed depression in the bed level (second and fourth row of fig. 3.44) has no significant effect on morphological changes in the downdrift sub-basin and inlet. Changes of the bed level in both nearshore sea and updrift sub-basin and inlet increase with an increased intensity of the imposed depression, especially larger erosion in the updrift inlet and larger sedimentation on the updrift ebb-tidal delta. However, an increased intensity of the imposed depression does not lead to different patterns.

It is especially striking that no significant morphological changes happen in the region where the most intense lowering of the bed takes place. To analyse this effect, fig. 3.45 shows the ration of bed shear stress over critical shear stress ($|\boldsymbol{\tau}_\mathrm{b}|/\tau_\mathrm{crit}$) for the reference case and the three cases of lowering, after 185 yr (directly after lowering of the bed). A decreased bed shear stress is observed in the region of lowering, which is caused by a decreased velocity magnitude (because

$\boldsymbol{\tau}_{\mathrm{b}}$ varies with the velocity only, cf. eq. (2.2)). Thus, it is concluded that the velocity decreases in the region of lowering. This is caused by continuity in eq. (2.1). The frictional part in eq. (2.1) cannot cause this effect, because the frictional term is inversely proportional to the local water depth.

3.3.2 Net sediment transport patterns

To find out whether an artificial lowering of the bed level results in a compensating import of sediment by the system, the net sediment transport patterns are shown in fig. 3.46, both directly after lowering ($t = 185$ yr, left column) and after 70 yr of morphological adaptation ($t = 255$ yr, right column). From top to bottom, reference case and the cases '1 m updrift', '1 m centre' and '2 m updrift' are shown. The main difference in net sediment transport between a lowering in the updrift sub-basin and the reference case is a lower transport in the case of lowering and a region of high net sediment transport at the landward boundary in the centre of the basin. The main difference in net sediment transport between a lowering in the centre of the basin and the reference case is a largely increased net transport from the inlet towards the watershed.

To investigate the net sediment transport patterns more closely, the same approach as in the previous sections is followed, namely by applying the simple transport formulation of eq. (2.28). Fig. 3.47 shows the obtained net transport patterns, both directly after lowering ($t = 185$ yr, left column) and after 70 yr of morphological adaptation ($t = 255$ yr, right column). Again, from top to bottom, reference case and the cases '1 m updrift', '1 m centre' and '2 m updrift' are shown. For a lowering in the updrift sub-basin (second and fourth row), no significant net transport occurs in the updrift part of the updrift sub-basin (compared to the reference case). For a lowering in the centre of the basin, no significant net transport occurs in the updrift part of the downdrift sub-basin (compared tot the reference case).

To further investigate these total patterns of the net sediment transport, the net sediment transport of fig. 3.47 is split in a part induced by the residual flow and a part induced by tidal asymmetry, visualised in figs. 3.48 and 3.49, respectively. First the part of the sediment transport due to the residual flow (fig. 3.48) is examined. For a lowering of the bed level in the updrift sub-basin (second and fourth row) the only significant change is a downdrift directed net transport at the landward boundary near the centre of the basin. In case of a lowering of the bed level in centre of the basin, the main net transport patterns are the same as in the reference case, except for an increased intensity of the transports. In all cases of lowering of the bed level, shoals in the reference case that are submerged due to the artificial lowering of the bed level do not experience significant net transport. For the sediment transport induced by tidal asymmetry (fig. 3.49), the main difference in net sediment transport pattern between a lowering of the bed level in the updrift sub-basin and the reference case, is a decreased sediment transport in the updrift part of the downdrift sub-basin. Furthermore, an updrift directed transport arises due to the lowering at the landward boundary near the centre of the basin. In case of a lowering in the centre of the basin, the main differences in net transport (compared to the reference case) are an increased updrift transport away from the watershed in the updrift sub-basin and a decreased sediment transport in the updrift part of the downdrift sub-basin.

To answer the question whether an artificial lowering of the bed level results in a compensating import of sediment by the system, figs. 3.48 and 3.49 are zoomed at the inlet areas. These zoomed vector fields are shown in fig. 3.50 for the net sediment transport induced by the

residual flow and in fig. 3.51 for the net sediment transport induced by tidal asymmetry, both after 255 yr. In both figures, the left column corresponds to the downdrift inlet and the right column to the updrift inlet. From top to bottom, reference case and the cases '1 m updrift', '1 m centre' and '2 m updrift' are shown. For the net sediment transport induced by the residual flow (fig. 3.51), no significant differences are found between the different cases and the reference case. However, for the net sediment transport induced by tidal asymmetry, in all three cases a decrease of the sediment import at the landward side of the updrift basin is observed. This decrease is stronger for a lowering in the updrift sub-basin than for a lowering in the centre of the basin. Furthermore, an increase of the sediment export at the updrift side of the updrift basin is observed (compared to the reference case), which is strongest for a lowering of 2 m in the updrift sub-basin and weakest in case of a lowering of 1 m at the centre of the basin.

To quantify the effect of the location of the imposed depression of the bed level on the import or export of sediment by the system, the upper panel of fig. 3.52 shows the evolution of the total deposited sediment volume compared to $t = 185$ yr (directly after lowering of the bottom) for the reference case (blue), a lowering of maximum 1 m in the updrift sub-basin (red) and a lowering of maximum 1 m in the centre of the basin (green). The downdrift (updrift) sub-system is indicated by solid (dashed) curves. Positive values indicate the sub-basins (deposited sediment), and negative values indicate the inlets (erosion of sediment). So, three groups of three curves can be identified, from top to bottom: updrift sub-basin, downdrift sub-basin, downdrift inlet and updrift inlet. For the updrift sub-basin, there is almost no difference in deposited sediment volume between a lowering in the centre of the basin and the reference run, although the former is slightly larger. However, a lowering at the centre of the basin results in a decreased volume of deposited sediment. For the updrift inlet, both a lowering of the bed level at the centre of the basin and a lowering in the updrift sub-basin result in an increased volume of eroded sediment compared to the reference case. For the downdrift sub-basin, lowering of the bed level at either location results in a decreased volume of deposited sediment compared to the reference case, with a slightly larger decrease for lowering at the centre of the basin. For the downdrift inlet, both a lowering of the bed level at the centre of the basin and a lowering in the updrift sub-basin result in a decreased volume of eroded sediment compared to the reference case.

The middle panel of fig. 3.52 is comparable to the upper panel, but for the effect of the intensity of the imposed depression of the bed level. Here the evolution of the total deposited sediment volume (compared to $t = 185$ yr) for the reference case (blue) is shown, together with the same quantity for a lowering of maximum 1 m in the updrift sub-basin (red) and a lowering of maximum 2 m in the updrift sub-basin (cyan). For the updrift sub-basin, there is no difference in deposited sediment volume between a lowering of maximum 1 m or 2 m in the updrift sub-basin. However, for the updrift inlet, an increased intensity of the imposed depression of the bed level results in an increased volume of eroded sediment. For the downdrift sub-basin, the total deposited sediment volume decreases with increasing intensity of the imposed depression of the bed level. For the downdrift inlet, the total eroded sediment volume decreases with increasing intensity of the lowering, although the difference in total eroded sediment volume between a lowering of 1 m and 2 m is small.

Finally, the bottom panel of fig. 3.52 shows the total deposited sediment volume (compared to $t = 185$ yr) in the total of inlets and basin for all three cases and the reference case, with the choice of colours the same as in the upper and middle panel. For all cases of lowering the bed level, this is not compensated by an import of sediment in the basin, but even enhanced by an

export of sediment compared tot the reference case. From this panel it is also concluded that both location and intensity of lowering of the bed level have a significant influence on the total imported sediment. Note that, compared to the reference case, the difference in total deposited sediment in basin and inlets together is mainly caused by an increased erosion of the updrift inlet, which is (cf. fig. 3.51) mainly caused by tidal asymmetry. This increased erosion of the updrift inlet is also the main cause for the effect of the intensity of the lowering of the bed level on the total deposited sediment volume. The effect of the location of the lowering on the total deposited sediment volume, however, is mainly caused by a difference in sedimentation of the updrift sub-basin between a lowering in the centre of the basin and a lowering in the updrift sub-basin.

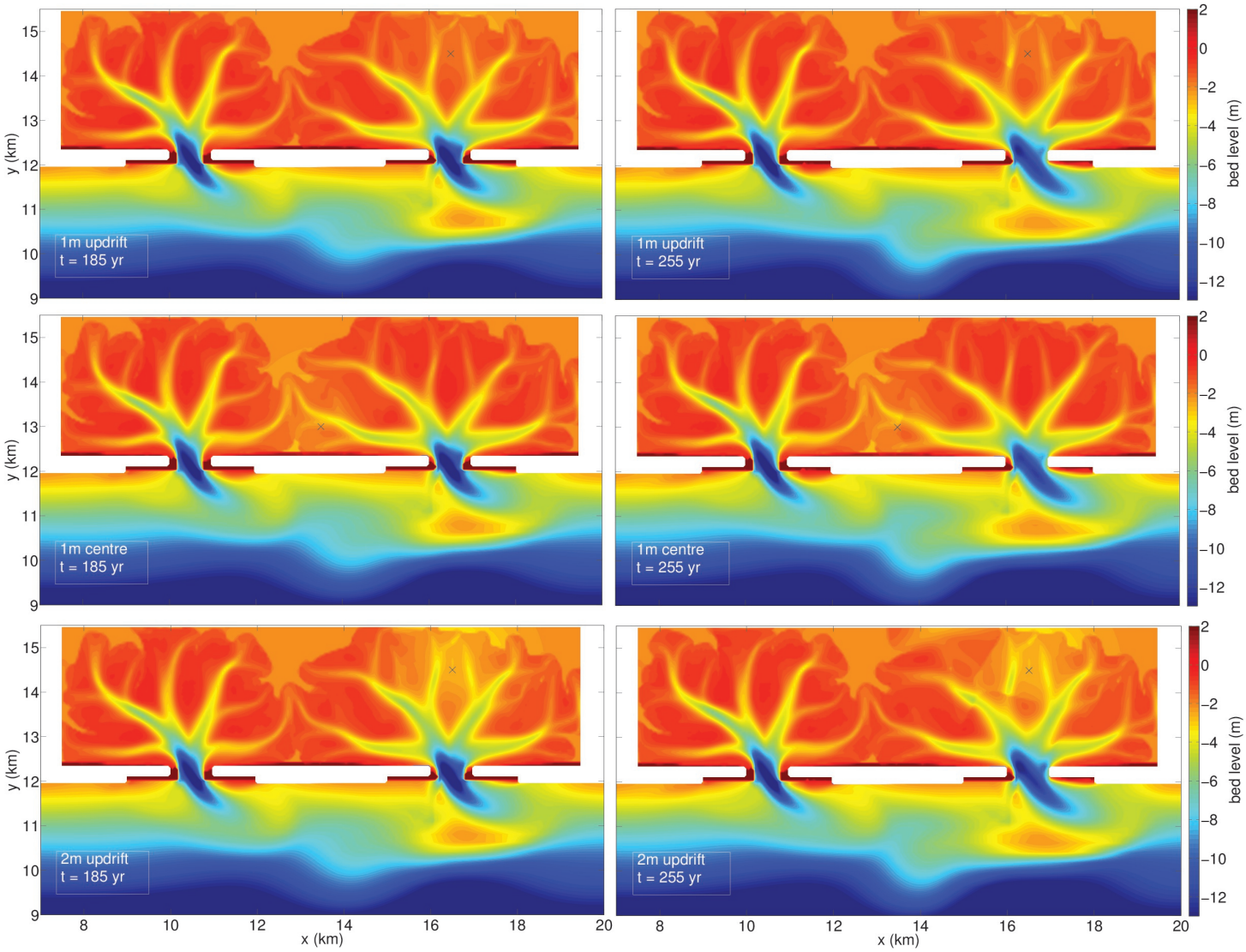

Figure 3.43: Colour plots of the bed level after lowering of the bottom for the three different cases, with 0 representing mean water level at sea. Left: the bed level directly after lowering the bottom. Right: the bed level after 70 yr of morphologic adaptation. In each panel, the black cross indicates the point of most intense lowering of the bottom (centre of the Gaussian).

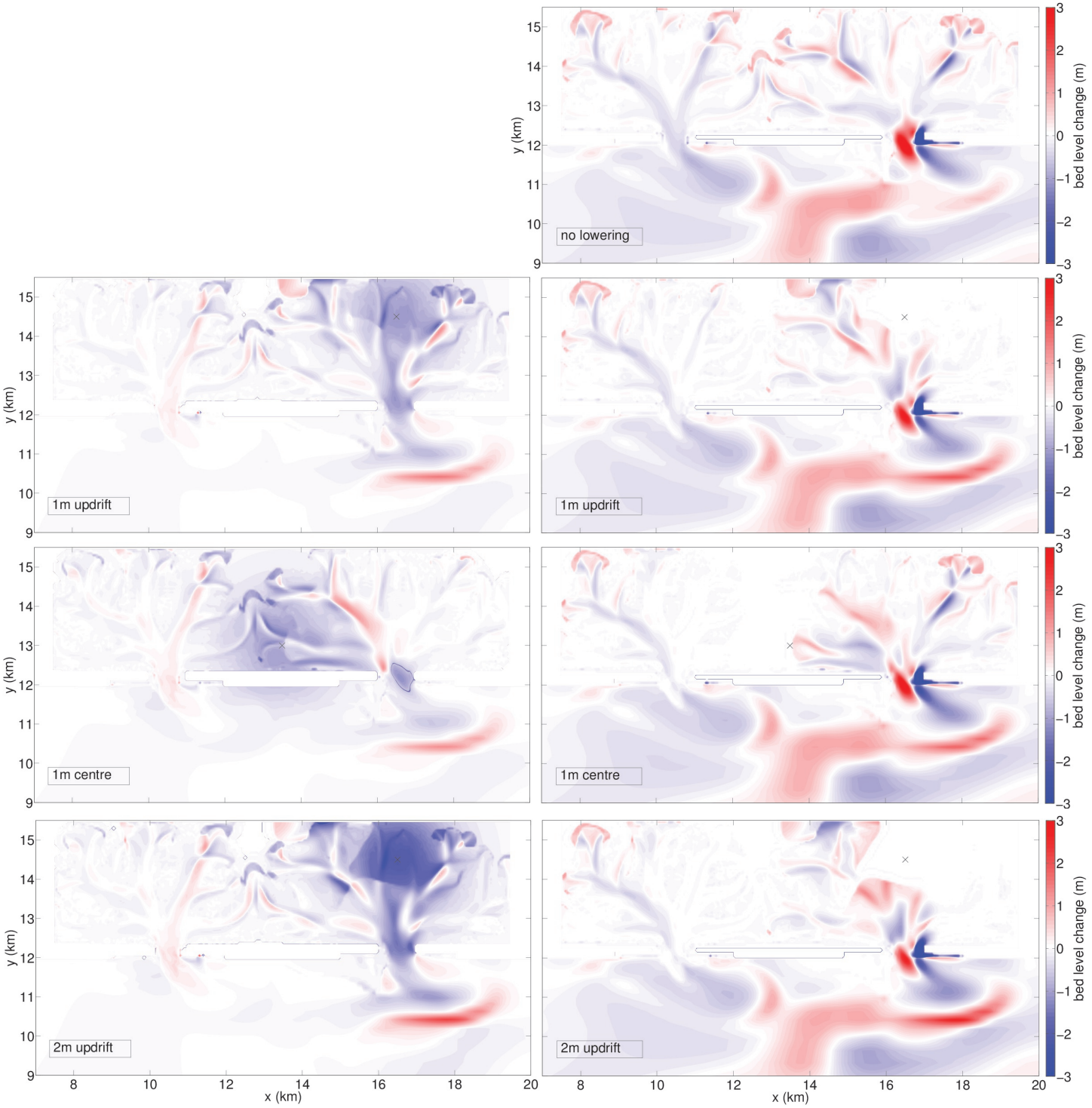

Figure 3.44: Left: colour plots of the difference in bed level between the case with lowered bottom (after 70 yr of morphologic adaptation) and the reference case at the same time ($t = 255$ yr). Red indicates levels higher and blue lower than the reference case at the same time.
Right: colour plots of the change in bed level after 70 yr of morphologic adaptation after lowering of the bottom (change between $t = 185$ yr and $t = 255$ yr). The reference case (no lowering) is shown, accompanied by the three different cases of lowering. Red indicates levels higher and blue lower than the elevation directly after lowering.
In each panel, the black cross indicates the point of most intense lowering of the bed (centre of the Gaussian).

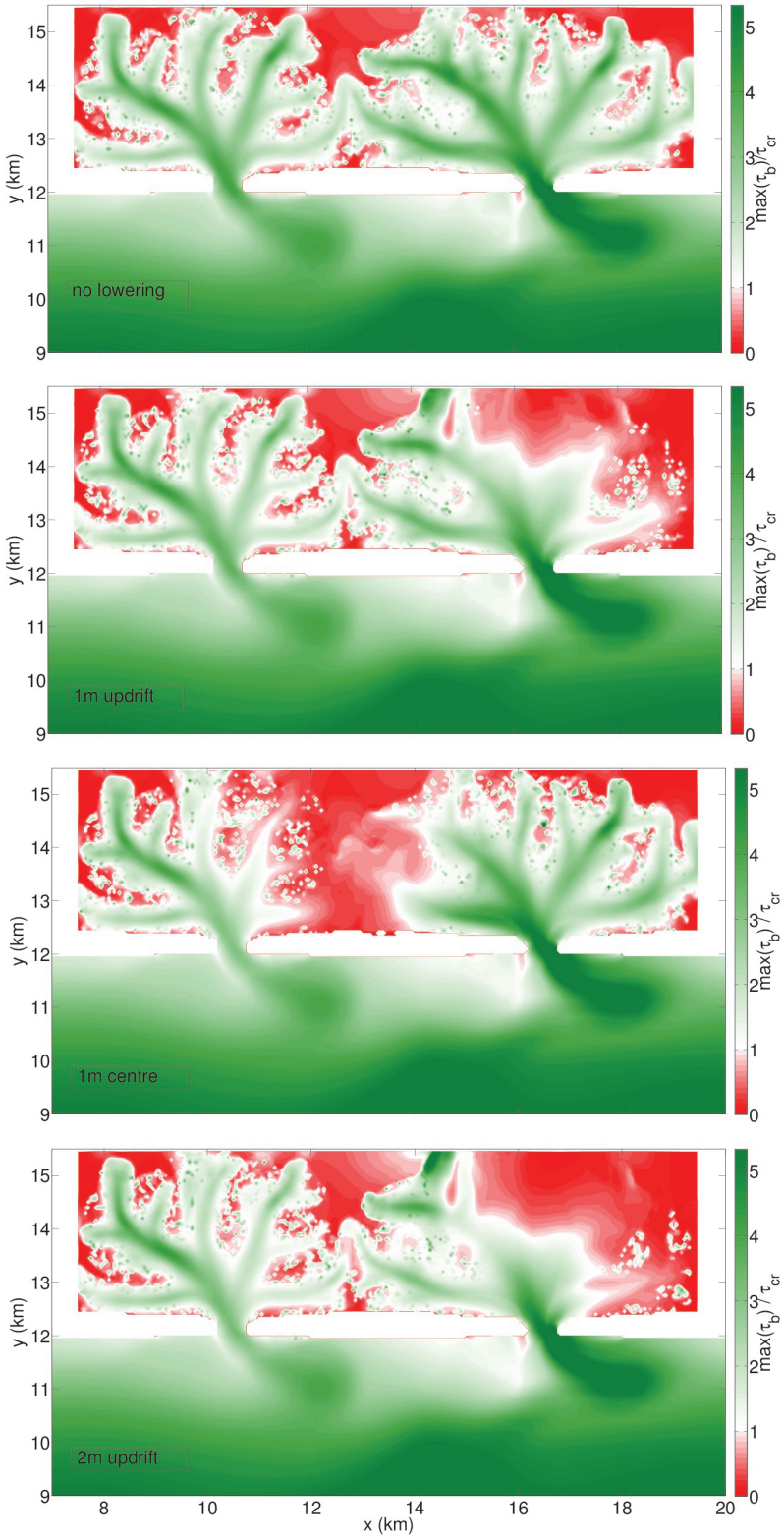

Figure 3.45: Ratio of bed shear stress (cf. eq. (2.2)) over critical shear stress (cf. eq. (2.13)) in the domain after 185 yr (directly after lowering of the bed). From top to bottom, the reference case, 1 m lowering in the updrift sub-basin, 1 m in the centre and 2 m in the updrift sub-basin are shown.

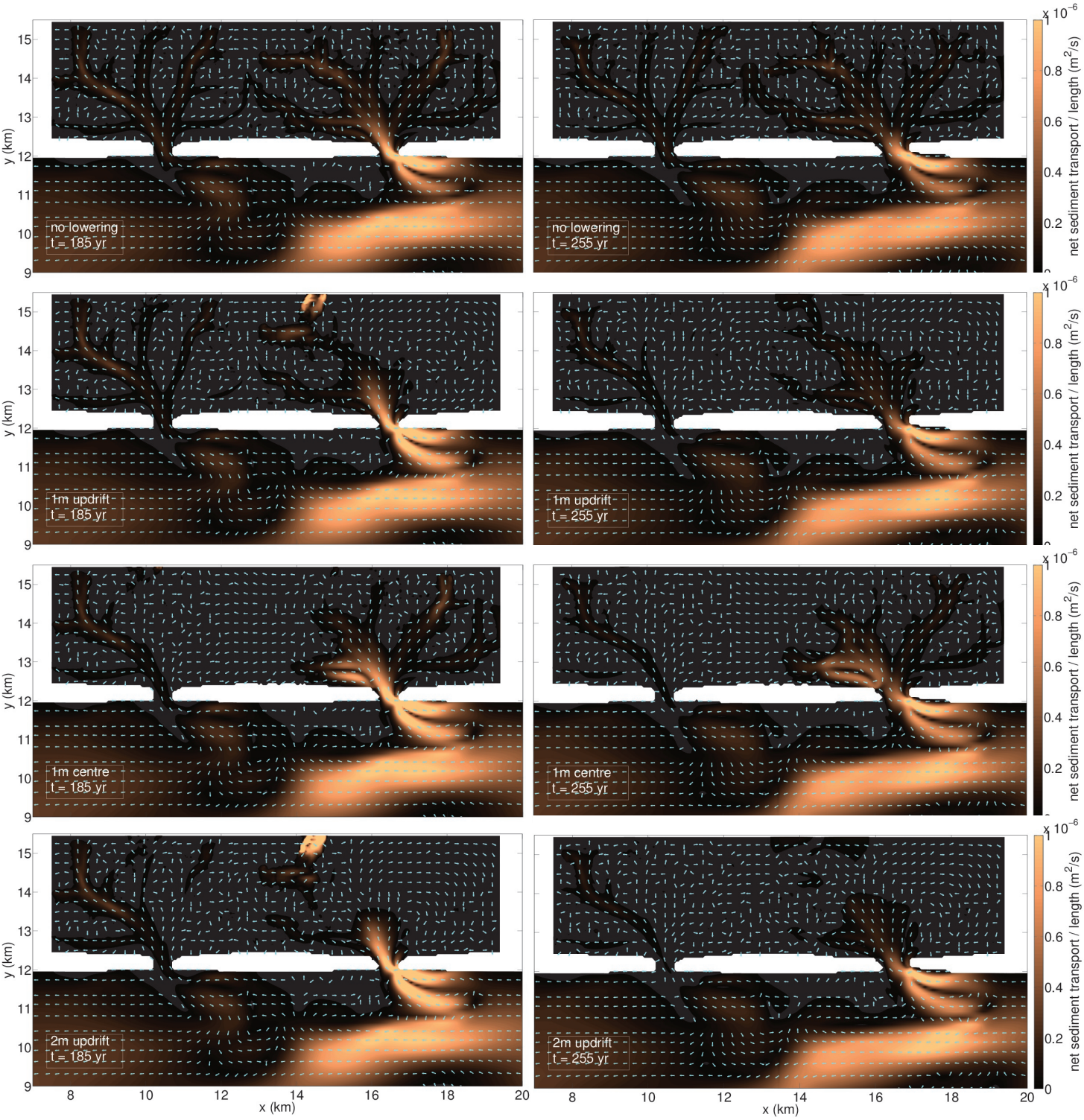

Figure 3.46: Vector field of the net sediment transport per unit length at $t = 185\,\mathrm{yr}$ (left column) and at $t = 185\,\mathrm{yr}$ (right column). From top to bottom, the rows show an increasing distance between the inlets. In order to even visualise the direction of small transports, all vectors have equal length. The magnitude of the transport is indicated by the colours.

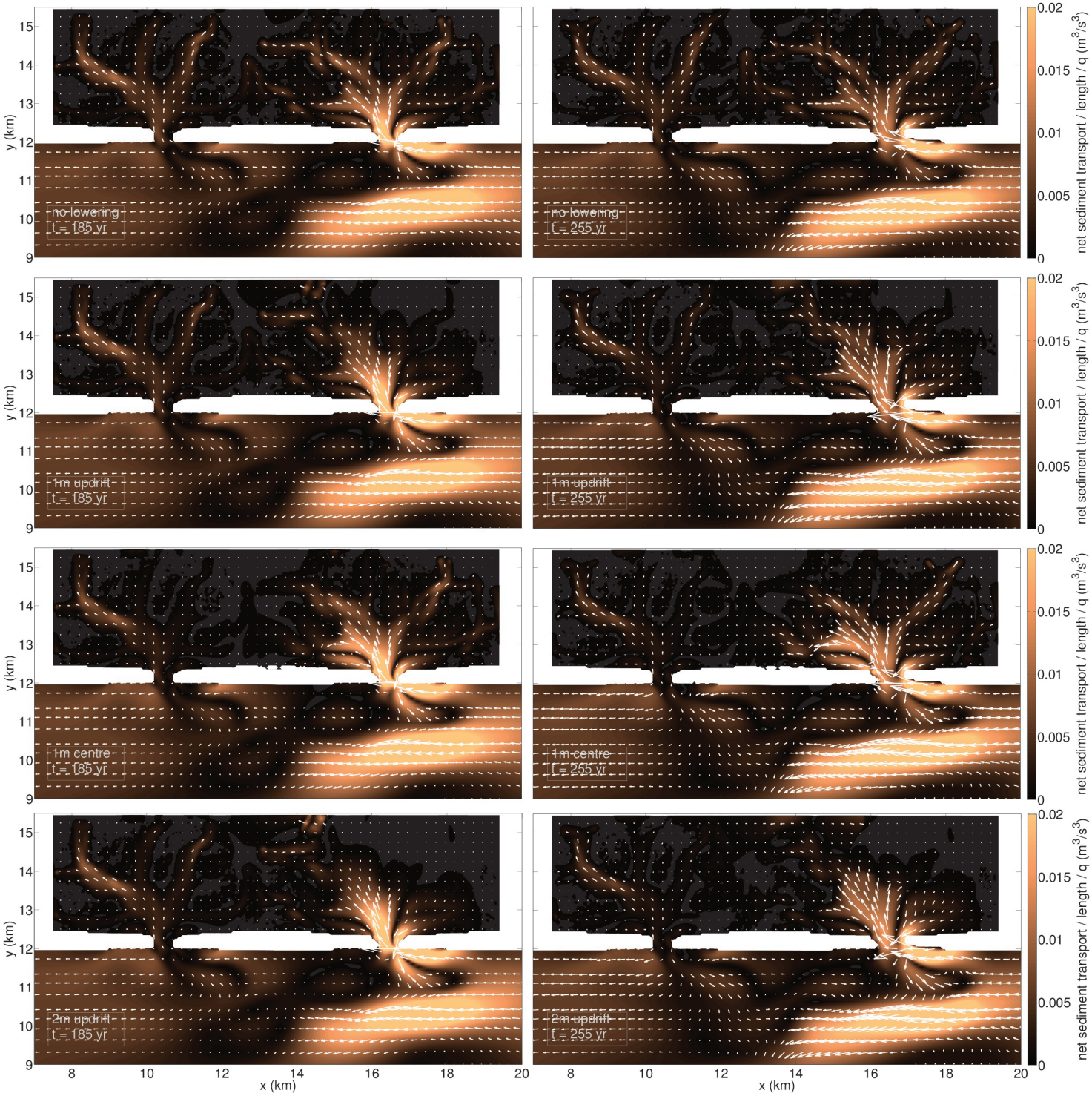

Figure 3.47: Vector field of the net sediment transport (divided by a constant $\hat{q}$, see § 2.2.4) as parameterised by eq. (2.31). Colours highlight the magnitude of the sediment transport.
Left column: $t = 185$ yr. Right column: $t = 255$ yr. The configuration is the same as in fig. 3.46, so the top row shows the reference case, the second row shows lowering of maximum 1 m in the updrift basin, the third row lowering near the watershed, and the bottom row lowering of maximum 2 m in the updrift basin.

Figure 3.48: Vector field of the net sediment transport (divided by a constant $\hat{q}$, see § 2.2.4) due to joint action of residual and M2 tidal velocities, as parameterised by eq. (2.31). Colours highlight the magnitude of the sediment transport.
Left column: $t = 185\,\mathrm{yr}$. Right column: $t = 255\,\mathrm{yr}$. The configuration is the same as in fig. 3.46, so the top row shows the reference case, the second row shows lowering of maximum 1 m in the updrift basin, the third row lowering near the watershed, and the bottom row lowering of maximum 2 m in the updrift basin. Grid cells that are partly submerged during a tidal cycle are excluded.

Figure 3.49: Vector field of the net sediment transport (divided by a constant $\hat{q}$, see § 2.2.4) due to joint action of M2 and M4 tidal velocities (tidal asymmetry), as parameterised by eq. (2.31). Colours highlight the magnitude of the sediment transport.
Left column: $t = 185$ yr. Right column: $t = 255$ yr. The configuration is the same as in fig. 3.46, so the top row shows the reference case, the second row shows lowering of maximum 1 m in the updrift basin, the third row lowering near the watershed, and the bottom row lowering of maximum 2 m in the updrift basin. Grid cells that are partly submerged during a tidal cycle are excluded.

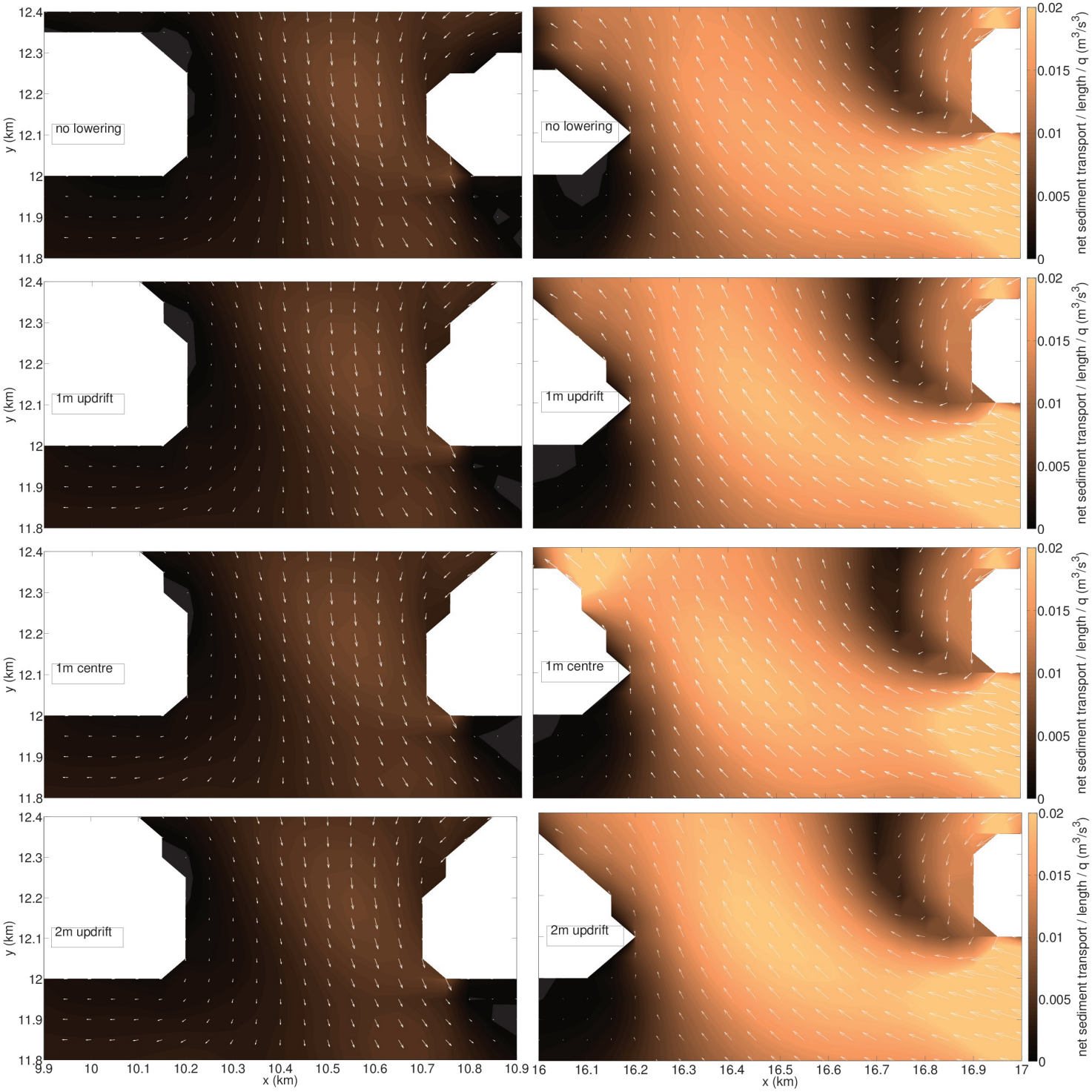

Figure 3.50: Vector field of the net sediment transport (divided by a constant $\hat{q}$, see § 2.2.4) due to joint action of residual and M2 tidal velocities, as parameterised by eq. (2.31) at $t = 255\,\mathrm{yr}$. Colours highlight the magnitude of the sediment transport.
Left column: downdrift inlet. Right column: updrift inlet. The configuration is the same as in fig. 3.46, so the top row shows the reference case, the second row shows lowering of maximum 1 m in the updrift basin, the third row lowering near the watershed, and the bottom row lowering of maximum 2 m in the updrift basin. Grid cells that are partly submerged during a tidal cycle are excluded.

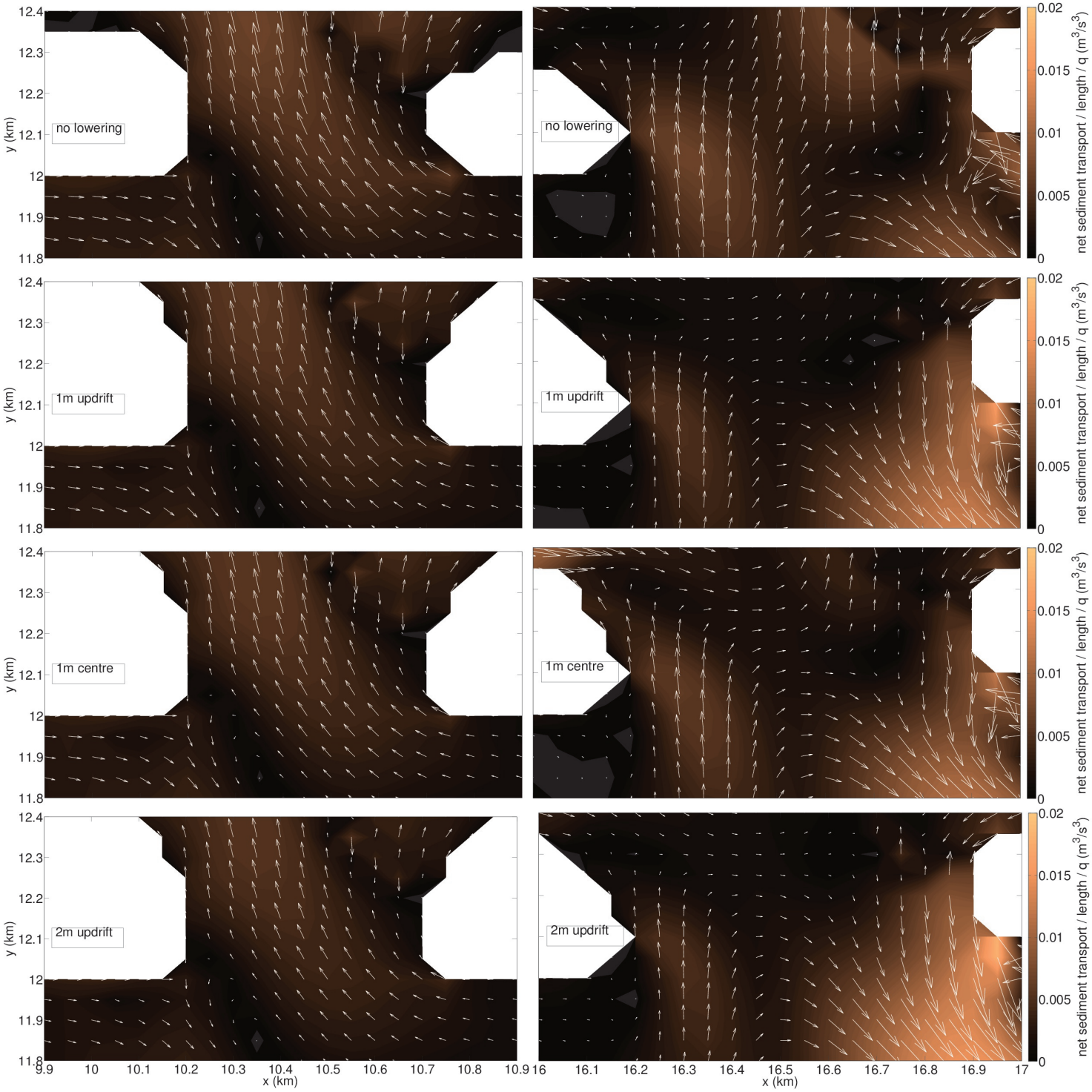

Figure 3.51: Vector field of the net sediment transport (divided by a constant $\hat{q}$, see § 2.2.4) due to joint action of M2 and M4 tidal velocities, as parameterised by eq. (2.31) at $t = 255\,\mathrm{yr}$. Colours highlight the magnitude of the sediment transport.
Left column: downdrift inlet. Right column: updrift inlet. The configuration is the same as in fig. 3.46, so the top row shows the reference case, the second row shows lowering of maximum 1 m in the updrift basin, the third row lowering near the watershed, and the bottom row lowering of maximum 2 m in the updrift basin. Grid cells that are partly submerged during a tidal cycle are excluded.

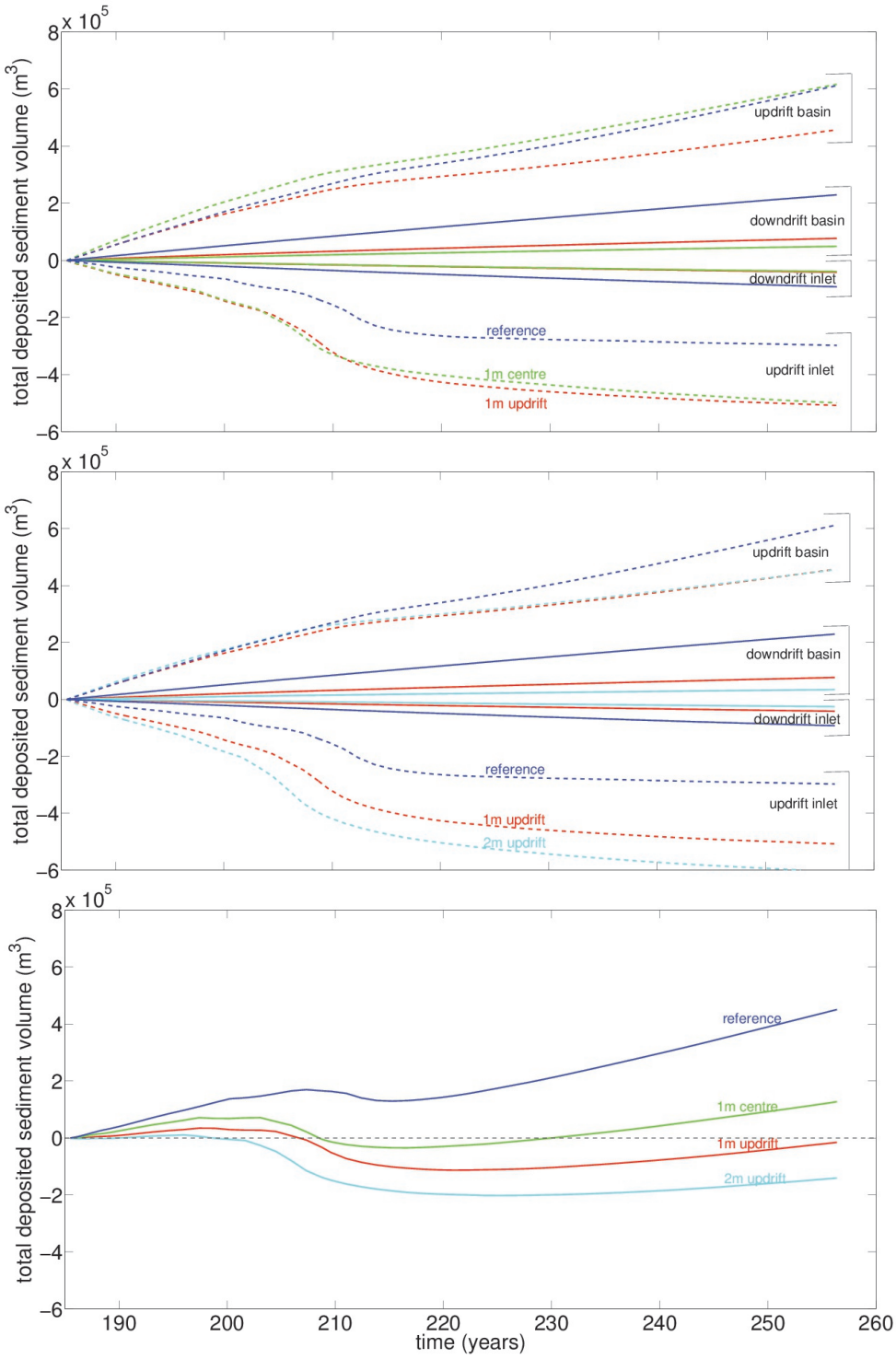

Figure 3.52: Total deposited sediment volume versus time in both inlets and sub-basins, after the bottom is lowered in part of the domain. The dashed lines indicate the updrift part and the solid lines the downdrift part.
Upper panel: the effect of the location of lowering on the deposition and erosion in time. Middle panel: the effect of the intensity of lowering on the deposition and erosion in time. Bottom panel: Total deposition of sediment in basin and inlets together, versus time.
In all panels, blue indicates the reference case, cyan indicates a lowering of maximum 2 m in the updrift sub-basin, red indicates a lowering of maximum 1 m in the updrift sub-basin and green indicates a lowering of maximum 1 m in the centre of the basin.

4. Discussion

In this chapter, the results of chapter 3 are compared to measurements and theoretical concepts in literature. Furthermore, the analytical model of Ridderinkhof [1988] and Buijsman & Ridderinkhof [2007] is used to gain more insight. For details on this model, see appendix A. Special attention goes to the continuous net import of sediment and the location and intensity of the tidal watershed. Also comparison with measurements of the inlets at the updrift and the downdrift side of the East Frisian Wadden island of Baltrum (Wichter Ee and Accumer Ee, respectively) deserves special attention, as the dimensions of the numerical model domain are based on this system.

Afterwards, the additional value of this numerical model study to the present state of knowledge will be briefly discussed. Finally, both the assumptions in the physical model and the numerical implementation of it will be discussed.

4.1 Comparison with present state of knowledge

4.1.1 Measurement results from literature

As shown in figs. 3.2 and 3.3, in each inlet a main channel develops during the morphological evolution, which extends in the downdrift direction into the basin. These channels branch into a complex network of small channels in the basin (cf. fig. 3.3). The channel-shoal patterns resulting from the model runs used in this thesis, show the 'apple tree' like behaviour as described by Van Veen [1950]. Moreover, the downdrift orientation of the main channels is in accordance with the patterns observed in the East Frisian Wadden Sea (see e.g. Stanev et al. [2007]), although the downdrift tilting is less pronounced in the results of the numerical model. This may be caused by the dominant wind direction being from the west in the Dutch and East Frisian Wadden Sea. Furthermore, the channel direction in the numerical model is also influenced by the cross-shore boundaries of the basin, which are impermeable. In the Wadden Sea, these boundaries are replaced by tidal watersheds and (especially for the updrift sub-basin of Baltrum), farther away from the inlet.

Besides the tilting of the channels in the basin, also a branching pattern is observed, of typically two to three times branching. Cleveringa & Oost [1999] described a typical three to four times branching in the Wadden Sea, with a scale not smaller than 500 m. Although the four times branching is not reached in the present research, this could be caused by the rather small dimensions compared to most Wadden Sea sub-basin. As for the fraction of the basin area covered by shoals, this is reported by Niemeyer [1994] to be 88% and 75% for the Wichter Ee and Accumer Ee, respectively, and by Elias et al. [2012] to be in the Dutch Wadden Sea

50% and 70% for the Ameland and Frisian inlets, respectively. This is all significantly larger than the results of the numerical model reveal (almost 45% after 185 yr, cf. 3.21). However, after 185 yr an increasing trend is still observed and import of sediment is still ongoing.

For the watershed, a downdrift shift is observed compared to the geometrical centre of the basin, caused by a phase difference between the two inlets. This downdrift shift is in agreement with what is observed for the watershed locations in the East Frisian Wadden Sea [Stanev et al., 2003].

The tidal prism that is observed in the inlets surrounding the Wadden island of Baltrum, reported by Niemeyer [1994] and Flöser et al. [2011] are compared to the results of the numerical model (see table 4.1). The differences are large, but this is mainly caused by difference in the area of the back barrier basin of each sub-system between numerical model and measurements (see table 4.1). Because the tidal prism is in first order estimate $P \sim A \times$ tidal range, correcting for the large differences in back barrier basin area leads to similar results for the numerical model and the measurements.

	Delft3D	Niemeyer [1994]	Flöser et al. [2011]
P_{down}	$3.2 \times 10^7\,\text{m}^3$	$15.8 \times 10^7\,\text{m}^3$	$19 \times 10^7\,\text{m}^3$
P_{up}	$4.3 \times 10^7\,\text{m}^3$	$3.1 \times 10^7\,\text{m}^3$	
A_{down}	$15.8\,\text{km}^2$	$101.5\,\text{km}^2$	$90\,\text{km}^2$
A_{up}	$20.2\,\text{km}^2$	$23.1\,\text{km}^2$	

Table 4.1: Comparison of tidal prism (P) and basin area (A) between the numerical model (after 185 yr) and two studies that mention results from measurements in the inlets surrounding Baltrum, both for the downdrift (subscript 'down') and the updrift (subscript 'up') sub-system.

4.1.2 Theoretical concepts and theories

In the nearshore sea, two main channels exist (cf. fig. 3.12), of which one is ebb dominant and one is flood dominant in terms of water flow. The ebb channel is directed mainly in the cross-shore direction and the flood channel mainly in the longshore direction. In agreement with the idealised tidal inlet system described by De Swart & Zimmerman [2009] (cf. fig. 1.1), water flows in the cross-shore direction during the ebb phase of the tidal cycle, mainly in a free turbulent jet. Yet during the flood phase of the tidal cycle, a more radial inflow pattern occurs. These two phenomena result in a tidal residual circulation cell in the nearshore sea (with cross-shore flow out of the inlet and longshore flow into the inlet). According to Sha [1989b] and Sha & Van den Berg [1993], the cross-shore ebb-channel is tilted in the updrift direction in the nearshore sea when a small phase difference (much smaller than 90°) in tidal velocity is observed between shore-parallel tidal currents in the nearshore sea and cross-shore tidal currents in the inlet. This tilting of the ebb-channel is indeed observed in the results of this study (cf. fig. 3.12), along with a phase difference between the M2 tidal ellipse in the inlet and the M2 tidal ellipse in the nearshore sea that is significantly smaller than 90°. This phase difference is visualised in fig. 4.1 for both inlets versus time, where an increasing phase difference between sea and inlet M2 tidal current ellipses indicates a decreasing time lag between maximum currents in the inlets and in the sea.

Furthermore, Sha [1989a] proposes that cross-shore tidal currents (in and near the inlets) and longshore tidal currents (in the nearshore sea) interact at the seaward side of tidal inlets.

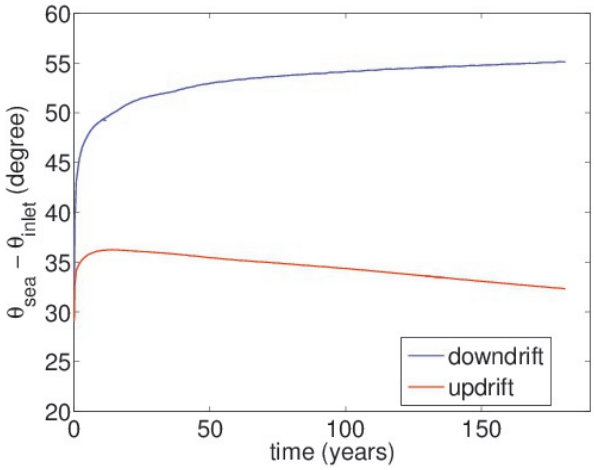

Figure 4.1: The phase difference (in degree) of the M2 tidal current ellipse between the nearshore sea (2 km offshore) and the inlets versus time. For the downdrift (updrift) sub-system the phase difference is visualised by the blue (red) curve.

As a result, a more or less circular flow pattern exists at the downdrift side of each inlet. Along with this, a unidirectional flow exists at the updrift side of each inlet, resulting from the enhancement of the longshore flow by the inlet tidal currents. These circular and unidirectional flow patterns at the updrift and downdrift side of each inlet, respectively, are visible in the tidal ellipses by large (small) values of the eccentricity at the downdrift (updrift) side of each inlet. This is also the case for the M2 tidal component in the results of this study (cf. bottom panels of fig. 3.7), and to a lesser degree also for the M4 component (cf. bottom panels of fig. 3.8).

Remarkable in the present research is the continuous import of sediment into the back-barrier basin by both inlets, which has a decreasing magnitude (cf. e.g. fig. 3.23). It was pointed out earlier that the import of sediment into the updrift sub-basin is mainly a result of the residual flow and the import of sediment in the downdrift sub-basin is mainly a result of tidal asymmetry (cf. fig. 3.16). Lincoln & Fitzgerald [1988] studied five flood-dominant (in terms of water) small tidal inlets along the southern coast of Maine (USA). They discuss that on of the reasons for flood-dominance is harmonic overtide growth due to frictional nonlinearities. In the present research, net sediment import is a result of tidal asymmetry in both inlets. However, for the updrift inlet, the residual flow (which is directed into the basin) causes flood currents to exceed ebb currents, which effect is largely dominant over tidal asymmetry. Thus, the residual flow turns out to be important for flood dominant behaviour in one inlet of a double-inlet tidal system. Furthermore, Ridderinkhof et al. [2014b] mention that, (building on earlier work of Friedrichs & Aubrey [1988] for short basins) flood dominance occurs for a phase difference between M2 and M4 tidal current ellipses of $-90° < 2\theta_{\mathrm{M2}} - \theta_{\mathrm{M4}} < 90°$. Moreover, Friedrichs & Aubrey [1988] already denoted that (for short basins) $2\phi_{\mathrm{M2}} - \phi_{\mathrm{M4}} \longrightarrow 90°$ (phase of sea level) and $2\theta_{\mathrm{M2}} - \theta_{\mathrm{M4}} \longrightarrow 360°$ (phase of the tidal current) in the centre of the inlet for a perfectly asymmetric situation. These properties are indeed observed for the downdrift inlet in the present research (cf. fig. 3.17). However, the updrift inlet turns out to behave exactly the opposite, which again indicates that tidal asymmetry is not the main cause for flood dominance in the updrift sub-system.

Note that an import of sediment is needed for the tidal inlet system to keep up with sea

level rise. When the import of sediment is too low for the bed level to keep up with sea level rise, shoals will drown and the system will be pushed increasingly farther away from a state of dynamic morphological equilibrium [Van Goor et al., 2003]. The total mean bed level rise in the basin (calculated from e.g. the slope of the dash-dotted black line in fig. 3.20, divided by the basin area) is approximately 0.35 mm/yr in the numerical model. This is still way below the rate of sea level rise, which was according to the IPCC [Rhein et al., 2013] globally very likely 3.2 mm/yr between 1993 and 2010.

Typical values of maximum velocities in the tidal inlets lie around 0.6 m/s (see fig. 4.2 for maximum velocities in the inlets versus time), which is much smaller than the typical value of 1 m/s that is generally applied for the O'Brien relation in the literature [O'Brien, 1966; Stive & Rakhorst, 2008]. The O'Brien relation $A_c = aP^m$ gives an approximate relation between tidal prism P and inlet cross-sectional area A_c, assuming the velocity amplitude U in the inlet to be constant (because $P \sim UA_c/\omega$).

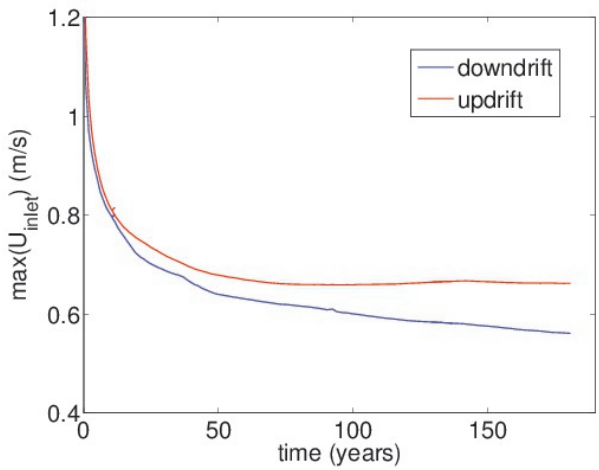

Figure 4.2: Maximum velocity (in m/s) observed during a tidal cycle in the inlet, versus time. The downdrift (updrift) inlet is represented by the blue (red) curve.

Following O'Brien [1966], the cross-sectional area A_c of the inlets is plotted against the tidal prism P from the numerical model (after 185 yr) in the right panel of fig. 4.3, with the downdrift (updrift) inlet denoted by the blue (red) dot. Green dots indicate inlets in the Wadden Sea and the black dots are tidal inlets elsewhere in the world. The solid black line shows the O'Brien relation $A_c = aP^m$, with coefficients $a = 7.0 \times 10^{-5}\,\mathrm{m}^{-1}$ and $m = 1$ as found by Eysink [1990] for the Dutch Wadden Sea. Note, however, that similar values are found for different regions of the Wadden Sea [Stive & Rakhorst, 2008]. As from table 4.1, it can be concluded from the right panel of fig. 4.3 that the tidal prism of both inlets in the numerical model corresponds quite well with the prism for Wichter Ee (indicated by the green dot at $P \approx 4{\times}10^7\,\mathrm{m}^3$ and $A_c = 3{\times}10^3\,\mathrm{m}^2$). However, the inlet cross-sectional area in the numerical model results is larger than observed in Wichter Ee. Although the tidal prism depends linearly on the inlet cross-sectional area A_c as $P \sim UA_c/\omega$, this effect is counteracted by the lower velocity amplitude U (cf. fig. 4.2).

In the left panel of fig. 4.3, the inlet cross-sectional area obtained from the numerical model is plotted against tidal prism for different times, viz. initial case (cyan), $t = 20$ yr (green), $t = 50$ yr (red), $t = 100$ yr (blue) and $t = 185$ yr, with the downdrift (updrift) inlet denoted by the circles (squares) and the total of the two inlets by the crosses. The line shows the O'Brien relationship

$A_c = aP^m$, with coefficients $a = 7.0 \times 10^{-5}\,\mathrm{m}^{-1}$ and $m = 1$ as found by Eysink [1990]. This panel shows that the inlet cross-sectional area increases during the whole morphodynamic evolution of the system (cyan to black). This increase in cross-sectional area is explained by the lack of a sedimentation mechanism in the inlet in the model. According to $P \sim UA_c/\omega$ this is linked to a decrease of the tidal prism in time, which is especially observed in the updrift inlet (squares in left panel of fig. 4.3). The decrease in tidal prism after 50 yr (red to black) is dominated by another mechanism. According the downdrift basin this is most probably the decrease in velocity amplitude (cf. blue curve in fig. 4.2). For the updrift inlet (where the inlet velocity amplitude is approximately constant after 50 yr), still another mechanism is needed. This could be the development of shoals that fall dry during part of the tidal cycle, causing the effective basin area to be smaller at low tide (compared to the basin area at high tide). Note that already initially the tidal prism of the updrift basin (cyan squares) is larger than that of the downdrift basin (cyan circles). This is a result of the phase difference between the M2 tidal wave in the updrift and the downdrift inlet. Furthermore, it should be noticed that the proportionality constant a in the O'Brien relation $A_c = aP^m$ (given $m = 1$, with A_c cross-sectional area and P tidal prism) meeting the model results after 185 yr, is approximately three times the value found by Eysink [1990]. Yet, this is no surprise because the inlet velocity is much smaller than 1 m/s.

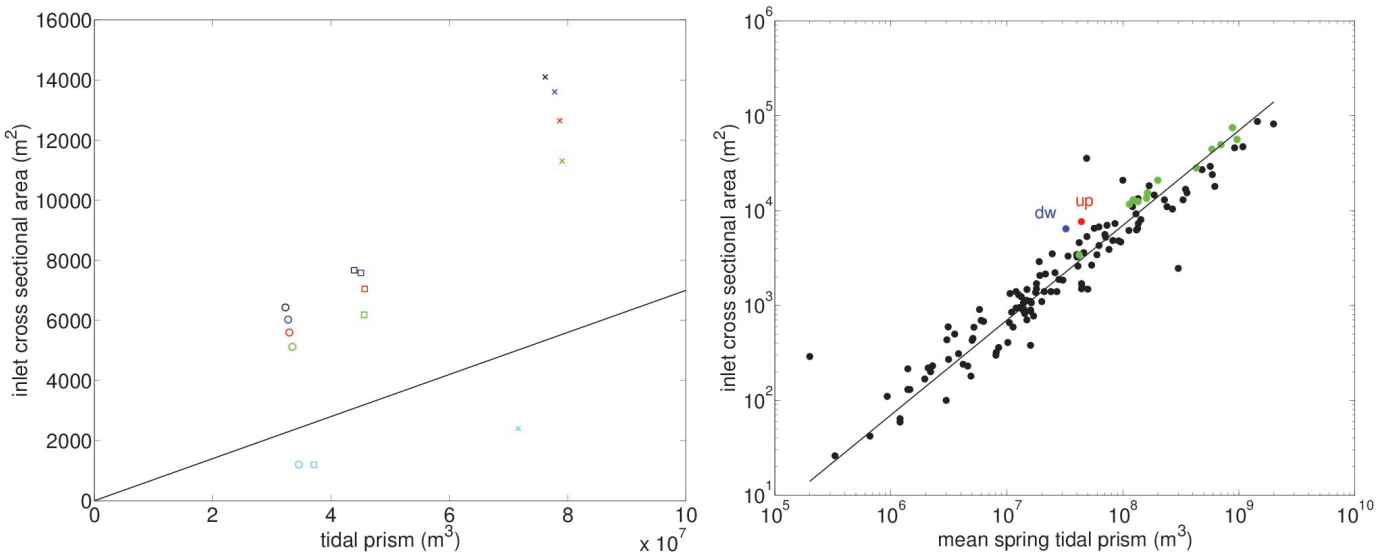

Figure 4.3: Left: change of inlet cross-sectional area and tidal prism in time, both for the downdrift inlet (circles), the updrift inlet (squares) and the total of two inlets (crosses) at five times, viz. initial case (cyan), $t = 20$ yr (green), $t = 50$ yr (red), $t = 100$ yr (blue) and $t = 185$ yr (black). The line indicates the O'Brien relationship $A_c = aP^m$ with coefficients $a = 7.0 \times 10^{-5}\,\mathrm{m}^{-1}$ and $m = 1$, as found by Eysink [1990] for the Dutch Wadden Sea.
Right: cross-sectional area of inlets verses mean spring tidal prism for different inlets around the world. The green points are inlets in the Wadden Sea. The red and blue points correspond to the updrift and downdrift case after 185 yr respectively. The line represents again the relationship according to Eysink [1990].

A sudden lowering of the bed level (both in the updrift sub-basin or at the geometrical centre of the basin) increases the tidal prism, especially in the updrift sub-basin. This is shown in table 4.2, which shows the tidal prism for the updrift and the downdrift sub-basin directly

after local lowering of the bed (so the inlet cross-sectional area is still unchanged). This larger tidal prism in the updrift sub-system causes increased erosion in the updrift inlet (cf. fig. 3.52), enlarging the cross-section area of this inlet. This larger erosion is also expected as a result of an increased tidal prism according to $P \sim UA/\omega$. For the downdrift inlet, this increase in erosion is not observed (but even a slight decrease in erosion), and the tidal prism in the downdrift sub-system is indeed unchanged after lowering.

run	reference	1 m updrift	1 m centre	2 m updrift
P_{down}	$3.2 \times 10^7\,\text{m}^3$	$3.3 \times 10^7\,\text{m}^3$	$3.2 \times 10^7\,\text{m}^3$	$3.2 \times 10^7\,\text{m}^3$
P_{up}	$4.3 \times 10^7\,\text{m}^3$	$4.7 \times 10^7\,\text{m}^3$	$4.8 \times 10^7\,\text{m}^3$	$4.9 \times 10^7\,\text{m}^3$

Table 4.2: Tidal prism for the downdrift (P_{down}) and the updrift (P_{up}) sub-basin directly after lowering ($t = 185\,\text{yr}$), for the three different cases in the numerical model study. Besides the tidal prism of the reference case is shown.

4.1.3 Analytical model

Using the analytical model of Ridderinkhof [1988] and Buijsman & Ridderinkhof [2007] (see appendix A), the amplitude of the flow in both inlets ($|Q|$), the residual flow (Q_{0t}) and the tidal prism (P) are calculated. The obtained values are shown in the left column of table 4.3. These values mach quite well with the values obtained for the reference case in the numerical model after 185 yr, that are shown in the right column of table 4.3.

	analytical model	Delft3D
$\lvert Q\rvert_{\text{down}}$	$1.7 \times 10^3\,\text{m}^3/\text{s}$	$2.6 \times 10^3\,\text{m}^3/\text{s}$
$\lvert Q\rvert_{\text{up}}$	$4.0 \times 10^3\,\text{m}^3/\text{s}$	$3.7 \times 10^3\,\text{m}^3/\text{s}$
Q_{0t}	$178\,\text{m}^3/\text{s}$	$160\,\text{m}^3/\text{s}$
P_{down}	$2.3 \times 10^7\,\text{m}^3$	$3.2 \times 10^7\,\text{m}^3$
P_{up}	$5.6 \times 10^7\,\text{m}^3$	$4.3 \times 10^7\,\text{m}^3$

Table 4.3: Comparison of amplitude of the water volume transport in the inlets ($|Q|$), residual discharge (Q_{0t}) and tidal prism (P) between the analytical model of Ridderinkhof [1988] and Buijsman & Ridderinkhof [2007], and the reference case after 185 yr of the complex numerical Delft3D model. The subscripts 'down' and 'up' indicate downdrift and updrift sub-system, respectively. Following model parameter values are used: $b' = h' = \ell' = Z' = 1$; $C_{\text{D}} = 0.0024$; $\alpha = 3/4$; $H_A = 2\,\text{m}$; $L_A = 4\,\text{km}$; $B_A = 4.5\,\text{km}$; $Z_A = 1.1\,\text{m}$

When the distance between the inlets is increased, as is done in § 3.2, the efficiency of the watershed in separating the two sub-systems turns out to decrease (cf. figs. 3.30 and 3.42), and the watershed shifts downdrift. To study these observations, the analytical model of Ridderinkhof [1988] is used. In this model, a larger inlet spacing means a larger length L_{A} of the updrift part of the channel (which automatically indicates a larger length of the downdrift part, because $\ell' = 1$) and a larger phase difference ϕ between the inlets. Both L_{A} and ϕ can be changed independently, unlike in the numerical model. Fig. 4.4 shows the amplitude of the water volume transport ($|Q|$) versus longshore coordinate for three cases in the analytical model: 1.) different phase difference and spatial distance (top panel), 2.) only different phase difference (middle panel), and 3.) only different spatial distance between the inlets (bottom panel). In all panels the red, blue and green curves correspond to the 'close', 'reference' and 'far' cases in the

numerical model, respectively.

The minima in the upper panel of fig. 4.4 show qualitatively the same differences between the three studied cases as observed in the numerical model (cf. fig. 3.24). The middle panel of fig. 4.4 (only phase difference is varied) shows a downdrift shift in the location of the minimum and an increase in the magnitude of the minimum in $|Q|$ with increasing inlet spacing. The lower panel (only spatial distance is varied) shows an updrift shift in the location of the minimum and a decrease in the magnitude of the minimum in $|Q|$ with increasing inlet spacing. From these results, it is concluded that the downdrift shift of the watershed with increasing inlet spacing is caused by the increased phase difference, whereas the more efficient separation of the sub-basins for small inlet spacing is merely a result of the small spatial distance between the inlets.

4.2 Additions to earlier studies

Although some numerical studies have been done on double-inlet tidal systems, e.g. by Salles et al. [2005], most studies on this subject are done using (semi-)analytical models [Van de Kreeke, 1990; De Swart & Volp, 2012]. This numerical study adds to previous studies on multiple inlets because it calculates the full depth-averaged equations of motion. In contrast to Salles et al. [2005], evolution of the bed is analysed starting with a flat bathymetry. From that, the characteristic branched channels start to form. Moreover, a watershed develops dynamically. This is of course also a numerical continuation of the work of Roos et al. [2013], whose results did not require tidal watersheds to preexist, but may be interpreted as resulting form the flow patterns. Moreover, most numerical models of the Wadden Sea use a grid resolution way smaller than the present $(1/50)\,\mathrm{m}^{-1}$, not resolving the small scale channels that can be resolved in this numerical study.

Most analytical studies thus far assume that waves are needed for a tidal inlet to reach a morphodynamic equilibrium. The sedimentation in the inlet due to wave-induced littoral drift should then balance the erosion due to the ebb currents [Escoffier, 1940]. This idea was extended to double inlets by e.g. Van de Kreeke [1990]. However, the present numerical model study showed that even in the absence of waves, the inlets in a double-inlet tidal system can stabilise, in the sense that they do not erode any further.

Finally, the study to the morphological impact of an instant lowering of the bed level is of vast interest today. Especially because of salt extraction and salt mining below the bed of the Dutch Wadden Sea. However, as far as known to the author, no physical studies and only some biological studies have been done on this particular subject, e.g. by Marquenie & De Vlas [2005].

4.3 Model aspects

4.3.1 Physical assumptions

In this numerical study, hydrodynamic calculations are carried out using the depth-averaged shallow water equations. Although a three-dimensional model would of course be interesting, it is especially useful when density difference, secondary flows or other complex flows need to be accounted for. Because of the relatively small scale (especially vertically) in this study,

stratification effects are neglected. Moreover, this study focusses on the long-term morphological effects, for which a depth-averaged simplification is generally considered to be sufficient [Coco et al., 2013].

To calculate the drag coefficient C_{D} in the depth-averaged shallow water equations, a spatially uniform Chézy coefficients is used. It is tested whether the choice for a Chézy coefficient or a Manning coefficient largely effects the hydrodynamical and morphological parameters in the initial evolution. This is done because when a Manning coefficient is used, the bed shear stress in eq. (2.2) becomes proportional to $H^{-1/3}$. The effect turned out to be minor during the initial evolution. Eventually, a Chézy value of $C_{\mathrm{D}} = 65\,\mathrm{m}^{1/2}/\mathrm{s}$ turns out to give physically reasonable results.

The sediment in this study consists of sand of only a single grain size, whereas in reality the bed consists of layers with different particle characteristics (both cohesive and non-cohesive). Although it is assumed that implementation of additional particle classes does not change the main mechanisms, taking particle classes of different particle size into account could introduce sorting mechanisms.

It is important to realise that atmospheric effects are completely absent in the experiments that were carried out. These effects include e.g., storm surges and wind-driven generation of waves. Implementation of these effects could considerably change the drying and flooding pattern of the tidal flats in the basin, which is now purely tide-determined. Moreover, the tidal forcing is very regular, being only one harmonic component (M2). Excluding the M4 component in the forcing of the model (which is, however, in the Wadden Sea non-negligible), has certainly an influence on e.g., the import of sediment in the system due to tidal asymmetry. A potential development towards an equilibrium state would constantly be disturbed by an irregular atmospheric influence and by a more complex tidal forcing including the spring-neap cycle.

Besides a lack of dynamically induced waves (by atmospherical effects), also no waves are included in the model in any other way. This has the drawbacks that no stirring of sediment by waves can occur, and that littoral drift is completely absent. According to Escoffier [1940] and Van de Kreeke et al. [2008], littoral drift due to waves provides an important mechanism for importing sediment, and thus for the stability of the inlets. To make sure that the inlets do not keep on expanding (making the barrier islands disappear), only a specified number of grid cells can be submerged on either side of the each inlet. However, this could also lead to a final bathymetry with an inlet that is surrounded by fixed non-erodible banks. Because no erosion takes place at the end of the simulation of the numerical model ($t = 185\,\mathrm{yr}$), but not all sediment of the erodible banks is eroded, this assumption seems to be reasonable. Yet, it is striking that no continuous export of sediment occurs, which would be expected according to the mechanism proposed by Escoffier [1940]. This import is here governed by tidal asymmetry, and in the updrift inlet also largely by the residual flow (which is mainly a through-flow from updrift to downdrift sub-basin).

4.3.2 Numerical assumptions

In this study, the model domain is chosen in such a way that the resolution in the back barrier basin and in the inlets is high ($1/50\,\mathrm{m}^{-1}$), but the computational cost is still acceptable. Therefore, the resolution decreases at sea both longshore and cross-shore away from the in-

lets. Additionally, the model grid is decomposed in three different parts, which run parallel and interact with each other. To ensure that these computational aspects do not influence the model outcome significantly, runs are done with a constant resolution of $1/50\,\mathrm{m}^{-1}$ and with a domain that was not decomposed. This showed that these choices do not affect the obtained morphological patterns significantly. To further reduce the computational cost, a morphological factor was introduced, which was in several steps increased to $f_\mathrm{M} = 50$. Test runs with smaller morphological factors were done, to ensure that the outcome does not depend on the chosen value of f_M.

Apart from these domain constraints, the cyclic method used for the spatial discretisation in the numerical calculations implies a maximum on the time step, defined by the Courant-Friedrichs-Lewy number, $C_t = 2\Delta t\sqrt{gH\,(1/\Delta x^2 + 1/\Delta y^2)}$, which should generally not exceed a value of ten [Deltares, 2013]. This is checked initially, but at the end of the model runs, the inlets have deepened extremely. It should be checked therefore if a smaller time step is needed in the course of the simulation.

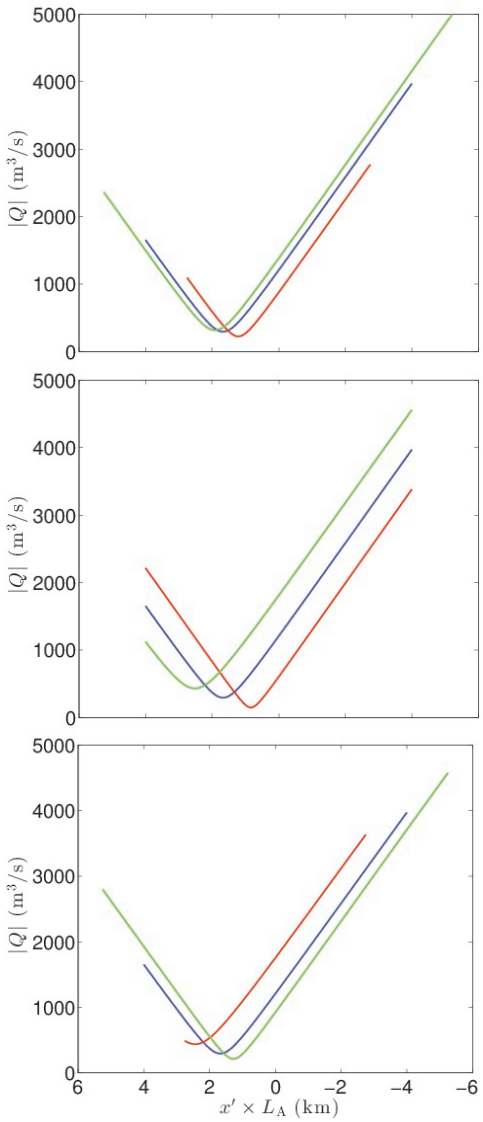

Figure 4.4: The amplitude of the water volume transport versus distance (both dimensionalised), making use of the conceptual model of Ridderinkhof [1988] (see appendix A). From top to bottom, results of three experiments are shown: 1.) varying phase difference and spatial distance, 2.) only varying phase distance and 3.) only varying spatial distance between the inlets. In all three panels, red indicates a close distance between the inlets, blue the reference case and green a large distance between the inlets. Following model parameter values are used: $b' = h' = \ell' = Z' = 1$; $C_{\mathrm{D}} = 0.0024$; $\alpha = 3/4$; $H_A = 2\,\mathrm{m}$; $B_A = 4.5\,\mathrm{km}$; $Z_A = 1.1\,\mathrm{m}$. The used values for spatial distance L_{A} are 2.75 km, 4.0 km and 5.25 km. The used values for phase difference ϕ are 1.5°, 3.0°and 4.5°.

5. Conclusions

In this thesis, a numerical model was used to simulate the morphological evolution of a double inlet tidal system. As it appears, these systems can be stable on a timescale of centuries, in the sense that both inlets stay open and even stabilise their cross-sectional area. Although stated otherwise in literature, it appears that for the existence of such morphodynamic equilibrium no waves have to be taken into account. During the morphological evolution, a tidal watershed develops dynamically. Despite the quasi-stable state of the system, a steady import of sediment is observed, infilling the basin with sand. This import is caused by tidal asymmetry, and in the updrift sub-system also by the residual flow (which is largely dominant). The import is however way lower than the current average global rate of sea level rise observed.

From sensitivity tests to the distance between the inlets, it appears that for increasing distance between the inlets, the watershed shifts downdrift. This is mainly caused by the increased phase difference between the inlets. The efficiency of the watershed (in separating the two sub-basins) decreases with increasing inlet spacing, which is (especially for small inlet spacing) mainly caused by the increasing spatial distance between the inlets. Furthermore, the two sub-systems behave more equal in terms of sediment import when the inlet spacing is increased, due to a decreased import of sediment into the updrift sub-basin with increasing inlet spacing.

To investigate the effect of an instant lowering of the bed, caused by e.g. salt extraction, the bed was lowered artificially in the updrift sub-basin and at the geometrical centre of the basin. Almost no morphological changes occur in the regions of peak lowering during 70 yr after the time of lowering. This is caused by continuity, decreasing the velocity and therefore causing a bed shear stress below the critical value for sediment erosion. Due to decreasing sediment import induced by tidal asymmetry, the lowering is not compensated by an additional import of sediment, and even a decreased import is observed compared to a situation without lowering of the bed.

6. Outlook

This thesis gives a first impression of the development of double-inlet tidal systems and shows that it is possible to get physically reasonable results when using a complex numerical model with a fine grid. However, some improvements should be made to the grid and the model parameters in future research. Furthermore, a lot of questions are still unanswered, and could be examined in future research.

6.1 Possible improvements

Although the domain is already divided into three separate sub-grids that interact, it could be a good idea to also split the sea in two parts. The sea is at the moment still the most computationally expensive part of the domain. Tests should be done on the possibilities of splitting the sea and therefore also one of the domain boundaries. It is especially unclear if splitting of a boundary condition will have unwanted effects. A different solution to this computationally expensive sub-grid, is decreasing the dimensions of the sea. In that case, it should be confirmed that the inlets are separated far enough from the domain boundaries to not experience unwanted boundary effects. Apart from these domain improvements, it may be possible to further (or in a shorter time interval) increase the morphological factor, which than considerably reduces the computational cost. Finally, as discussed in § 4.3.2, it should be checked whether a smaller time step is needed in the course of the simulation, in order to meet the restriction on the Courant-Friedrichs-Lewy number.

More extensive sensitivity experiments should be done on the sudden transition in the initial sea bed (from flat to sloping). Especially in long runs as done in this experiment, non-negligible erosion and sedimentation patterns take place here, which could possibly influence the seaward extension of the updrift ebb-tidal delta.

6.2 Ideas for future research

To compare the model results to measurements, first trials have already been started with a slightly increased tidal range and/or a downdrift extended back barrier basin. These adaptations make the system more comparable with the Baltrum site in the German Wadden Sea. Runs like this also gain information on the sensitivity of the obtained results to the imposed tidal range, which probably has quite a large effect (especially on the flooding/drying behaviour of the shoals in the basin). In addition to an increased tidal range, the effect of imposing an additional M4 tide could also gain more reliable results, because the Wadden Sea has quite an

important offshore generated M4 component.

As mentioned earlier, littoral drift is not included in the present model, whereas it is an important mechanism according to Escoffier [1940]. It is therefore interesting to include it parametrically by dumping sediment in the basin each time step. However, extensive sensitivity tests should be done here to make sure that the desired effect is reached and side effects are minimised. When this works, more reliable studies on the eventual stability of double-inlet tidal systems can be done, even without artificially making the barrier islands to a large extend non-erodible. A first test has already been done. The total amount of sediment entering the inlets due to littoral drift is in the Wadden Sea estimated to be $\sim 10^6\,\mathrm{m}^3/\mathrm{yr}$ (following e.g. Roos et al. [2013]). Because the numerical model domain is based on the island of Baltrum, which is small compared to other Wadden islands, 25% of this rate is dumped as sand in each inlet. The results are briefly discussed in appendix B, and reveal shallower channels and larger and higher shoals, as expected. Both inlets still stay open after 92 yr. To further investigate the effect of littoral drift, the temporal evolution of the cross-sectional areas A_{up} and A_{down} of updrift and downdrift inlet respectively, could be plotted in $(A_{\mathrm{up}}, A_{\mathrm{down}})$-space, as is done by Van de Kreeke [1990] to investigate whether there is a tendency to close one inlet.

As it turned out, the orientation of the main channels in the back barrier basin (in terms of net sediment transport) is largely determined by the dimensions of the basin. It would be nice to investigate whether the main conclusions of this thesis still hold when the dimensions of the basin are doubled or even more enlarged, but with the same inlet dimensions. It is for instance expected that the tidal prism increases, and as a result the inlets will experience increased erosion. Yet, such larger model grid should go at the cost of high resolution to avoid computationally too expensive model runs.

Finally, the Wadden Sea is nowadays also subject to sea level rise. As already mentioned in § 4.1.2, the sediment input in the numerical model results are not enough to keep up with sea level rise, so it would be interesting to investigate what effect a rising sea level would have on the sediment import. Not only will shoals be drowned, but also will the inlet cross-sectional areas increase. If however rising sea level leads to an increased import of sediment, the system may keep up with it and maintain its partly submerged shoals, which are so important for e.g. birds.

Appendices

A. Analytical model for water flow in double inlet tidal system

In this research, a comparison of the model results is made with the analytical model by Ridderinkhof [1988] and Buijsman & Ridderinkhof [2007]. This model is based on the basic shallow water equations, viz.

$$\begin{aligned} &\frac{\partial Q}{\partial t} + \frac{\partial}{\partial x}\left(\frac{Q^2}{B(H+\eta)}\right) + gB(H+\eta)\frac{\partial \eta}{\partial x} + \frac{C_\mathrm{D} Q|Q|}{B(H+\eta)^2} = 0\,, \\ &\frac{\partial Q}{\partial x} + B\frac{\partial \eta}{\partial t} = 0\,, \end{aligned} \tag{A.1}$$

with Q the volume transport, H the mean water depth, B the width of the basin, η the water elevation relative to the mean water depth, $C_\mathrm{D} = \frac{g}{C^2}$ the bottom-friction coefficient, C the Chezy coefficient, x the longitudinal coordinate and t the time. The model basically approaches the Marsdiep–Vlie system in the Dutch Wadden Sea by a channel, consisting of two connected parts. In this appendix, this model will be briefly discussed, but not in-depth. Furthermore, some corrections to the published equations will be made. Because the notation varies between references, it is chosen to follow Ridderinkhof [1988] with some minor changes to avoid confusion.

A.1 Water flow and tidal prism

The equations are rewritten making some assumptions not discussed here and are made dimensionless, making use of the following scaling parameters:

$$\begin{array}{ll} B = B_\mathrm{A} b' & B_\mathrm{A} \text{ is width of updrift basin,} \\ H = H_\mathrm{A} h' & H_\mathrm{A} \text{ is depth of updrift basin,} \\ x = L_\mathrm{A} x' & L_\mathrm{A} \text{ is length of updrift basin,} \\ \eta = Z_\mathrm{A} \eta' & Z_\mathrm{A} \text{ is tidal amplitude at the updrift inlet } (x' = -1), \\ t = t'/\sigma & \sigma \text{ is frequency of tidal wave,} \\ Q = \langle Q \rangle q' & \langle Q \rangle = B_\mathrm{A} L_\mathrm{A} Z_\mathrm{A} \sigma\,, \\ \lambda_1 = \sigma H_\mathrm{A} \lambda_1' & \lambda_1 = \frac{8C_\mathrm{D}}{3\pi}\frac{|u|}{H_\mathrm{A}\sigma} \text{ is linearised bottom friction coefficient,} \\ k = k'/L_\mathrm{A} & k = \frac{\sigma}{\sqrt{gH_\mathrm{A}}} \text{ is wavenumber,} \\ q_0 = \langle q \rangle q_0' & \langle q_0 \rangle = \langle Q \rangle Z_\mathrm{A} H_\mathrm{A}^{-1}\,, \\ \lambda_0 = \sigma H_\mathrm{A} \lambda_0' & \lambda_0' = 1.5\lambda_1'\,, \end{array} \tag{A.2}$$

in which the primed variables are dimensionless and $|u|$ is a typical velocity amplitude. Furthermore, included in the boundary conditions are a dimensionless water elevation amplitude

of 1 and Z' at updrift (called A) and downdrift (called B) inlet respectively, and continuous η and q at the separation of the two channels.

In the following, primes will be omitted, but all equations will be dimensionless. Following Ridderinkhof [1988], the system can be solved for $-1 < x < 0$ by

$$\begin{aligned} \eta_{\mathrm{A}}(x,t) &= \frac{1}{2}\left[\eta_{\mathrm{A}}(x)\mathrm{e}^{\mathrm{i}t} + \text{c.c.}\right] , \\ \eta_{\mathrm{A}}(x) &= A\mathrm{e}^{\mathrm{i}\tau x} + B\mathrm{e}^{-\mathrm{i}\tau x} , \\ q_{\mathrm{A}}(x,t) &= q_{\mathrm{A}}(x)\mathrm{e}^{\mathrm{i}t} + \text{c.c.} , \end{aligned} \tag{A.3}$$

and for $0 < x < \ell$ by

$$\begin{aligned} \eta_{\mathrm{B}}(x,t) &= \frac{1}{2}\left[\eta_{\mathrm{B}}(x)\mathrm{e}^{\mathrm{i}t} + \text{c.c.}\right] , \\ \eta_{\mathrm{B}}(x) &= C\mathrm{e}^{\mathrm{i}\tau x} + D\mathrm{e}^{-\mathrm{i}\tau x} , \\ q_{\mathrm{A}}(x,t) &= q_{\mathrm{B}}(x)\mathrm{e}^{\mathrm{i}t} + \text{c.c.} , \end{aligned} \tag{A.4}$$

with c.c. indicating the complex conjugate and

$$\begin{aligned} q_{\mathrm{A}}(x) &= \frac{\mathrm{i}}{\tau_{\mathrm{A}}^2}\frac{\partial \eta_{\mathrm{A}}}{\partial x} , \\ q_{\mathrm{B}}(x) &= \frac{b\mathrm{i}}{\tau_{\mathrm{B}}^2}\frac{\partial \eta_{\mathrm{B}}}{\partial x} . \end{aligned} \tag{A.5}$$

With appropriate boundary conditions, this results in following values for coefficients A, B, C and D:

$$\begin{aligned} C &= \frac{(\cos\tau_{\mathrm{A}} + \mathrm{i}\gamma\sin\tau_{\mathrm{A}})Z\mathrm{e}^{\mathrm{i}\phi} - \mathrm{e}^{-\mathrm{i}\tau_{\mathrm{B}}\ell}}{2\mathrm{i}[\cos\tau_{\mathrm{A}}\sin(\tau_{\mathrm{B}}\ell) + \gamma\sin\tau_{\mathrm{A}}\cos(\tau_{\mathrm{B}}\ell)]} \\ D &= \frac{(-\cos\tau_{\mathrm{A}} + \mathrm{i}\gamma\sin\tau_{\mathrm{A}})Z\mathrm{e}^{\mathrm{i}\phi} + \mathrm{e}^{\mathrm{i}\tau_{\mathrm{B}}\ell}}{2\mathrm{i}[\cos\tau_{\mathrm{A}}\sin(\tau_{\mathrm{B}}\ell) + \gamma\sin\tau_{\mathrm{A}}\cos(\tau_{\mathrm{B}}\ell)]} \\ A &= \frac{1}{2}\left[(C+D) + \gamma(C-D)\right] \\ B &= \frac{1}{2}\left[(C+D) - \gamma(C-D)\right] \\ \gamma &= b\tau_{\mathrm{A}}/\tau_{\mathrm{B}} = 1 . \end{aligned} \tag{A.6}$$

With these coefficient values the water elevation η and the water flow q are fully determined, both in the updrift (A) and downdrift (B) sub-system. The water flow q is also used to calculate the tidal prism by averaging over the ebb-duration of one tidal period.

To make things somewhat simpeler, it can for this research be assumed that the complex wavenumber τ is the same in both parts of the model (because h is kept the same in both parts), and therefore $\tau_{\mathrm{A}} = \tau_{\mathrm{B}} = \tau = \sqrt{k^2\left(1 - \lambda_1\mathrm{i}\right)}$ and $\gamma = 1$. From this, it also results that $A = C$ and $B = D$.

Two corrections have been made to the original equations of Ridderinkhof [1988]. Firstly, a factor 1/2 is added in eqs. (A.3) and (A.4). Secondly, the first minus in the expression for B in eq. (A.6) was wrongly stated in Ridderinkhof [1988] to be a plus.

A.2 Residual flow

Following Ridderinkhof [1988] and Buijsman & Ridderinkhof [2007], which is based hereon, the dimensionless model can be used to calculate the residual water flow, with a component due to an amplitude difference between the inlets and a component due to a phase difference. To make life easier, following parameters are defined, in which it is assumed that $b = 1$ (both channel-parts have same width) and:

$$\begin{aligned}
\hat{P} &= \frac{2}{\tau\left(-\mathrm{e}^{\mathrm{i}\tau(1+\ell)} - \mathrm{e}^{\mathrm{i}\tau(1+\ell)}\right)} \\
\hat{Q} &= \frac{\left(\mathrm{e}^{\mathrm{i}\tau(1+\ell)} + \mathrm{e}^{-\mathrm{i}\tau(1+\ell)}\right)}{\tau\left(\mathrm{e}^{-\mathrm{i}\tau(1+\ell)} - \mathrm{e}^{\mathrm{i}\tau(1+\ell)}\right)} \\
F &= \hat{P}\hat{P}^* - \hat{Q}\hat{Q}^* \\
G &= \frac{2}{\mathrm{i}}(\hat{P}\hat{Q}^* - \hat{Q}\hat{P}^*)\,,
\end{aligned} \tag{A.7}$$

where the star (*) denotes the complex conjugate. Note the factor $\frac{2}{\mathrm{i}}$ in the expression for G, which was wrongly stated in Ridderinkhof [1988] to be 2i.

Using these new parameters, the residual flow q_0 from the updrift (A) to the downdrift (B) side can be calculated by

$$q_0 = \frac{1}{\lambda_0(1+\ell)}\left[(\alpha F - \frac{2}{k^2})(Z^2 - 1) + \alpha G Z \sin\phi\right]\,, \tag{A.8}$$

with α a parameter introduced by Buijsman & Ridderinkhof [2007] that indicates whether or not the Bernoulli effect is accounted for. However, unlike te values mentioned by Buijsman & Ridderinkhof [2007], $\alpha = \frac{3}{4}$ when the Bernoulli effect is account for and $\alpha = 1$ when not. The first term on the RHS of eq. (A.8) contributes to the residual flow by a water elevation amplitude difference between the inlets, and the second term contributes to the residual flow by both a phase difference and a water elevation amplitude difference.

In Buijsman & Ridderinkhof [2007] eq. (A.8) is rewritten in dimensional form as

$$Q_{0t} = -\frac{BH}{F_l L}\left[\frac{\alpha}{HB^2}\left(|Q_\mathrm{B}|^2 - |Q_\mathrm{A}|^2\right) + 2g\left(|\eta_\mathrm{B}|^2 - |\eta_\mathrm{A}|^2\right)\right]\,, \tag{A.9}$$

where Q_{0t} is the dimensional residual flow from downdrift to updrift side, $|Q_\mathrm{A}|$ and $|Q_\mathrm{B}|$ are the amplitudes of the water volume transport in the inlets in updrift and downdrift inlet, respectively, $|\eta_\mathrm{A}|$ and $|\eta_\mathrm{B}|$ are the amplitudes of the dimensional water elevation in updrift and downdrift inlet, respectively, and F_l is a dimensional linearised bottom friction coefficient. The first term on the RHS of eq. (A.9) contributes to the residual flow by a water transport amplitude difference between the inlets, and the second term contributes to the residual flow by a water elevation amplitude difference between the inlets. Note that the factor $2g$ in eq. (A.9) (corresponding to the factor $\frac{2}{k^2}$ in eq. (A.8)) is wrongly stated in Buijsman & Ridderinkhof [2007] to be $\frac{2}{g}$.

A.3 Parameter setting

The parameter values of the analytical model are chose such, that the channel area is the same as the total basin area in the numerical model. This should make the tidal prisms in both models to be of approximately the same magnitude, which enables direct comparison between the models. Furthermore, the length of the channel is determined by fitting a circular curve through the landward centre of both inlets (coordinates $(10.5, 12.5)$ and $(16.5, 12.5)$ in km) in the numerical model, and through the geometrical centre at 1 km from the coast (coordinate $(13.5, 14.5)$ in km). This results in a arc length of approximately 8 km, which is taken to be the combined length of downdrift and updrift channel in the analytical model. The sea level amplitude Z_{A} with which the system is forced is set to 1.1 m, as is observed in the basin in the numerical model. The phase difference ϕ between the inlets is the same as in the numerical model for all three studied distances between the inlets, viz. $\phi = 1.5°$, $\phi = 3.0°$ and $\phi = 4.5°$. All parameter values are shown in table A.1.

	dimensional	dimensionless	
B_{A}	4.5×10^3 m	b'	1
H_{A}	2×10^3 m	h'	1
L_{A}	4×10^3 m	ℓ'	1
Z_{A}	1.1 m	Z'	1
σ	$1.405 \times 10^{-4}\,\mathrm{s}^{-1}$		
C	$65\,\mathrm{m}^{1/2}\mathrm{s}^{-1}$		
g	$9.81\,\mathrm{m\ s}^{-2}$		
ϕ	1.5°	3.0°(ref.)	4.5°

Table A.1: Dimensions and parameter setting of the analytical model. The bottom row gives the values of the phase difference between the inlets, corresponding to an inlet spacing of 3 km, 6 km and 9 km in the numerical model, respectively.

In order to get a feeling of the sensitivities of tidal prism and residual discharge in the analytical model, fig. A.1 shows the tidal prism (left) and the residual flow (right) as function of (from top to bottom) B_{A}, H_{A}, L_{A} and C_{D}. For the tidal prism, the blue (red) curve denotes the downdrift (updrift) sub-system. In all panels, solid curves denote $\ell = 1$ and dashed curves $\ell = 0.78$ (based on the devision of the sub-basins in the numerical model after 185 yr). For the tidal prism, these two curves overlap. The black vertical dashed lines denote the used parameter values for e.g. table. 4.3, whereas the horizontal red, blue and black dash-dotted lines denote the values of updrift tidal prism, downdrift tidal prism and residual flow after 185 yr in the numerical model, respectively.

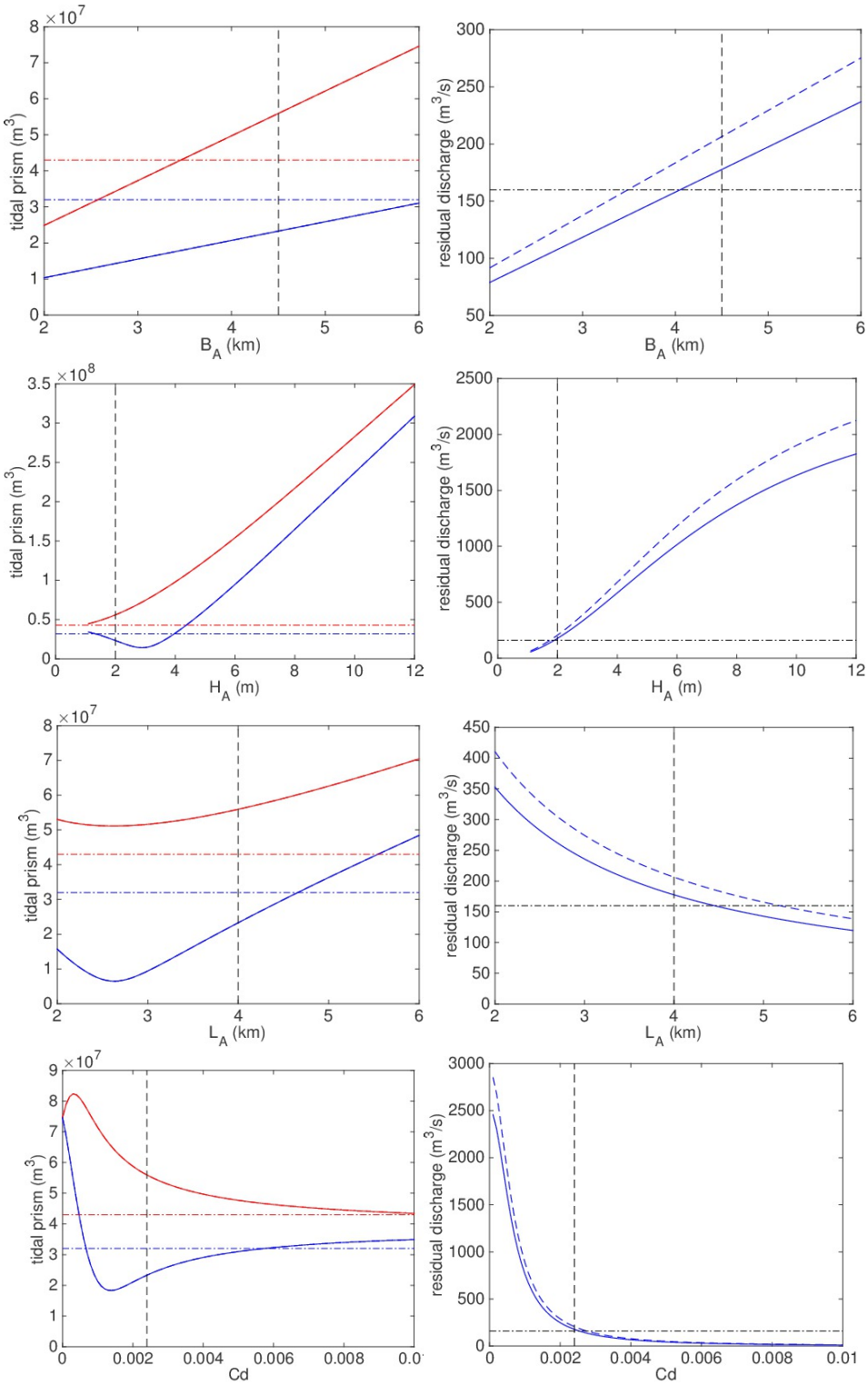

Figure A.1: Sensitivity of tidal prism (in m^3, left column) and residual discharge (in m^3/s, right column) of the analytical model of Ridderinkhof [1988] and Buijsman & Ridderinkhof [2007] to parameters B_A, H_A, L_A and C_D. Blue (red) indicates the downdrift (updrift) inlet and dotted curves indicate the use of $\ell' = 0.78$ (based on actual separation between the sub-basins) rather than $\ell' = 1$ (based on the geometrical centre of the basin). The dashed black lines indicates the used parameter values in table 4.3, that correspond to the reference case in the present research. The horizontal dash-dotted lines indicate the values of tidal prism and residual discharge after 185 yr in the numerical model.

B. Parametrical implementation of littoral drift

This appendix briefly discusses the test run that has already been done on the parameterisation of littoral drift in the inlets, as mentioned in § 6.2.

Sediment import in inlets due to littoral drift along the coast in the Wadden Sea is estimated to be $\sim 10^6\,\mathrm{m}^3/\mathrm{yr}$ (following Roos et al. [2013]). To parameterise littoral drift, in each of the two inlets sediment can be dumped at each time step ('nourishment'), with a rate that is a fraction of the estimated littoral drift, e.g., 25%. This is done, because the Baltrum system (on which the numerical model grid is based) is small compared to most Wadden islands. Most probably, part of this sediment will be imported into the basin, because of the tendency of the modelled system to import sediment. However, part of this dumped sediment may stay in the inlet and provide a counteracting force to the erosion of the inlet. Fig. B.1 shows bed level (left panels) and bed level change (right panels) after 92 yr for the reference case (upper panels) and for a test run (bottom panels) in which $2.5 \times 10^5\,\mathrm{m}^3$ sediment is dumped in the inlet per year to parameterise the effect of littoral drift. Comparing the case with parameterised littoral drift with the reference case, reveals that a lot more sediment is transported into the basin when littoral drift is implemented, leading to larger and higher shoals, and to smaller and less deep channels. The shoals and channels are also already more evolved towards the boundaries of the basin, suggesting a faster evolution of the channel-shoal system of the nourished system compared to the reference system. As expected, the inlets are shallower due to the deposition of sediment. Remarkably, the downdrift ebb-tidal delta has shifted more downdrift as a result of the sediment dump in the inlets.

Fig. B.2 shows the total deposited sediment volume versus time for both inlets and sub-basins. After 30 yr the amount of eroded sediment stays constant in both inlets (dashed lines), but the net effect in the inlets is less erosion than in the reference case (cf. 3.20), as is expected due to the nourishment. In both sub-basins a linearly increasing amount of deposited sediment is observed, with a net sediment transport of $1.7 \times 10^5\,\mathrm{m}^3/\mathrm{yr}$ into the basin (taking into account the total of the two inlets). This corresponds to a mean increase of the bed level of 0.47 mm/yr, which is larger than the 0.35 mm/yr observed in the reference case, but still way below global mean sea level rise. From fig. B.2 it is thus suggested that the system keeps importing sediment, as was also observed in the main part of this research, and will probably eventually silt up totally, if enough sediment is supplied in the inlet or the nearshore sea. However, it is still unclear whether the system would evolve towards a single-inlet system by closing one inlet. The import of sediment in the updrift basin is namely mainly caused by the residual flow, which would disappear after closure of the other inlet.

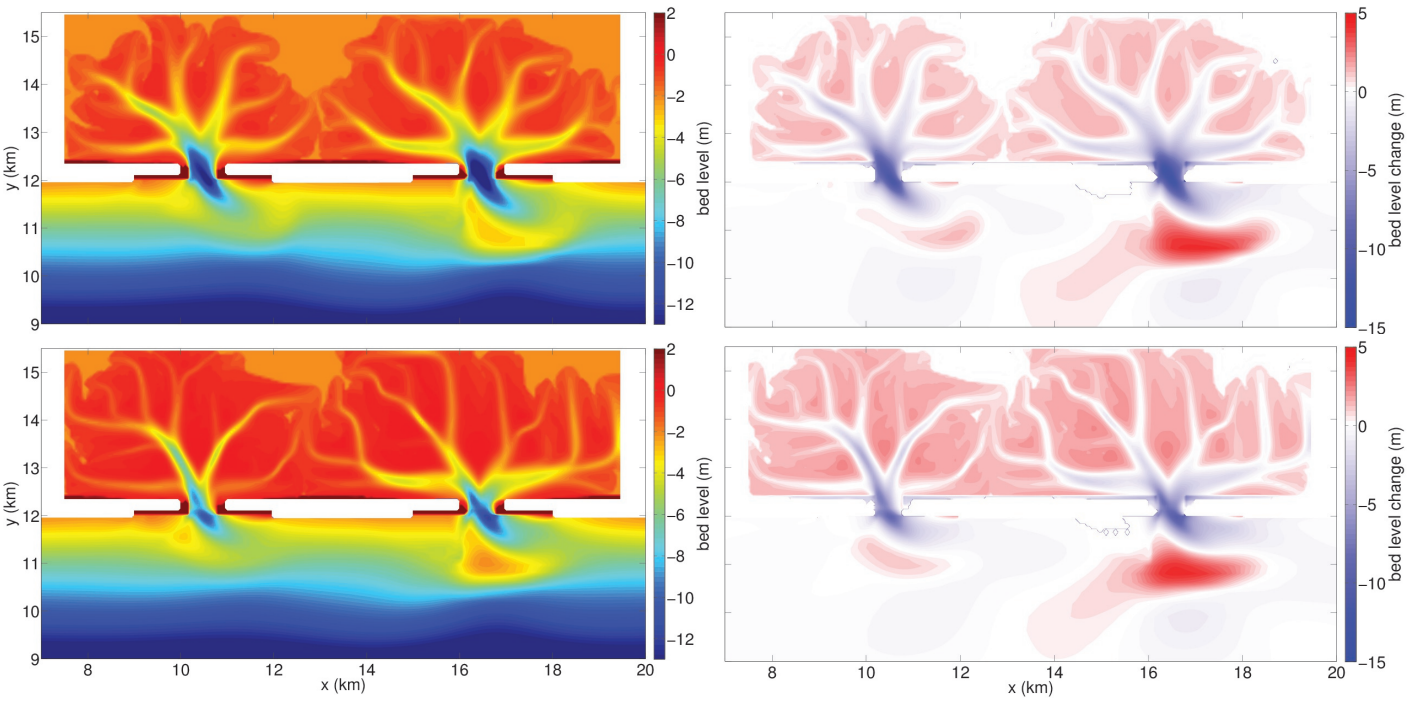

Figure B.1: Colour plots of the bed level (in meters, left column) and the change in bed level (in meters, right column) in the domain after 92 yr. The upper panels show the reference case, whereas the lower panels show the parameterised implementation of littoral drift by a sediment dump in both inlets at a rate of $25 \times 10^5\,\mathrm{m}^3/\mathrm{yr}$.

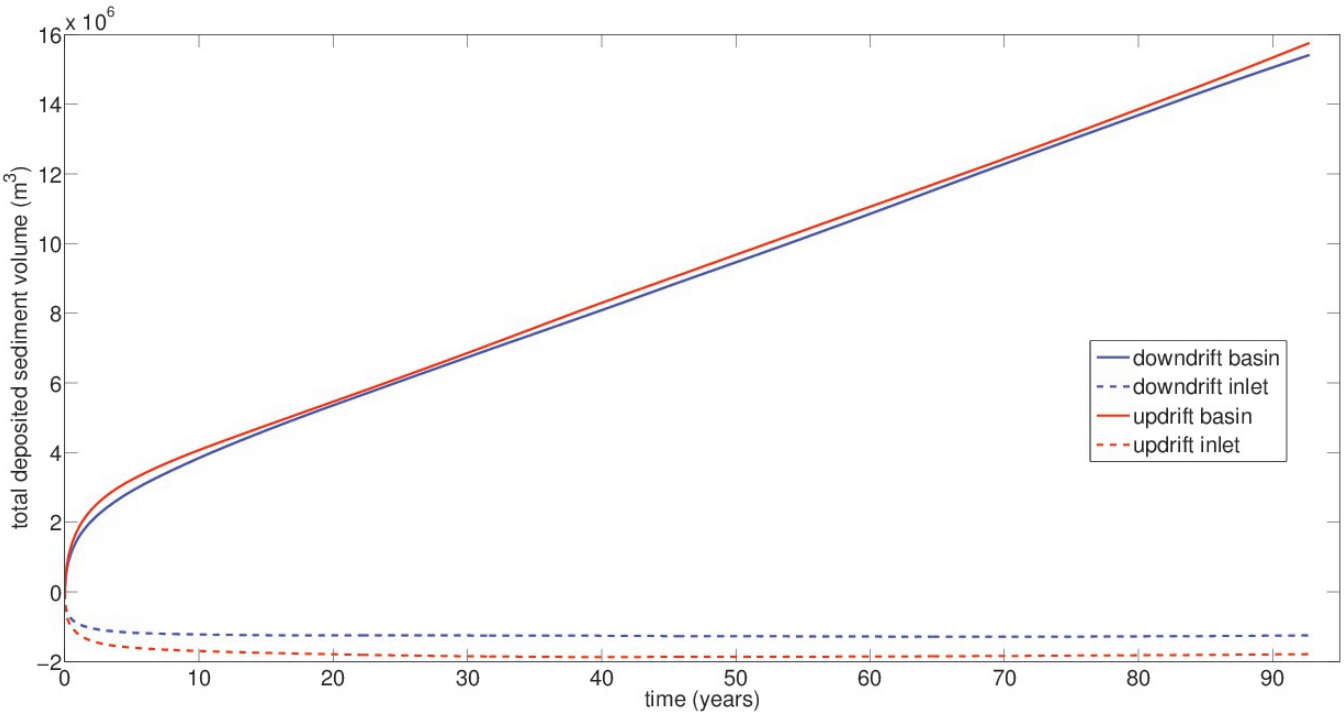

Figure B.2: Total deposited sediment volume versus time in both inlets, sub-basins and the total system of basin and inlets (excluding the sea) for a sediment dump of $2.5 \times 10^5\,\mathrm{m}^3/\mathrm{yr}$ in both inlets.

Bibliography

Amos, C.L., Bergamasco, A., Umgiesser, G., Cappucci, S., Cloutier, D., DeNat, L., Flindt, M., Bonardi, M., & Cristante, S. The stability of tidal flats in Venice Lagoon — the results of in-situ measurements using two benthic, annular flumes. *Journal of Marine Systems*, 51(1): 211–241, 2004.

Beerlage, B. & Ten Holder, V. Natural gas production in the Wadden area: evaluation an essential component of environmental assessment. Netherlands Commission for Environmental Assessment, 2009.

Beets, D.J. & Van der Spek, A.J.F. The Holocene evolution of the barrier and back-barrier basins of Belgium and the Netherlands as a function of late Weichelian morphology, relative sea-level rise and sediment supply. *Geologie en Mijnbouw*, 79(1):3 – 16, 2000.

Brouwer, R.L., Van de Kreeke, J., & Schuttelaars, H.M. Entrance/exit losses and cross-sectional stability of double inlet systems. *Estuarine, Coastal and Shelf Science*, 107:69–80, 2012.

Brown, E.I. Inlets on sandy coasts. American Society of Civil Engineers, 1928.

Buijsman, M.C. The impact of gas extraction and sea level rise on the morphology of the Wadden Sea. *Delft Hydraulics, Report H*, 3099:30, 1997.

Buijsman, M.C. & Ridderinkhof, H. Water transport at subtidal frequencies in the Marsdiep inlet. *Journal of Sea Research*, 58(4):255 – 268, 2007.

CERC. *Shore Protection Manual*. US Army Corps of Engineers, Vicksburg, Missisipi, fourth edition, 1984.

Cleveringa, J. & Oost, A.P. The fractal geometry of tidal-channel systems in the Dutch Wadden Sea. *Geologie en Mijnbouw*, 78(1):21–30, 1999.

Coco, G., Zhou, Z., Van Maanen, B., Olabarrieta, M., Tinoco, R., & Townend, I. Morphodynamics of tidal networks: Advances and challenges. *Marine Geology*, 346:1–16, 2013.

Davis, R.A. & Fitzgerald, D.M. *Beaches and Coasts*. Blackwell Science Ltd., 2004.

Deltares. *Delft3D-FLOW User Manual*, 2013.

Dissanayake, D.M.P.K., Roelvink, J.A., & Van der Wegen, M. Modelled channel patterns in a schematized tidal inlet. *Coastal Engineering*, 56(11–12):1069 – 1083, 2009.

Dissanayake, D.M.P.K., Ranasinghe, R., & Roelvink, J.A. The morphological response of large tidal inlet/basin systems to relative sea level rise. *Climatic Change*, 113:253–276, 2012.

Elias, E.P.L., Van der Spek, A.J.F., Wang, Z.B., & De Ronde, J. Morphodynamic development and sediment budget of the Dutch Wadden Sea over the last century. *Netherlands Journal of Geosciences - Geologie en Mijnbouw*, 91(3):293 – 310, 2012.

Escoffier, F. The stability of tidal inlets. *Shore and Beach*, pages 114 – 115, October 1940.

Eysink, W.D. Morphologic response of tidal basins to changes. *Coastal Engineering Proceedings*, 1(22), 1990.

Flöser, G., Burchard, H., & Riethmüller, R. Observational evidence for estuarine circulation in the German Wadden Sea. *Continental Shelf Research*, 31(16):1633–1639, 2011.

Foreman, M.G.G. Manual for tidal currents analysis and prediction. Unpublished manuscript; online revised in 2004, 1978.

Fortunato, A.B. & Oliveira, A. A modeling system for tidally driven long-term morphodynamics. *Journal of hydraulic Research*, 42(4):426–434, 2004.

Friedrichs, C. T. & Aubrey, D. G. Non-linear tidal distortion in shallow well-mixed estuaries: a synthesis. *Eastuarin, Coastal and Shelf Science*, 27:521–545, 1988.

Fry, V.A. & Aubrey, D.G. Tidal velocity asymmetries and bedload transport in shallow embayments. *Estuarine, Coastal and Shelf Science*, 30(5):453–473, 1990.

Van de Kreeke, J. Can multiple tidal inlets be stable? *Estuarine, Coastal and Shelf Science*, 30(3):261–273, 1990.

Van de Kreeke, J. & Robaczewska, K. Tide-induced residual transport of coarse sediment; application to the Ems estuary. *Netherlands Journal of Sea Research*, 31(3):209 – 220, 1993.

Van de Kreeke, J., Brouwer, R.L., Zitman, T.J., & Schuttelaars, H.M. The effect of a topographic high on the morphological stability of a two-inlet bay system. *Coastal Engineering*, 55(4):319–332, 2008.

Van Leeuwen, S.M., Van der Vegt, M., & De Swart, H.E. Morphodynamics of ebb-tidal deltas: a model approach. *Estuarine, Coastal and Shelf Science*, 57(5–6):899 – 907, 2003.

Lesser, G.R., Roelvink, J.A., Van Kester, J.A.T.M., & Stelling, G.S. Development and validation of a three-dimensional morphological model. *Coastal Engineering*, 51(8–9):883 – 915, 2004.

Lincoln, J.M. & Fitzgerald, D.M. Tidal distortions and flood dominance at five small tidal inlets in southern Maine. *Marine geology*, 82(3):133–148, 1988.

Marciano, R., Wang, Z.B., Hibma, A., De Vriend, H.J., & Defina, A. Modeling of channel patterns in short tidal basins. *Journal of Geophysical Research*, 110(F01001), 2005.

Marquenie, J.M. & De Vlas, J. The impact of subsidence and sea level rise in the Wadden Sea: prediction and field verification. In *Managing European Coasts*, pages 355–363. Springer, 2005.

MER. Opzet monitoring zoutwinning Frisia, havenmond Harlingen. Netherlands Commission for Environmental Assessment, 2014.

Niemeyer, H.D. Long-term morphodynamical development of the East Frisian islands and coast. *Coastal Engineering Proceedings*, 1(24), 1994.

O'Brien, M.P. Equilibrium flow areas of tidal inlets on sandy coasts. *Coastal Engineering Proceedings*, 1(10), 1966.

Oost, A.P. & De Boer, P.L. Sedimentology and development of barrier islands, ebb-tidal deltas, inlets and backbarrier areas of the Dutch Waddensea. *Senckenbergiana maritima*, 24:65 – 115, 1994.

Prandle, D. The vertical structure of tidal currents. *Geophysical & Astrophysical Fluid Dynamics*, 22(1-2):29–49, 1982.

Rhein, M., Rintoul, S.R., Aoki, S., Campos, E., Chambers, D., Feely, R.A., Gulev, S., Johnson, G.C., Josey, S.A., Kostianoy, A., Mauritzen, C., Roemmich, D., Talley, L.D., & Wang, F. Observations: Ocean. In Stocker, T.F., Qin, D., Plattner, G.-K., Tignor, M., Allen, S.K., Boschung, J., Nauels, A., Xia, Y., Bex, V., & Midgley, P.M., editors, *Climate change 2013: The physical science basis. Contribution of Working Group I of the Fifth Assessment Report of the Intergovernmental Panel on Climate Cchange*. Cambridge University Press, 2013.

Ridderinkhof, H. Tidal and residual flows in the western Dutch Wadden Sea II: An analytical model to study the constant flow between connected tidal basins. *Netherlands Journal of Sea Research*, 22(3):185–198, 1988.

Ridderinkhof, W., de Swart, H.E., van der Vegt, M., & Hoekstra, P. Influence of the back-barrier basin length on the geometry of ebb-tidal deltas. *Ocean Dynamics*, 64:1333 – 1348, 2014a.

Ridderinkhof, W., De Swart, H.E., Van der Vegt, M., Alebregtse, N.C., & Hoekstra, P. Geometry of tidal inlet systems: A key factor for the net sediment transport in tidal inlets. *Journal of Geophysical Research: Oceans*, 119(10):6988–7006, 2014b.

Van Rijn, L.C., Roelvink, J.A., & Ter Horst, W. Approximation formulae for sand transport by currents and waves and implementation in DELFT-MOR. *WL— Delft Hydraulics Report*, Z3054, 2001.

Roelvink, J.A. Coastal morphodynamic evolution techniques. *Coastal Engineering*, 53(2–3):277 – 287, 2006.

Roelvink, J.A. & Walstra, D.J. Keeping it simple by using complex models. *Advances in Hydro-Science and -Engineering*, 6, 2004.

Roos, P.C., Schuttelaars, H.M., & Brouwer, R.L. Observations of barrier island length explained using an exploratory morphodynamic model. *Geophysical research letters*, 40(16):4338–4343, 2013.

Salles, P. Hydrodynamic controls on multiple tidal inlet persistence. Technical report, DTIC Document, 2001.

Salles, P., Voulgaris, G., & Aubrey, D.G. Contribution of nonlinear mechanisms in the persistence of multiple tidal inlet systems. *Estuarine, Coastal and Shelf Science*, 65(3):475–491, 2005.

Sha, L.P. Sand transport patterns in the ebb-tidal delta off Texel Inlet, Wadden Sea, the Netherlands. *Marine Geology*, 86:137 – 154, 1989a.

Sha, L.P. Variation in ebb-tidal delta morphologies along the west and east frisian islands, the netherlands and germany. *Marine Geology*, 89:11 – 28, 1989b.

Sha, L.P. & Van den Berg, J.H. Variation in ebb-tidal delta geometry along the coast of the netherlands and the german bight. *Journal of Coastal Research*, 9(3):730 – 746, 1993.

Soulsby, R. *Dynamics of marine sands: a manual for practical applications*. Thomas Telford, 1997.

Stanev, E.V., Wolff, J.-O., Burchard, H., Bolding, K., & Flöser, G. On the circulation in the East Frisian Wadden Sea: numerical modeling and data analysis. *Ocean Dynamics*, 53(1): 27–51, 2003.

Stanev, E.V., Brink-Spalink, G., & Wolff, J.-O. Sediment dynamics in tidally dominated environments controlled by transport and turbulence: a case study for the East Frisian Wadden Sea. *Journal of Geophysical Research: Oceans (1978–2012)*, 112(C4), 2007.

Stive, M.J.F. & Rakhorst, R.D. Review of empirical relationships between inlet cross-section and tidal prism. *Journal of Water Resources and Environmental Engineering*, 23:89–95, 2008.

De Swart, H.E. & Volp, N.D. Effects of hypsometry on the morphodynamic stability of single and multiple tidal inlet systems. *Journal of Sea Research*, 74(0):35 – 44, 2012.

De Swart, H.E. & Zimmerman, J.T.F. Morphodynamics of tidal inlet systems. *Annual Review of Fluid Mechanics*, 41(1):203–229, 2009.

Van der Vegt, M., Schuttelaars, H. M., & De Swart, H. E. Modeling the equilibrium of tide-dominated ebb-tidal deltas. *Journal of Geophysical Research-Earth Surface*, 111:F02013/1–F02013/15, 2006. doi: 10.1029/2005JF000312.

Van Rijn, L.C. *Principles of Sediment Transport in Rivers, Estuaries and Coastal seas*. Aqua Publications, 1993.

Van Veen, J. Eb-en vloedschaarsystemen in de Nederlandse getijwateren. *Journal of the Royal Dutch Geographical Society*, 67(303-3), 1950. republished in English as *Ebb and flood channel systems in the Netherlands tidal waters* in 2005.

Van Goor, M.A., Zitman, T.J., Wang, Z.B., & Stive, M.J.F. Impact of sea-level rise on the morphological equilibrium state of tidal inlets. *Marine Geology*, 202(3):211–227, 2003.

Van Maanen, B., Coco, G., & Bryan, K.R. A numerical model to simulate the formation and subsequent evolution of tidal channel networks. *Australian Journal of Civil Engineering*, 9 (1):61, 2011.

Vitousek, P.M., Mooney, H.A., Lubchenco, J., & Melillo, J.M. Human domination of Earth's ecosystems. *Science*, 277(5325):494–499, 1997.

Wang, Z.B., Louters, T., & De Vriend, H.J. Morphodynamic modelling for a tidal inlet in the Wadden Sea. *Marine Geology*, 126(1):289–300, 1995.

Van der Wegen, M. & Roelvink, J.A. Long-term morphodynamic evolution of a tidal embayment using a two-dimensional, process-based model. *Journal of Geophysical Research*, 113(C3): C03016, 2008.

Williams, J.J., O'Connor, B.A., Arens, S.M., Abadie, S., Bell, P., Balouin, Y., Van Boxel, J.H., Do Carmo, A.J., Davidson, M., Ferreira, O., Heron, M., Howa, H., Hughes, Z., Kaczmarek, L.M., Kim, H., Morris, B., Nicholson, J., Pan, S., Salles, P., Silva, A., Smith, J., Soares, C., & Vila-Concejo, A. Tidal inlet function: field evidence and numerical simulation in the INDIA project. *Journal of Coastal Research*, pages 189–211, 2003.

Xu, Z. Ellipse parameters conversion and velocity profiles for tidal currents in Matlab. 2002. URL `http://www.mathworks.com/matlabcentral/fileexchange/347-tidal-ellipse`.